
Investigations of Coherent Structures in Magnetically Confined Plasmas

Master Thesis

Supervisors:
Anders H. Nielsen
Jens J. Rasmussen
Jens Madsen

February 1, 2015

by

Jeppe Olsen, s092967

Preface

This master thesis is written as a part of the M.Sc. Eng. education in Physics and Nanotechnology at the Technical University of Denmark. The thesis corresponds to 30 ECTS points and was prepared at the Department of Physics using the Risø super computer for simulations.

I would like to thank my supervisors Anders Henry Nielsen, Jens Juul Rasmussen and Jens Madsen for guidance throughout the project and for always being helpful when issues arose.

Jeppe Olsen
Department of Physics
Technical University of Denmark
February 1, 2015

Abstract

Magnetically confined fusion has been proposed as an alternative to fossil fuels in order to stop the expulsion of greenhouse gases. However several technical difficulties need to be overcome in order to realise such a fusion reactor. Small fluctuations in plasma potential and density give rise to instabilities driving radial transport of extremely warm plasma in a fusion reactor, causing the fusion reaction to stop and destroying the chamber walls. The main cause of this radial transport is by the propagation of coherent plasma filaments also known as blobs.

This study investigates the dynamics of such blobs using an existing code, HESEL. The code was used to first examine the dynamics in weakly ionized plasmas and compared with experimental results and other simulations. Large discrepancies were found between HESEL, the experimental results and the other codes, likely due to lack of parallel dynamics in HESEL. However this will need to be investigated further in future works.

The code was also used to examine the behaviour of blobs for fully ionized plasmas, where previous results have shown good agreement with experiments. It was found that finite ion temperatures have a significant impact on the dynamics of the blobs, causing both faster radial propagation, but also causing poloidal movement not seen for low ion temperatures. Finally the maximum radial velocities of the blobs found with HESEL were compared with different scaling laws for varying initial blob parameters, and it was found that none of the theoretically derived models fit with the observed behaviour in the simulations. Especially the behaviour with increasing blob density was very different, seemingly scaling linearly in the simulations, where the theoretical estimates describe the scaling as a square root. This behaviour is also left to be explained in future works.

Resumé

Magnetisk indsluttet fusion er blevet foreslået som et alternativ til fossile brændstoffer for at stoppe udledningen af drivhusgasser. Der er dog flere tekniske problemer, der skal overvinDES for at virkeliggøre en sådan fusionsreaktor. Små fluktuationer i plasmapotentiale og tæthed leder til ustabiliteter, som driver en transport af ultra varmt plasma i en fusionsreaktor, hvilket fører til at fusionsreaktionen stopper og reaktorvæggene øDELÆGGES. Hovedårsagen til denne radielle transport er udbredelse af koherente plasmastrukturer, også kendt som blobs.

Denne opgave undersøger dynamikken af sådanne blobs ved at bruge en eksisterende kode, HESEL. Koden blev først brugt til at undersøge dynamikken i svagt ioniserede plasmaer og blev her sammenlignet med eksperimentelle resultater og andre simuleringer. Der blev fundet store forskelle mellem HESEL, de eksperimentelle resultater og de andre koder, sandsynligvis grundet manglen på parallel dynamik i HESEL. Men disse forskelle efterlades til videre undersøgelser.

Koden blev også brugt til at undersøge dynamikken af blobs for fuldt ioniserede plasmaer, hvor tidligere simuleringer har vist god overenstemmelse med eksperimentelle resultater. Det blev vist at endelig ion-temperatur har en betydelig effekt på blobbens dynamik, hvor det forårsager både hurtigere radiel bevægelse, men også forårsager bevægelse i den poloidale retning, som ikke blev set for lave ion temperaturer. Endeligt blev de maksimale radielle hastiheder, fundet med HESEL, sammenlignet med forskellige skaleringslove for varierende begyndelsesbetingelser for blobsene og det blev vist at ingen af de teoretisk fundne modeller passede med det observederede in simulationerne. Især når blob amplituden blev øget, var der stor forskel mellem teorien og simuleringerne, hvor simuleringerne tilsyneladende skalerede lineært, og de teoretiske modeller forudsage en afhængighed, der skalerede som en kvadratrod. Denne forskel efterlades også til videre undersøgelser.

Contents

| | | |
|----------|--|-----------|
| 1 | Introduction | 1 |
| 1.1 | Background | 1 |
| 1.2 | Purpose | 4 |
| 2 | Theory | 5 |
| 2.1 | The Braginskii Two-Fluid Model | 5 |
| 2.1.1 | The Boltzmann equation | 5 |
| 2.1.2 | The two-fluid equations | 7 |
| 2.1.3 | Weakly ionized plasma | 8 |
| 2.1.4 | Fully ionized plasma | 12 |
| 2.2 | Instabilities | 14 |
| 2.2.1 | Interchange instability | 15 |
| 2.2.2 | Resistive drift waves | 18 |
| 2.2.3 | Effect of drift waves | 20 |
| 3 | Numerical methods | 24 |
| 3.1 | The HESEL code | 24 |
| 3.2 | Definition of blob position | 27 |
| 4 | Simulation results | 31 |
| 4.1 | Weakly ionized plasma | 31 |
| 4.1.1 | Simulation parameters | 32 |
| 4.1.2 | Comparisons with experimental values | 34 |
| 4.1.3 | Comparison with BOUT++ and GBS | 37 |
| 4.2 | Fully ionized plasma | 41 |
| 4.2.1 | Simulation parameters | 41 |
| 4.2.2 | Blob behaviour | 42 |
| 4.2.3 | Scaling laws | 47 |
| 5 | Conclusion | 52 |
| 5.1 | Outlook | 54 |

| | |
|---|------------|
| A Appendix A | I |
| A.1 Derivations | I |
| A.1.1 Derivation of the parallel velocity for a weakly ionized plasma | I |
| A.1.2 Derivation of the lowest order perpendicular velocity for a weakly ionized plasma | I |
| A.1.3 Derivation of first order perpendicular velocity for a weakly ionized plasma | II |
| A.1.4 Derivations of gradients for a weakly ionized plasma | II |
| A.1.5 Derivation of first order perpendicular velocity for a fully ionized plasma | III |
| A.1.6 Derivation of the stress-tensor for a fully ionized plasma | III |
| A.1.7 Derivation of dispersion relation | IV |
| A.1.8 Derivation of the finite difference scheme | V |
| B Appendix B | VII |
| B.1 Matlab Scripts | VII |
| B.1.1 VelocityCalc.m | VII |

Chapter 1

Introduction

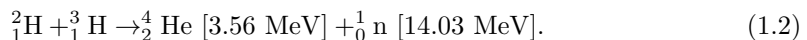
During recent years a lot of focus has been on the growing energy demand, which has lead to an increase in the consumption of fossil fuels, polluting the air and expelling vast amounts of greenhouse gases, resulting in global warming. Therefore a lot of research and different propositions for alternative sustainable energy sources have been made, the most prominent being solar cells and wind power. However these renewable energy sources do not produce electricity unless the wind is blowing or the sun is shining, which is not always when it is needed. A suggestion to overcome these limitations is by the process of controlled fusion, which fuses hydrogen into helium with a large benefit in output energy.

1.1 Background

Fusion is the process that takes place in the core of the sun, which generates the light and warmth we experience on earth. This is caused by two hydrogen nuclei colliding, creating helium. However, the mass of the helium is not exactly equal to that of the two hydrogen nuclei. A tiny bit of mass is lost in the process and is converted to a large amount of energy following Einsteins equation[1]

$$E = mc^2, \quad (1.1)$$

where c is the speed of light. The temperature at which the fusion in the sun takes place is around 15×10^6 °C, however this fusion process is also a result of large gravitational forces and resulting high densities, which are not present on earth. In order to achieve fusion on earth, it is therefore necessary to heat the reactants in the fusion process to much higher temperatures than the fusion process in the core of the sun, in order to overcome coulomb repulsion, necessary for the fusion to take place[1]. The most energetic outcome at the lowest temperature for a fusion reaction in a fusion power plant is that of deuterium, which is abundant on earth (0.0156% of the water on earth[2]), fusing with tritium (which can be obtained from lithium, a common metal) in the reaction[3]



The outcome of the suggested fusion reaction is charged α -particles and uncharged neutrons. Due to the extreme temperatures required for this process to take place, electrons and ions are separated, creating an electrically charged plasma, which can be confined, e.g. by using a magnetic field. The neutrons from the reaction leave the plasma without interaction and can be used to produce steam, driving a turbine and producing electricity like in a conventional power plant, but the helium is confined by the magnetic field and transfers

energy to the plasma through collisions. The reaction power per unit volume for the α -particles is given by[4]

$$P_\alpha = \frac{1}{4} n^2 \langle \sigma v \rangle E_\alpha, \quad (1.3)$$

where n is the density of the plasma, E_α is the energy from the α -particles produced by the fusion reaction and $\langle \sigma v \rangle$ is the reaction rate given by

$$\langle \sigma v \rangle = \left(\frac{8}{\pi} \right)^{1/2} \left(\frac{\mu}{T} \right)^{3/2} \frac{1}{m_d^2} \int \sigma(\epsilon) \epsilon \exp \left(-\frac{\mu \epsilon}{2T} \right) d\epsilon, \quad (1.4)$$

where μ is the reduced mass given by

$$\mu = \frac{m_d m_t}{m_d + m_t}, \quad (1.5)$$

$m_{d,t}$ is the mass of deuterium and tritium, respectively, T is the temperature and ϵ is the thermal energy. The fusion cross-section $\sigma(\epsilon)$ is a function of temperature and is usually found experimentally and different approximate expressions are found in the literature.

The overall power balance of the fusion reaction is given by the power supplied plus the power provided by the α -particles, which must be equal to the loss in the system. Assuming constant temperature and densities, this criterion is given as[4]

$$P_H = \left(\frac{3nT}{\tau_E} - \frac{1}{4} n^2 \langle \sigma v \rangle E_\alpha \right) V, \quad (1.6)$$

where P_H is the power supplied, n is the plasma density, T is the temperature, τ_E is the energy confinement time, and V is the volume of the plasma.

Thus in order for the plasma burn to be self-sustaining, the supplied power, P_H , must be less than or equal to zero. This criterion is known as ignition, and in order to achieve it, the following inequality needs to be fulfilled

$$n\tau_E > \frac{12T}{\langle \sigma v \rangle E_\alpha}. \quad (1.7)$$

A plot of $n\tau_E$ as a function of the temperature in keV is seen in Figure 1.1.

An approximate value for the reaction rate seen in Eq. (1.4), is given by[4]

$$\langle \sigma v \rangle = 1.1 \times 10^{-24} T^2 \text{m}^3 \text{s}^{-1}, \quad T \text{ in keV}, \quad (1.8)$$

in the temperature range 10-20 keV. Using this, an approximate criterion for ignition is given by

$$Tn\tau_E > 3 \times 10^{21} \text{ m}^{-3} \text{keV}, \quad (1.9)$$

which could be reached for example for $n = 10^{20} \text{ m}^{-3}$, $\tau_E = 3 \text{ s}$ and $T = 10 \text{ keV}$, which corresponds to 100 mio. °C.

Since the requirements for fusion are so specific, it is important to maintain a steady pressure and temperature of the plasma over an extended time-period to be able to harvest energy from the fusion reaction. This has not yet been achieved, and the main reason is that no materials can withstand temperatures of up to 100 mio. °C, which is where the optimal criterion for fusion is achieved (see Figure 1.1), so the reactants must be confined by other means. As previously mentioned, the gas becomes so warm that electrons are separated from the ions at these temperatures, creating an electrically charged plasma, which can be confined by using a magnetic field. However, there are several technical difficulties related to the magnetic confinement of plasmas, and various devices have been proposed. The most

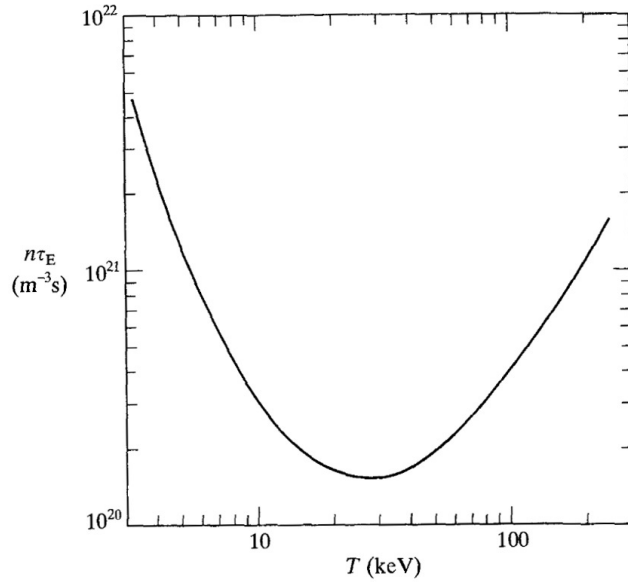


Figure 1.1: The value of $n\tau_E$ as a function of temperature required for ignition[4].

successful device this far has been the tokamak, a toroidal magnetic confinement device developed in the 1950's by soviet scientists[4].

The tokamak confines the plasma using a toroidal magnetic field induced by coils around the main reactor chamber. However this is not sufficient to contain the plasma, so a poloidal field is also applied, mainly induced by the plasma itself, moving in a toroidal direction as illustrated in Figure 1.2.

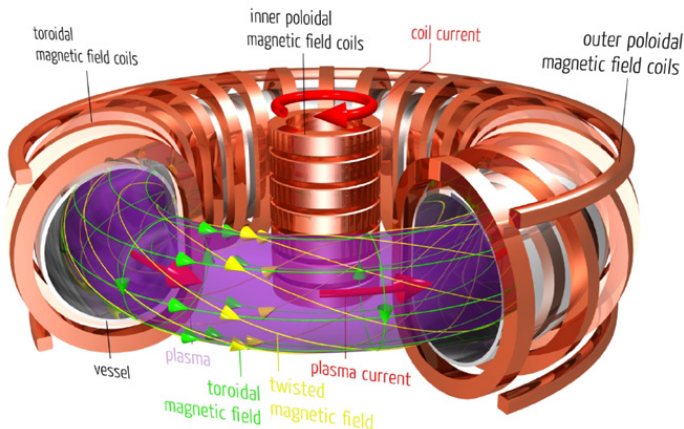


Figure 1.2: An illustration of the principles of a tokamak. The toroidal magnetic field lines (green), which are necessary for the confinement of the plasma (purple) are created by a current in the inner coil and the moving plasma (red). This, along with the toroidal magnetic field creates the twisted magnetic field lines (yellow), necessary for confinement[5].

Due to the curvature of the magnetic field in a tokamak and small density and potential fluctuations, the plasma develops instabilities. Parts of the plasma accumulates due to these fluctuations, and since both the density and the electric field decrease radially, these instabilities propagate out of the confinement region of closed magnetic field-lines, also known as

the last closed flux surface (LCFS), and travels towards the wall of the fusion reactor. This gives rise to problems such as erosion of the main chamber walls and steady-state operation parameters like main chamber recycling, material mitigation, plasma rotation and density disruption limit[6].

The main cause of radial transport in the region of open field lines of a tokamak, also known as the scrape-off layer (SOL), is expected to be due to this so-called interchange instability and the transport of coherent structures, also known as blobs.

1.2 Purpose

Due to the importance of blobs in the radial transport of the plasma, a lot of effort is put into understanding this phenomenon. The main purpose of this thesis is therefore to investigate the dynamics of these coherent structures in a magnetically confined fusion plasma.

Initially, in chapter 2, the equations describing the main concepts behind radial transport in both weakly and fully ionized, magnetically confined plasmas are investigated and the concepts behind different instabilities are described.

Then, in chapter 3, a brief discussion of the code used to simulate blob propagation is given and different methods for calculating positions and velocities of blobs are described.

Next, in chapter 4, simulation results are presented for two different regimes. One for a weakly ionized plasma and one for a fully ionized plasma. The first simulations examined are for the weakly ionized plasma, which are compared with experimental results from the TORPEX device in Lausanne and with results from other codes using the same parameters. The other simulations investigated are for the fully ionized plasma, which are used to investigate the effects of warm ions in the HESEL code, and finally used to compare with different scaling laws for the maximum velocity of the blob with different initial parameters. Finally, in chapter 5, a conclusion is presented and an outlook for future projects is given.

Since the instabilities causing radial transport mainly occur in the outboard mid-plane when considering a toroidal magnetic fusion device, a small square in the outboard mid-plane is investigated throughout the project. The area considered, and the coordinates used, unless otherwise specified, are seen in Figure 1.3. Finally it should be noted that the scope of this project has been to investigate the structures using a 2D domain, so effects parallel to the magnetic field are only briefly mentioned.

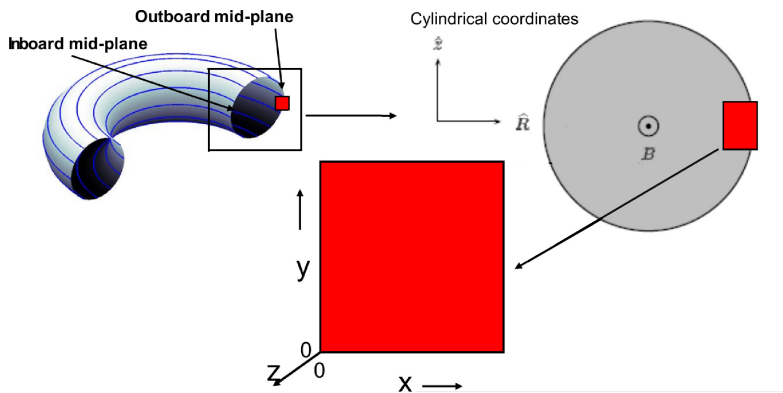


Figure 1.3: A sketch of the cross-section investigated in the project. The major radius of the torus is given by R_0 , the minor radius by r_0 , the magnetic field is assumed along the torus and is pointed out of the paper[7].

Chapter 2

Theory

Before looking at the simulations of seeded blobs in magnetically confined plasmas, it is fruitful to investigate the qualitative behaviour of plasma particles in a magnetic field and instabilities caused by small fluctuations in plasma density and potential. In this chapter, the so-called two-fluid equations are derived, followed by an analysis of weakly and fully ionized plasmas, and finally instabilities in different regimes are investigated.

2.1 The Braginskii Two-Fluid Model

Most simulation models describing magnetically confined plasmas solve the Braginskii two-fluid equations, so in order to better understand the theory behind the codes, a simple two-fluid model is derived, and different regimes are investigated.

2.1.1 The Boltzmann equation

To describe the effect of small fluctuations in a magnetically confined plasma, it is first necessary to develop the governing equations for the motion of the plasma. Initially particles are described using a phase-space diagram as shown in Figure 2.1[8].

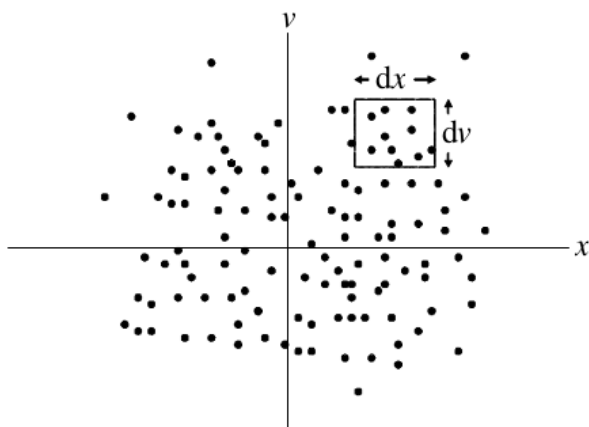


Figure 2.1: An illustration of the phase-space diagram used to visualize the particles in a plasma. The y -axis is the velocity, v , and the x -axis is the position, x .

Since all particles at any given time have a given position and velocity, they can be described by the instantaneous density of particles using a distribution function, denoted by $f(x, v, t)$ ¹. Defining a small box with the width dx and the height dv in the phase-space diagram as shown in Figure 2.1, the evolution of the PDF can be found by considering the flux into and out of the box. Defining $a(x, v, t)$ as the acceleration of the particles, the rates at which the flux enters and exits the box are given by[8];

- The flux into the left side of the box is $f(x, v, t)v dv$.
- The flux into the right side of the box is $-f(x + dx, v, t)v dv$.
- The flux into the bottom of the box is $f(x, v, t)a(x, v, t)dx$.
- The flux into the top of the box is $-f(x, v + dv, t)a(x, v + dv, t)dx$.

Combining these into a master equation describing the change of the PDF with time, the rate of change into the small box is found to be

$$\begin{aligned} \frac{\partial f(x, v, t)}{\partial t} dx dv &= -f(x + dx, v, t)v dv + f(x, v, t)v dv \\ &\quad - f(x, v + dv, t)a(x, v + dv, t)dx + f(x, v, t)a(x, v, t)dx. \end{aligned} \quad (2.1)$$

Next the right-hand side (RHS) is Taylor-expanded, which gives:

$$-f(x + dx, v, t)v dv \approx -f(x, v, t)v dv - v \frac{\partial f(x, v, t)}{\partial x} dv dx$$

and

$$\begin{aligned} -f(x, v + dv, t)a(x, v + dv, t)dx &\approx -f(x, v, t)a(x, v, t)dx - a(x, v, t) \frac{\partial f(x, v, t)}{\partial v} dx dv \\ &\quad - f(x, v, t) \frac{\partial a(x, v, t)}{\partial v} dx dv \\ &\approx -f(x, v, t)a(x, v, t)dx - \frac{\partial(f(x, v, t)a(x, v, t))}{\partial v} dx dv. \end{aligned}$$

Inserting this into the master equation (Eq. (2.1)) and dividing by $dx dv$, the so-called one-dimensional Vlasov equation is obtained

$$\frac{\partial}{\partial t} f(x, v, t) + v \frac{\partial}{\partial x} f(x, v, t) + \frac{\partial}{\partial v} (f(x, v, t)a(x, v, t)) = 0, \quad (2.2)$$

which is easily expanded to 3D[8],

$$\frac{\partial}{\partial t} f(\mathbf{x}, \mathbf{v}, t) + \mathbf{v} \cdot \frac{\partial}{\partial \mathbf{x}} f(\mathbf{x}, \mathbf{v}, t) + \frac{\partial}{\partial \mathbf{v}} (f(\mathbf{x}, \mathbf{v}, t) \cdot \mathbf{a}(\mathbf{x}, \mathbf{v}, t)) = 0. \quad (2.3)$$

Since \mathbf{v} is independent of \mathbf{x} in phase-space, Eq. (2.3) can be rewritten as

$$\frac{\partial}{\partial t} f(\mathbf{x}, \mathbf{v}, t) + \frac{\partial}{\partial \mathbf{x}} \cdot (\mathbf{v} f(\mathbf{x}, \mathbf{v}, t)) + \frac{\partial}{\partial \mathbf{v}} (f(\mathbf{x}, \mathbf{v}, t) \cdot \mathbf{a}(\mathbf{x}, \mathbf{v}, t)) = 0. \quad (2.4)$$

However this equation does not take collisions into account, so in order to describe these, a collision operator is introduced[8], which finally gives the so-called Boltzmann equation

$$\frac{\partial f_\sigma}{\partial t} + \frac{\partial}{\partial \mathbf{x}} \cdot (\mathbf{v} f_\sigma) + \frac{\partial}{\partial \mathbf{v}} \cdot (\mathbf{a} f_\sigma) = \sum_\alpha C_{\sigma\alpha}(f_\sigma), \quad (2.5)$$

where σ and α indicate species (ions or electrons). The collision operator needs to be subjected to the following requirements

¹Also known as a probability distribution function, PDF, since it describes the probability of finding a particle with the velocity, v , at a given position, x , and time, t .

- $\int d\mathbf{v} C_{\sigma\alpha}(f_\sigma) = 0$, the total number of particles must be conserved.
- $\int d\mathbf{v} m_\sigma \mathbf{v} C_{\sigma\sigma}(f_\sigma) = 0$, the momentum of each species must be conserved. Collisions between the same kind of particles cannot change the total momentum of that species.
- $\int d\mathbf{v} m_i \mathbf{v} C_{ie}(f_i) + \int d\mathbf{v} m_e \mathbf{v} C_{ei}(f_e) = 0$, the total momentum must be conserved.
- $\int d\mathbf{v} m_\sigma v^2 C_{\sigma\sigma}(f_\sigma) = 0$, the energy of each species must be conserved. Collision between same species cannot change the energy of this species.
- $\int d\mathbf{v} m_i v^2 C_{ie}(f_i) + \int d\mathbf{v} m_e v^2 C_{ei}(f_e) = 0$, the total energy must be conserved.

2.1.2 The two-fluid equations

From the Boltzmann equation (Eq. (2.5)), which describes the evolution of a collection of particles with respect to time, it is possible to derive the so-called two-fluid equations. The first step to doing this is by taking the moments of the distribution function, given by

$$\text{0th moment: } n(\mathbf{x}, t) = \int f(\mathbf{x}, \mathbf{v}, t) d\mathbf{v} \quad (2.6)$$

$$\text{1st moment: } \mathbf{u}(\mathbf{x}, t) = \frac{\int \mathbf{v} \cdot f(\mathbf{x}, \mathbf{v}, t) d\mathbf{v}}{n(\mathbf{x}, t)} \quad (2.7)$$

where $n(\mathbf{x}, t)$ is the density of the distribution function and $\mathbf{u}(\mathbf{x}, t)$ is the mean velocity of the particles in the plasma, also called the fluid velocity.

The next step is taking the moments of the entire Boltzmann equation. The 0th moment, also known as the continuity equation, is obtained by multiplying Eq. (2.5) by $\mathbf{v}^0 = 1$ and integrating it over all \mathbf{v} . Using that \mathbf{a} is the acceleration resulting from the Lorentz force $\mathbf{a} = (\mathbf{E} + \mathbf{v} \times \mathbf{B})/m$ and thus commutes² with $\partial/\partial\mathbf{v}$, the 0th moment equation is found to be

$$\begin{aligned} \int \left[\frac{\partial f_\sigma}{\partial t} + \mathbf{v} \frac{\partial f_\sigma}{\partial \mathbf{x}} + \mathbf{a} \frac{\partial f_\sigma}{\partial \mathbf{v}} \right] d\mathbf{v} &= \frac{\partial}{\partial t} \int f_\sigma d\mathbf{v} + \nabla_{\mathbf{x}} \cdot \int \mathbf{v} f_\sigma d\mathbf{v} + \int \mathbf{a} \nabla_{\mathbf{v}} f_\sigma d\mathbf{v} \\ &= \frac{\partial}{\partial t} n_\sigma(\mathbf{x}, t) + \nabla_{\mathbf{x}} n_\sigma(\mathbf{x}, t) \mathbf{u}_\sigma(\mathbf{x}, t) + \int_S \mathbf{a} \cdot d\mathbf{s} \cdot f_\sigma \\ &= \frac{\partial}{\partial t} n_\sigma(\mathbf{x}, t) + \nabla n_\sigma(\mathbf{x}, t) \mathbf{u}_\sigma(\mathbf{x}, t) = \int \sum_\alpha C_{\sigma\alpha}(f_\sigma) d\mathbf{v} \\ &= \frac{\partial}{\partial t} n_\sigma(\mathbf{x}, t) + \nabla n_\sigma(\mathbf{x}, t) \mathbf{u}_\sigma(\mathbf{x}, t) = 0 \\ &= \left(\frac{\partial}{\partial t} + \mathbf{u}_\sigma(\mathbf{x}, t) \cdot \nabla \right) n_\sigma(\mathbf{x}, t) + n_\sigma(\mathbf{x}, t) \nabla \cdot \mathbf{u}_\sigma(\mathbf{x}, t) = 0, \end{aligned} \quad (2.8)$$

where, in the second line, Eq.'s (2.6) and (2.7), and Gauss' theorem have been used, and in the third line it has been used that $f \rightarrow 0$ at the surface as $v \rightarrow \infty$ and $\int \sum_\alpha C_{\sigma\alpha}(f_\sigma) d\mathbf{v} = 0$ due to conservation of particles.

In the same way it is possible to find the first moment of the Boltzmann equation, by multiplying the entire equation (Eq. (2.5)) by \mathbf{v} and taking the integral over all \mathbf{v} . The derivation is rather lengthy and can be found in [8], so it is omitted here. The result, is

$$n_\sigma m_\sigma \left(\frac{\partial}{\partial t} + \mathbf{u}_\sigma \cdot \nabla \right) \mathbf{u}_\sigma = n_\sigma q_\sigma (\mathbf{E} + \mathbf{u}_\sigma \times \mathbf{B}) - \nabla \cdot \overleftrightarrow{\mathbf{P}}_\sigma - \mathbf{R}_{\sigma\alpha}, \quad (2.9)$$

² \mathbf{a} actually depends on \mathbf{v} , but since it is a cross-product, a_i does not depend on v_i and it thus commutes with the vectorial partial derivative

where $\overleftrightarrow{\mathbf{P}}_\sigma$ is the pressure tensor given by $m_\sigma \int \mathbf{v}' \cdot \mathbf{v}' f_\sigma d\mathbf{v}'$, with \mathbf{v}' being the random part of the velocity and $\mathbf{R}_{\sigma\alpha} = \int \mathbf{v} C_{\sigma\alpha} f(\sigma) d\mathbf{v}$ using that $m_\sigma \int \mathbf{v} C_{\sigma\sigma} d\mathbf{v} = 0$. Furthermore the pressure tensor can be split into a scalar part p_σ , and a stress tensor $\mathbf{\Pi}_\sigma$, so $\overleftrightarrow{\mathbf{P}}_\sigma = p_\sigma + \mathbf{\Pi}_\sigma$. Inserting this, and defining the convective derivative as

$$\frac{d}{dt} = \left(\frac{\partial}{\partial t} + \mathbf{u}_\sigma \cdot \nabla \right) \quad (2.10)$$

the equations for the 0'th and first moment become

$$\frac{d}{dt} n_\sigma + n_\sigma \nabla \cdot \mathbf{u}_\sigma = 0, \quad (2.11)$$

$$n_\sigma m_\sigma \frac{d}{dt} \mathbf{u}_\sigma = n_\sigma q_\sigma (\mathbf{E} + \mathbf{u}_\sigma \times \mathbf{B}) - \nabla p_\sigma - \nabla \cdot \mathbf{\Pi}_\sigma - \mathbf{R}_{\sigma\alpha}, \quad (2.12)$$

known as the two-fluid equations, which can be used to investigate the motion of a magnetically confined plasma.

2.1.3 Weakly ionized plasma

To analyse the two-fluid equations, the properties of a weakly ionized plasma are initially examined, where the following assumptions are made:

- Low frequency dynamics, $\omega \ll \omega_{c\sigma} \equiv q_\sigma B / m_\sigma$, where $\omega_{c\sigma}$ is the species cyclotron frequency, which means that d/dt is small, since it is of the order ω .
- Partially ionized plasma, so collisions between the fluid species σ and a stationary neutral gas are the dominating dissipation terms, which means that all collisions between ions and electrons are neglected and $\mathbf{u}_n = 0$.
- Electrostatic \mathbf{E} -field, i.e. $\mathbf{E} = -\nabla\phi$.
- Isothermal fluid species, so the pressure is given by $p_\sigma = n_\sigma T_\sigma$, where T_σ is the temperature of the species in units of energy and is assumed constant.
- $p_\sigma \gg \mathbf{\Pi}_\sigma$, so only the isotropic pressure is retained.
- Weakly collisional, which means that the collision frequency $\nu_{\sigma n} \ll \omega_{c\sigma}$.

With these assumptions Eq. (2.12) can be split into a parallel and a perpendicular part with respect to the magnetic field, which gives

$$n_\sigma m_\sigma \left(\frac{\partial}{\partial t} + \mathbf{u}_{\sigma\parallel} \cdot \nabla_{\parallel} \right) \mathbf{u}_{\sigma\parallel} = n_\sigma q_\sigma \mathbf{E}_{\parallel} - \nabla_{\parallel} p_\sigma - \mathbf{R}_{\sigma\alpha\parallel} \quad (2.13)$$

$$n_\sigma m_\sigma \left(\frac{\partial}{\partial t} + \mathbf{u}_{\sigma\perp} \cdot \nabla_{\perp} \right) \mathbf{u}_{\sigma\perp} = n_\sigma q_\sigma (\mathbf{E}_{\perp} + \mathbf{u}_{\sigma\perp} \times \mathbf{B}) - \nabla_{\perp} p_\sigma - \mathbf{R}_{\sigma\alpha\perp} \quad (2.14)$$

The collision term is given as [8] $\nu_{\sigma n} m_\sigma n_\sigma (\mathbf{u}_\sigma - \mathbf{u}_n)$, where $\nu_{\sigma n}$ is the collision frequency between species σ and neutrals. Inserting this in Eq. (2.13) and (2.14) leads to the equations for the parallel and perpendicular fluid velocities

$$n_\sigma m_\sigma \left(\frac{\partial}{\partial t} + \mathbf{u}_{\sigma\parallel} \cdot \nabla_{\parallel} \right) \mathbf{u}_{\sigma\parallel} = n_\sigma q_\sigma \mathbf{E}_{\parallel} - \nabla_{\parallel} p_\sigma - \nu_{\sigma n} m_\sigma n_\sigma \mathbf{u}_{\sigma\parallel} \quad (2.15)$$

$$n_\sigma m_\sigma \left(\frac{\partial}{\partial t} + \mathbf{u}_{\sigma\perp} \cdot \nabla_{\perp} \right) \mathbf{u}_{\sigma\perp} = n_\sigma q_\sigma (\mathbf{E}_{\perp} + \mathbf{u}_{\sigma\perp} \times \mathbf{B}) - \nabla_{\perp} p_\sigma - \nu_{\sigma n} m_\sigma n_\sigma \mathbf{u}_{\sigma\perp}. \quad (2.16)$$

These equations can be solved iteratively to find an expression for the fluid velocities of the different species, necessary in order to explain the behaviour of a weakly ionized, magnetically confined plasma.

Fluid velocities

In order to find the fluid velocities resulting from Eq. (2.15) and (2.16), an order of magnitude estimate is performed based on the definitions given.

From Eq. (2.15), the parallel fluid velocity is found to be³

$$\mathbf{u}_{\sigma\parallel} = \frac{T_{\sigma}}{m_{\sigma}\nu_{\sigma n}} \nabla_{\parallel} \left(\frac{-q_{\sigma}\phi}{T_{\sigma}} - \ln n_{\sigma} \right), \quad (2.17)$$

to lowest order in ϵ , where ϵ is a small parameter.

The perpendicular velocity is found by writing $\mathbf{u}_{\sigma\perp}$ as a term on the order of ϵ^0 and a term on the order of ϵ^1 , so $\mathbf{u}_{\sigma\perp} = \mathbf{u}_{\sigma\perp 0} + \mathbf{u}_{\sigma\perp 1}$, where $\mathbf{u}_{\sigma\perp 1}$ is a small perturbation on the order of $\epsilon\mathbf{u}_{\sigma\perp 0}$. Solving Eq. (2.16) to lowest order gives⁴

$$\mathbf{u}_{\sigma\perp 0} = -\frac{\nabla_{\perp}\phi \times \mathbf{B}}{B^2} - \frac{T_{\sigma}}{q_{\sigma}B^2} \nabla_{\perp} \ln n_{\sigma} \times \mathbf{B}. \quad (2.18)$$

$\mathbf{u}_{\sigma\perp 1}$ is found by going to the next order in Eq. (2.16) and including terms on the order of ϵ . This gives⁵

$$\mathbf{u}_{\sigma\perp 1} = \frac{m_{\sigma}T_{\sigma}}{q_{\sigma}^2B^2} \frac{d}{dt} \nabla_{\perp} \left(\frac{-q_{\sigma}\phi}{T_{\sigma}} - \ln n_{\sigma} \right) + \frac{\nu_{\sigma n}m_{\sigma}T_{\sigma}}{q_{\sigma}^2B^2} \nabla_{\perp} \left(\frac{-q_{\sigma}\phi}{T_{\sigma}} - \ln n_{\sigma} \right) \quad (2.19)$$

Collecting both the lowest order parallel component and the lowest two orders of the perpendicular component, an equation for the fluid motion of each species is obtained,

$$\begin{aligned} \mathbf{u}_{\sigma} = & -\frac{\nabla_{\perp}\phi \times \mathbf{B}}{B^2} - \frac{T_{\sigma}}{q_{\sigma}B^2} \nabla_{\perp} \ln n_{\sigma} \times \mathbf{B} + \frac{m_{\sigma}T_{\sigma}}{q_{\sigma}^2B^2} \frac{d}{dt} \nabla_{\perp} \left(\frac{-q_{\sigma}\phi}{T_{\sigma}} - \ln n_{\sigma} \right) \\ & + \frac{\nu_{\sigma n}m_{\sigma}T_{\sigma}}{q_{\sigma}^2B^2} \nabla_{\perp} \left(\frac{-q_{\sigma}\phi}{T_{\sigma}} - \ln n_{\sigma} \right) + \frac{T_{\sigma}}{m_{\sigma}\nu_{\sigma n}} \nabla_{\parallel} \left(\frac{-q_{\sigma}\phi}{T_{\sigma}} - \ln n_{\sigma} \right), \end{aligned} \quad (2.20)$$

Neglecting inertia effects for electrons, the equation for the motion of electrons is given by

$$\mathbf{u}_e = -\frac{\nabla_{\perp}\phi \times \mathbf{B}}{B^2} + \frac{T_e}{eB^2} \nabla_{\perp} \ln n_e \times \mathbf{B} + \frac{\nu_{en}T_e}{\omega_{ce}eB} \nabla_{\perp} \left(\frac{e\phi}{T_e} - \ln n_e \right) + \frac{T_e\omega_{ce}}{\nu_{en}eB} \nabla_{\parallel} \left(\frac{e\phi}{T_e} - \ln n_e \right). \quad (2.21)$$

Assuming that the ions only move in the perpendicular direction and neglecting diamagnetic effects, the equation for the motion of ions is given by

$$\mathbf{u}_i = -\frac{\nabla_{\perp}\phi \times \mathbf{B}}{B^2} - \frac{T_i}{\omega_{ci}eB} \frac{d}{dt} \nabla_{\perp} \left(\frac{e\phi}{T_i} + \ln n_i \right) - \frac{\nu_{in}T_i}{\omega_{ci}eB} \nabla_{\perp} \left(\frac{e\phi}{T_i} + \ln n_i \right). \quad (2.22)$$

To simplify future calculations, the following definitions are made;

$$\mathbf{u}_E = -\frac{\nabla_{\perp}\phi \times \mathbf{B}}{B^2}, \quad (2.23)$$

$$\mathbf{u}_{di} = -\frac{T_i}{eB^2} \nabla_{\perp} \ln n_i \times \mathbf{B}, \quad \mathbf{u}_{de} = \frac{T_e}{eB^2} \nabla_{\perp} \ln n_e \times \mathbf{B} \quad (2.24)$$

$$\mathbf{u}_{pi} = \frac{T_i}{\omega_{ci}eB} \frac{d}{dt} \nabla_{\perp} \left(\frac{-e\phi}{T_i} - \ln n_i \right), \quad \mathbf{u}_{pe} = \frac{T_e}{\omega_{ce}eB} \frac{d}{dt} \nabla_{\perp} \left(\frac{e\phi}{T_e} - \ln n_e \right), \quad (2.25)$$

where \mathbf{u}_E is identified as the $\mathbf{E} \times \mathbf{B}$ -drift, $\mathbf{u}_{d\sigma}$ is the diamagnetic drift and $\mathbf{u}_{p\sigma}$ is the polarization drift[9]. Since electron inertia effects and ion diamagnetic effects are neglected[9], \mathbf{u}_{pe} and \mathbf{u}_{di} are assumed to be 0.

³See appendix A.1.1 for the derivation.

⁴See appendix A.1.2 for the derivation.

⁵See appendix A.1.3 for the derivation.

Continuity equations

To derive the governing equations for a weakly ionized plasma, the fluid velocities, Eq. (2.21) and (2.22), are inserted in the continuity equation, Eq. (2.11). This gives the electron and ion continuity equations

$$\begin{aligned} \frac{\partial}{\partial t} n_e + \nabla \left(n_e \left(\mathbf{u}_E + \mathbf{u}_{de} + \frac{\nu_{en} T_e}{\omega_{ce} e B} \nabla_{\perp} \left(\frac{e\phi}{T_e} - \ln n_e \right) + \frac{T_e \omega_{ce}}{\nu_{en} e B} \nabla_{\parallel} \left(\frac{e\phi}{T_e} - \ln n_e \right) \right) \right) &= 0 \\ \frac{d}{dt} \ln n_e + (\nabla \ln n_e + \nabla) \cdot \left(\frac{\nu_{en} T_e}{\omega_{ce} e B} \nabla_{\perp} \left(\frac{e\phi}{T_e} - \ln n_e \right) + \frac{T_e \omega_{ce}}{\nu_{en} e B} \nabla_{\parallel} \left(\frac{e\phi}{T_e} - \ln n_e \right) \right) &+ \nabla \cdot (\mathbf{u}_E + \mathbf{u}_{de}) = 0, \end{aligned} \quad (2.26)$$

and

$$\begin{aligned} \frac{\partial}{\partial t} n_i + \nabla \left(n_i \left(\mathbf{u}_E + \mathbf{u}_{pi} - \frac{\nu_{in} T_i}{\omega_{ci} e B} \nabla_{\perp} \left(\frac{e\phi}{T_i} + \ln n_i \right) \right) \right) &= 0 \\ \Rightarrow \frac{d}{dt} \ln n_i + (\nabla \ln n_i + \nabla) \cdot \left(\mathbf{u}_{pi} - \frac{\nu_{in} T_i}{\omega_{ci} e B} \nabla_{\perp} \left(\frac{e\phi}{T_i} + \ln n_i \right) \right) + \nabla \cdot \mathbf{u}_E &= 0, \end{aligned} \quad (2.27)$$

where, from the first to the second line, the definition of the convective derivative, Eq. (2.10) with \mathbf{u}_E instead of \mathbf{u}_{σ} , is used, and where, in the electron continuity equation, it is used that $\nabla \ln n_e \cdot \nabla \ln n_e \times \mathbf{B} = 0$. Assuming a purely toroidal magnetic field, $\mathbf{B} = (B_0 R_0 / R) \mathbf{b}$ as in [9] where $\mathbf{b} = \mathbf{B}/B$ is a unit vector in the negative azimuthal direction, B_0 is the magnetic field at the major radius R_0 and $R = R_0 + L + x$ with L being the minor radius, the last terms in Eq. (2.26) and (2.27) are given by⁶

$$\nabla \cdot \mathbf{u}_E = -\frac{2}{BR} \hat{\mathbf{z}} \cdot \nabla_{\perp} \phi \quad (2.28)$$

and

$$\nabla \cdot \mathbf{u}_{de} = \frac{2T_e}{eBR} \hat{\mathbf{z}} \cdot \nabla_{\perp} \ln n_e. \quad (2.29)$$

Inserting these, the electron continuity equation, Eq. (2.26), becomes

$$\begin{aligned} \frac{d}{dt} \ln n_e + (\nabla \ln n_e + \nabla) \cdot \left(\frac{\nu_{en} T_e}{\omega_{ce} e B} \nabla_{\perp} (\varphi - \ln n_e) + \frac{T_e \omega_{ce}}{\nu_{en} e B} \nabla_{\parallel} (\varphi - \ln n_e) \right) & \\ - \frac{2T_e}{eBR} \hat{\mathbf{z}} \cdot \nabla_{\perp} (\varphi - \ln n_e) &= 0, \end{aligned} \quad (2.30)$$

where $\varphi = \phi \frac{e}{T_e}$. Assuming cold ions, the ion continuity equation Eq. (2.27) becomes

$$\frac{d}{dt} \ln n_i - (\nabla \ln n_i + \nabla) \cdot \left(\frac{T_e}{e \omega_{ci} B} \frac{d}{dt} \nabla_{\perp} \varphi + \frac{\nu_{in} T_e}{\omega_{ci} e B} \nabla_{\perp} \varphi \right) - \frac{2T_e}{eBR} \hat{\mathbf{z}} \cdot \nabla_{\perp} \varphi = 0. \quad (2.31)$$

Assuming quasi-neutrality, $n_i \approx n_e \equiv n$, leads to the electron continuity equation

$$\begin{aligned} \frac{d}{dt} \ln n + (\nabla \ln n + \nabla) \cdot \left(\frac{\nu_{en} T_e}{\omega_{ce} e B} \nabla_{\perp} (\varphi - \ln n) + \frac{T_e \omega_{ce}}{\nu_{en} e B} \nabla_{\parallel} (\varphi - \ln n) \right) & \\ - \frac{2T_e}{eBR} \hat{\mathbf{z}} \cdot \nabla_{\perp} (\varphi - \ln n) &= 0, \end{aligned} \quad (2.32)$$

⁶See appendix A.1.4 for the derivation.

and the charge continuity equation, which is found by subtracting the ion continuity equation from the electron continuity equation becomes

$$\boxed{(\nabla \ln n + \nabla) \cdot \left(\frac{T_e}{e\omega_{ci}B} \frac{d}{dt} \nabla_{\perp} \varphi + \frac{\nu_{in}T_e}{\omega_{ci}eB} \nabla_{\perp} \varphi \right. \\ \left. + \frac{\nu_{en}T_e}{\omega_{ce}eB} \nabla_{\perp} (\varphi - \ln n) + \frac{T_e\omega_{ce}}{\nu_{en}eB} \nabla_{\parallel} (\varphi - \ln n) \right) + \frac{2T_e}{eBR} \hat{\mathbf{z}} \cdot \nabla_{\perp} \ln n = 0.} \quad (2.33)$$

These equations can be solved numerically in order to describe a magnetically confined plasma under the given assumptions.

Local approximation

Equations (2.32) and (2.33) can be solved numerically, however in order to give an analytical qualitative description of the plasma subjected to small perturbations, a local analysis is made, where the density is defined in terms of an equilibrium density profile, n_0 and a fluctuating plasma density \tilde{n} , so

$$n = n_0(x) + \tilde{n}(x, y, t) \quad (2.34)$$

Assuming that the characteristic length-scale of n_0 is L , and that the wavenumber of the fluctuations \tilde{n} is k , and further assuming that $\tilde{n} \ll n_0$ means that $\nabla n = \nabla n_0 + \nabla \tilde{n} = n_0/L + k\tilde{n}$. Furthermore it is assumed that all other gradients contribute with k , which means

$$\frac{\nabla \ln n}{\nabla} \propto \frac{n_0/L + k\tilde{n}}{n_0 k} = \frac{1}{kL} \left(1 + \frac{\tilde{n}}{n_0} \right) \ll 1, \quad (2.35)$$

so $\nabla \ln n$ is neglected in Eq. (2.32). and (2.33). Under this local assumption, the equations simplify to

$$\frac{d}{dt} \ln n + \frac{\nu_{en}T_e}{\omega_{ce}eB} \nabla_{\perp}^2 (\varphi - \ln n) + \frac{T_e\omega_{ce}}{\nu_{en}eB} \nabla_{\parallel}^2 (\varphi - \ln n) - \frac{2T_e}{eBR} \hat{\mathbf{z}} \cdot \nabla_{\perp} (\varphi - \ln n) = 0, \quad (2.36)$$

$$\frac{1}{\omega_{ci}} \frac{d}{dt} \nabla_{\perp}^2 \varphi + \frac{\nu_{in}}{\omega_{ci}} \nabla_{\perp}^2 \varphi + \frac{\nu_{en}}{\omega_{ce}} \nabla_{\perp}^2 (\varphi - \ln n) + \frac{\omega_{ce}}{\nu_{en}} \nabla_{\parallel}^2 (\varphi - \ln n) + \frac{2}{R} \hat{\mathbf{z}} \cdot \nabla_{\perp} \ln n = 0. \quad (2.37)$$

Now using the so-called Bohm normalization by introducing the normalized parameters $\nabla \rightarrow 1/\rho_s \nabla$, $\partial_t \rightarrow \omega_{ci} \partial_t$, where $\rho_s = c_s/\omega_{ci}$ is the gyration radius of the ions at the electron temperature, $c_s = (T_e/m_i)^{1/2}$ is the ion sound speed and defining $\xi = 2\rho_s/R$, $\nu_e = \nu_{en}/\omega_{ce}$, $\nu_i = \nu_{in}/\omega_{ci}$, and introducing the poisson-bracket $\{\phi, n\} = \mathbf{u}_E \cdot \nabla n$ Eq. (2.32) and (2.33) become[9]

$$\frac{\partial}{\partial t} \ln n + \{\varphi, \ln n\} + \nu_e \nabla_{\perp}^2 (\varphi - \ln n) + \nu_e^{-1} \nabla_{\parallel}^2 (\varphi - \ln n) - \xi \partial_y (\varphi - \ln n) = 0, \quad (2.38)$$

$$\frac{\partial}{\partial t} \nabla_{\perp}^2 \varphi + \{\varphi, \nabla_{\perp}^2 \varphi\} + \nu_i \nabla_{\perp}^2 \varphi + \nu_e \nabla_{\perp}^2 (\varphi - \ln n) + \nu_e^{-1} \nabla_{\parallel}^2 (\varphi - \ln n) + \xi \partial_y \ln n = 0. \quad (2.39)$$

Finally assuming an exponential density profile,

$$n_0 = n_{00} \exp(-x/L), \quad (2.40)$$

using the definition of n , so $\ln n = \ln(n_0(1 + \tilde{n}/n_0)) = \ln n_0 + \ln(1 + \tilde{n}/n_0) \equiv \ln n_0 + n$, defining the dimensionless vorticity $\nabla_\perp^2 \varphi$ as Ω and defining $\kappa = \rho_s/L$, the above governing equations for a thin-layer weakly ionized plasma are given by

$$\frac{\partial}{\partial t} n + \{\varphi, n\} + \nu_e \nabla_\perp^2 (\varphi - n) + \nu_e^{-1} \nabla_\parallel^2 (\varphi - n) + (\kappa - \xi) \frac{\partial}{\partial y} \varphi + \xi \frac{\partial}{\partial y} n = 0, \quad (2.41)$$

$$\frac{\partial}{\partial t} \Omega + \{\varphi, \Omega\} + \nu_i \Omega + \nu_e \nabla_\perp^2 (\varphi - n) + \nu_e^{-1} \nabla_\parallel^2 (\varphi - n) + \xi \frac{\partial}{\partial y} n = 0. \quad (2.42)$$

These coupled differential equations are used in section 2.2 to investigate stability criteria for a magnetically confined plasma. However it is interesting to first look at a fully ionized plasma, since this is the regime in which fusion takes place.

2.1.4 Fully ionized plasma

For a fully ionized plasma there are no neutrals for the electrons and ions to collide with, so the diffusive drifts are due to electron-ion collisions and ion viscosity[10]. This means that it is necessary to include the stress-tensor, Π_σ , in Eq. (2.12). Including Π_σ and assuming that $\mathbf{R}_{\sigma\alpha}$ consists only of a frictional force, so $\mathbf{R}_{\sigma\alpha} = \nu_{\sigma\alpha} m_\sigma n_\sigma (\mathbf{u}_\sigma - \mathbf{u}_\alpha)$ and splitting it into a parallel and a perpendicular part Eq. (2.12) becomes

$$n_\sigma m_\sigma \frac{d}{dt} \mathbf{u}_{\sigma\parallel} = n_\sigma q_\sigma \mathbf{E}_\parallel - \nabla_\parallel p_\sigma - \nabla_\parallel \Pi_\sigma - \nu_{\sigma\alpha} m_\sigma n_\sigma (\mathbf{u}_{\sigma\parallel} - \mathbf{u}_{\alpha\parallel}) \quad (2.43)$$

$$n_\sigma m_\sigma \frac{d}{dt} \mathbf{u}_{\sigma\perp} = n_\sigma q_\sigma (\mathbf{E}_\perp + \mathbf{u}_{\sigma\perp} \times \mathbf{B}) - \nabla_\perp p_\sigma - \nabla_\perp \Pi_\sigma - \nu_{\sigma\alpha} m_\sigma n_\sigma (\mathbf{u}_{\sigma\perp} - \mathbf{u}_{\alpha\perp}). \quad (2.44)$$

Using the same assumptions and approach as in section 2.1.3, and further assuming $\nabla_\parallel \Pi_\sigma \ll \nu_{\sigma\alpha} m_\sigma n_\sigma (\mathbf{u}_{\sigma\parallel} - \mathbf{u}_{\alpha\parallel})$, and that collisions and $\nabla_\perp \Pi_\sigma$ are of the order ϵ , where ϵ is a small parameter, the parallel fluid velocity, to lowest order, becomes

$$\mathbf{u}_{\sigma\parallel} - \mathbf{u}_{\alpha\parallel} = \frac{T_\sigma}{m_\sigma \nu_{\sigma\alpha}} \nabla_\parallel \left(\frac{-q_\sigma \phi}{T_\sigma} - \ln n_\sigma \right), \quad (2.45)$$

and the perpendicular fluid velocity to lowest order becomes

$$\mathbf{u}_{\sigma\perp 0} = -\frac{\nabla_\perp \phi \times \mathbf{b}}{B} - \frac{T_\sigma}{q_\sigma B} \nabla_\perp \ln n_\sigma \times \mathbf{b}. \quad (2.46)$$

Going to next order in Eq. (2.44) $\mathbf{u}_{\sigma\perp 1}$ is found to be⁷

$$\mathbf{u}_{\sigma\perp 1} = \frac{m_\sigma}{B q_\sigma} \mathbf{b} \times \frac{d}{dt} \mathbf{u}_{\sigma\perp 0} + \frac{\mathbf{b} \times \nabla_\perp \Pi_\sigma}{B n_\sigma q_\sigma} + \frac{\nu_{\sigma\alpha} m_\sigma}{B q_\sigma} \mathbf{b} \times (\mathbf{u}_{\sigma\perp 0} - \mathbf{u}_{\alpha\perp 0}) \quad (2.47)$$

The first term of Eq. (2.47) has already been evaluated in section 2.1.3 and is given by

$$\mathbf{u}_{p\sigma} = \frac{m_\sigma T_\sigma}{q_\sigma B^2} \frac{d}{dt} \nabla_\perp \left(\frac{-q_\sigma \phi}{T_\sigma} - \ln n_\sigma \right), \quad (2.48)$$

and the last term is easily evaluated and gives

$$\begin{aligned} \mathbf{u}_{R\sigma} &= \frac{\nu_{\sigma\alpha} m_\sigma}{B q_\sigma} \mathbf{b} \times \left(-\frac{\nabla_\perp \phi \times \mathbf{b}}{B} - \frac{T_\sigma}{q_\sigma B} \nabla_\perp \ln n_\sigma \times \mathbf{b} + \frac{\nabla_\perp \phi \times \mathbf{b}}{B} + \frac{T_\alpha}{q_\alpha B} \nabla_\perp \ln n_\alpha \times \mathbf{b} \right) \\ &= \frac{\nu_{\sigma\alpha} m_\sigma}{B q_\sigma} \mathbf{b} \times \left(\frac{T_\sigma}{q_\sigma B} \mathbf{b} \times \nabla_\perp \ln n_\sigma - \frac{T_\alpha}{q_\alpha B} \mathbf{b} \times \nabla_\perp \ln n_\alpha \right) \\ &= \frac{\nu_{\sigma\alpha} m_\sigma}{B q_\sigma} \left(-\frac{T_\sigma}{q_\sigma B} \nabla_\perp \ln n_\sigma + \frac{T_\alpha}{q_\alpha B} \nabla_\perp \ln n_\alpha \right). \end{aligned} \quad (2.49)$$

⁷See appendix A.1.5 for the derivation.

The final term is found to be⁸

$$\mathbf{u}_{\Pi\sigma} = \frac{\mathbf{b} \times \nabla_{\perp} \boldsymbol{\Pi}_{\sigma}}{B n_{\sigma} q_{\sigma}} = -\frac{\eta_1^{\sigma}}{B^2 n_{\sigma} q_{\sigma}} \nabla_{\perp} \cdot \nabla_{\perp}^2 \phi. \quad (2.50)$$

Using that[10] $\eta_1^{\sigma} = \frac{3}{10} n \frac{T_i \nu_{ci}}{\omega_{ce}^2}$, it is seen that $\eta_1^e \ll \eta_1^i$, since $\omega_{ci} \ll \omega_{ce}$. Finally assuming that the ions are cold and stationary in the parallel direction, the electron and ion fluid velocities can be written as

$$\mathbf{u}_e = \mathbf{u}_E + \mathbf{u}_{de} - \frac{\nu_{ei} m_e}{B^2 e} \left(\frac{T_e}{e} \nabla_{\perp} \ln n_e \right) + \frac{T_e}{m_e \nu_{ei}} \nabla_{\parallel} \left(\frac{e \phi}{T_e} - \ln n_e \right) \quad (2.51)$$

$$\begin{aligned} \mathbf{u}_i &= \mathbf{u}_E + \mathbf{u}_{pi} + \frac{\nu_{ie} m_i}{B^2 e} \left(-\frac{T_e}{e} \nabla_{\perp} \ln n_i \right) - \frac{\eta_1^i}{B^2 n_i e} \nabla_{\perp} \cdot \nabla_{\perp}^2 \phi \\ &= \mathbf{u}_E + \mathbf{u}_{pi} + \frac{n_i \nu_{ie} m_i}{n_i B^2 e} \left(-\frac{T_e}{e} \nabla_{\perp} \ln n_i \right) - \frac{\eta_1^i}{B^2 n_i e} \nabla_{\perp} \cdot \nabla_{\perp}^2 \phi \\ &= \mathbf{u}_E + \mathbf{u}_{pi} + \frac{\nu_{ei} m_e n_e}{n_i B^2 e} \left(-\frac{T_e}{e} \nabla_{\perp} \ln n_i \right) - \frac{\eta_1^i}{B^2 n_i e} \nabla_{\perp} \cdot \nabla_{\perp}^2 \phi, \end{aligned} \quad (2.52)$$

where, in the last line, it has been used that a plasma cannot exert a drag on itself, so $\nu_{ei} n_e m_e = \nu_{ie} n_i m_i$.

Inserting Eq. (2.51) and (2.52) into the continuity equation, Eq. (2.11), and using that the contributions from \mathbf{u}_E , \mathbf{u}_p and \mathbf{u}_d are the same as for the weakly ionized plasma, the electron continuity equation is given as

$$\begin{aligned} \frac{d}{dt} \ln n_e + (\nabla \ln n_e + \nabla) \cdot \left(-\frac{\nu_{ei} T_e}{\omega_{ce} e B} \nabla_{\perp} \ln n_e + \frac{T_e \omega_{ce}}{\nu_{ei} e B} \nabla_{\parallel} (\varphi - \ln n_e) \right) \\ - \frac{2 T_e}{e B R} \hat{\mathbf{z}} \cdot \nabla_{\perp} (\varphi - \ln n_e) = 0, \end{aligned} \quad (2.53)$$

and the ion continuity equation is given as

$$\begin{aligned} \frac{d}{dt} \ln n_i - (\nabla \ln n_i + \nabla) \cdot \left(\frac{T_e}{e \omega_{ci} B} \frac{d}{dt} \nabla_{\perp} \varphi - \frac{\nu_{ei} T_e n_e}{\omega_{ce} e B n_i} \nabla_{\perp} \ln n_i + \frac{\eta_1^i}{B^2 n_i e} \nabla_{\perp} \cdot \nabla_{\perp}^2 \phi \right) \\ - \frac{2 T_e}{e B R} \hat{\mathbf{z}} \cdot \nabla_{\perp} \varphi = 0. \end{aligned} \quad (2.54)$$

Assuming quasi-neutrality and inserting the definition of η_1^i , the electron continuity equations is given by

$$\begin{aligned} \frac{d}{dt} \ln n + (\nabla \ln n + \nabla) \cdot \left(-\frac{\nu_{ei} T_e}{\omega_{ce} e B} \nabla_{\perp} \ln n + \frac{T_e \omega_{ce}}{\nu_{ei} e B} \nabla_{\parallel} (\varphi - \ln n) \right) \\ - \frac{2 T_e}{e B R} \hat{\mathbf{z}} \cdot \nabla_{\perp} (\varphi - \ln n) = 0, \end{aligned} \quad (2.55)$$

and the charge continuity equation is given by

$$\begin{aligned} (\nabla \ln n + \nabla) \cdot \left(\frac{T_e \omega_{ce}}{\nu_{ei} e B} \nabla_{\parallel} (\varphi - \ln n) + \frac{T_e}{\omega_{ci} e B} \frac{d}{dt} \nabla_{\perp} \varphi \right. \\ \left. - \frac{3 T_i T_e \nu_i}{10 \omega_{ci}^2 e^2 B^2} \nabla_{\perp} \cdot \nabla_{\perp}^2 \varphi \right) + \frac{2 T_e}{e B R} \hat{\mathbf{z}} \cdot \nabla_{\perp} \ln n = 0, \end{aligned} \quad (2.56)$$

where ν_i is the ion-ion collision frequency.

⁸See appendix A.1.6 for the derivation.

Local approximation

Again, as in section 2.1.3, a local approximation is made, which means that Eq. (2.55) simplifies to

$$\frac{d}{dt} \ln n - \frac{\nu_{ei} T_e}{\omega_{ce} e B} \nabla_{\perp}^2 \ln n + \frac{T_e \omega_{ce}}{\nu_{ei} e B} \nabla_{\parallel}^2 (\varphi - \ln n) - \frac{2T_e}{eBR} \hat{\mathbf{z}} \cdot \nabla_{\perp} (\varphi - \ln n) = 0 \quad (2.57)$$

and Eq. (2.56) simplifies to

$$\frac{T_e \omega_{ce}}{\nu_{ei} e B} \nabla_{\parallel}^2 (\varphi - \ln n) + \frac{T_e}{\omega_{ci} e B} \frac{d}{dt} \nabla_{\perp}^2 \varphi - \frac{3T_i T_e \nu_{ii}}{10 \omega_{ci}^2 e^2 B^2} \nabla_{\perp}^2 \cdot \nabla_{\perp}^2 \varphi + \frac{2T_e}{eBR} \hat{\mathbf{z}} \cdot \nabla_{\perp} \ln n = 0. \quad (2.58)$$

Defining $\nu_e \equiv \nu_{ei}/\omega_{ce}$ and $\nu_i \equiv 3T_i \nu_{ii}/10T_e \omega_{ci}$ and using Bohm normalization, the dimensionless equations for a fully ionized, magnetically confined plasma under a local approximation, are given by

$$\frac{\partial}{\partial t} \ln n + \{\varphi, \ln n\} + \xi \frac{\partial}{\partial y} (\ln n - \varphi) = \nu_e \nabla_{\perp}^2 \ln n + \nu_e^{-1} \nabla_{\parallel}^2 (\ln n - \varphi) \quad (2.59)$$

$$\frac{\partial}{\partial t} \Omega + \{\varphi, \Omega\} + \xi \frac{\partial}{\partial y} \ln n = \nu_e^{-1} \nabla_{\parallel}^2 (\ln n - \varphi) + \nu_i \nabla_{\perp}^2 \Omega, \quad (2.60)$$

which is verified by [9]. Finally assuming an exponential density profile, given in Eq. (2.40), Eq. (2.59) and (2.60) simplify to

$$\frac{\partial}{\partial t} n + \{\varphi, n\} + (\kappa - \xi) \frac{\partial}{\partial y} \varphi + \xi \frac{\partial}{\partial y} n = \nu_e \nabla_{\perp}^2 n + \nu_e^{-1} \nabla_{\parallel}^2 (n - \varphi) \quad (2.61)$$

$$\frac{\partial}{\partial t} \Omega + \{\varphi, \Omega\} + \xi \frac{\partial}{\partial y} n = \nu_e^{-1} \nabla_{\parallel}^2 (n - \varphi) + \nu_i \nabla_{\perp}^2 \Omega. \quad (2.62)$$

Upon comparing these with Eq. (2.41) and (2.42), it is seen that the governing equations for weakly and fully ionized plasmas are very similar, and only differ in the definitions of the collision coefficients and perpendicular collision terms.

2.2 Instabilities

The model equations developed in the previous section are greatly simplified, however they do give a qualitative description of some of the properties of a plasma, which include different kinds of instabilities.

To get a qualitative description of these instabilities, nonlinear terms, i.e. the terms in the poisson-brackets and the perpendicular damping terms are neglected. With these simplifications, Eq. (2.61) and Eq. (2.62) have the same form as Eq. (2.41) and Eq. (2.42), so the following derivations are the same for both weakly and fully ionized plasmas. Assuming that the fluctuating density and potential have plane-wave solutions of the form[9]

$$n = n_{\mathbf{k}} \exp(i\mathbf{k} \cdot \mathbf{x} - i\omega t) \quad (2.63)$$

$$\varphi = \varphi_{\mathbf{k}} \exp(i\mathbf{k} \cdot \mathbf{x} - i\omega t), \quad (2.64)$$

Eq. (2.41) leads to

$$\begin{aligned} & -i\omega n_{\mathbf{k}} - \nu_e^{-1} k_{\parallel}^2 (\varphi_{\mathbf{k}} - n_{\mathbf{k}}) + i(\kappa - \xi) k_y \varphi_{\mathbf{k}} + i\xi k_y n_{\mathbf{k}} = 0 \\ \Rightarrow & n_{\mathbf{k}} \left(i\xi k_y + \nu_e^{-1} k_{\parallel}^2 - i\omega \right) - \varphi_{\mathbf{k}} \left(\nu_e^{-1} k_{\parallel}^2 - i(\kappa - \xi) k_y \right) = 0 \\ \Rightarrow & \frac{\nu_e^{-1} k_{\parallel}^2 - i\kappa k_y + i\xi k_y}{i\xi k_y + \nu_e^{-1} k_{\parallel}^2 - i\omega} \varphi_{\mathbf{k}} = n_{\mathbf{k}} \end{aligned} \quad (2.65)$$

Remembering the definition of Ω , Eq. (2.42) gives

$$\begin{aligned} i\omega k_{\perp}^2 \varphi_{\mathbf{k}} - \nu_e^{-1} k_{\parallel}^2 \varphi_{\mathbf{k}} + \nu_e^{-1} k_{\parallel}^2 n_{\mathbf{k}} + i\xi k_y n_{\mathbf{k}} &= 0 \\ \Rightarrow i\omega k_{\perp}^2 \varphi_{\mathbf{k}} - \nu_e^{-1} k_{\parallel}^2 \varphi_{\mathbf{k}} + \nu_e^{-1} k_{\parallel}^2 \frac{\nu_e^{-1} k_{\parallel}^2 - i\kappa k_y + i\xi k_y}{i\xi k_y + \nu_e^{-1} k_{\parallel}^2 - i\omega} \varphi_{\mathbf{k}} \\ + i\xi k_y \frac{\nu_e^{-1} k_{\parallel}^2 - i\kappa k_y + i\xi k_y}{i\xi k_y + \nu_e^{-1} k_{\parallel}^2 - i\omega} \varphi_{\mathbf{k}} &= 0. \end{aligned} \quad (2.66)$$

Collecting terms of ω leads to

$$\begin{aligned} \omega^2 + \omega \left(-\xi k_y + i\nu_e^{-1} k_{\parallel}^2 + i\nu_e^{-1} \frac{k_{\parallel}^2}{k_{\perp}^2} \right) \\ + \frac{1}{k_{\perp}^2} \left(-i\nu_e^{-1} \kappa k_y + i\nu_e^{-1} \xi k_{\parallel}^2 k_y - i\xi \kappa k_y^2 + \xi^2 k_y^2 \right) = 0 \end{aligned} \quad (2.67)$$

Following the notation of [9], several different parameters are defined in order to simplify future calculations;

$$\omega_{fm} = \xi k_y, \quad \omega_{dw} = \frac{\kappa k_y}{1 + k_{\perp}^2} \quad (2.68)$$

$$\Phi = \frac{\xi k_{\perp}^2}{\kappa - \xi}, \quad \Psi = \nu_e^{-1} k_{\parallel}^2 \frac{(1 + k_{\perp}^2)^2}{\kappa k_y k_{\perp}^2}. \quad (2.69)$$

Using these definitions, a dispersion relation, relating the wavenumber and the frequency of the plane-waves is found to be⁹

$$\omega^2 + (i\Psi \omega_{dw} - \omega_{fm}) \omega - i\Psi \omega_{dw}^2 + \frac{\omega_{fm}^2}{\Phi} + i\omega_{fm} \omega_{dw} \frac{\Psi}{1 + k_{\perp}^2} = 0. \quad (2.70)$$

From Eq. (2.63) and Eq. (2.64), it is seen that an exponential growth of the plane-waves occurs if ω has a positive imaginary part, which is what gives rise to the instabilities examined here.

2.2.1 Interchange instability

The first instability examined is the so-called interchange instability, which is caused by a curvature in the magnetic field[9]. Neglecting either collisions or parallel dynamics¹⁰, so $\Psi = 0$, the dispersion relation, Eq. (2.70), reduces to

$$\omega^2 - \omega_{fm} \omega + \omega_{fm}^2 \frac{1}{\Phi} = 0, \quad (2.71)$$

which has the solution

$$\begin{aligned} \omega &= \frac{\omega_{fm} \pm \sqrt{\omega_{fm}^2 - 4\omega_{fm}^2 \frac{1}{\Phi}}}{2} \\ \Rightarrow \frac{\omega}{\omega_{fm}} &= \frac{1}{2} \pm \sqrt{\frac{\Phi - 4}{4\Phi}}. \end{aligned} \quad (2.72)$$

An instability can only occur if ω is complex, which is true if $0 < \Phi < 4$. Furthermore, only a positive imaginary part will cause exponential growth, so an instability can only

⁹See the derivation in appendix A.1.7.

¹⁰Essentially assuming a solely 2D system.

occur for the positive solution. It is also seen from the definition of Φ , Eq. (2.69), that no instabilities can occur for $\xi > \kappa$.

For $0 < \Phi < 4$ it is seen, from Eq. (2.72), that the real frequency ω_r and the growth rate ω_i are given by

$$\begin{aligned}\omega_r &= \Re(\omega) = \frac{\omega_{fm}}{2} = \frac{k_y \xi}{2} = \frac{\rho_s}{R_0} k_y & (2.73) \\ \omega_i &= \Im(\omega) = \omega_{fm} \left(\frac{4 - \Phi}{4\Phi} \right)^{1/2} = k_y \xi \left(\frac{4\kappa - 4\xi - \xi k_\perp^2}{4\xi k_\perp^2} \right)^{1/2} \\ &= \left(\frac{8\rho_s^2}{4LR_0} - \frac{16\rho_s^2}{4R_0^2} - \frac{4\rho_s^2 k_\perp^2}{R_0^2} \right)^{1/2} \frac{k_y}{k_\perp} \\ &= \left(\frac{2\rho_s^2}{LR_0} \right)^{1/2} \left(1 - \frac{2L}{R_0} - \frac{k_\perp^2}{2R_0} \right)^{1/2} \frac{k_y}{k_\perp}. & (2.74)\end{aligned}$$

These are plotted in Figure 2.2, and it is seen that the largest growth rate is at $\Phi \rightarrow 0$, where the imaginary part diverges.

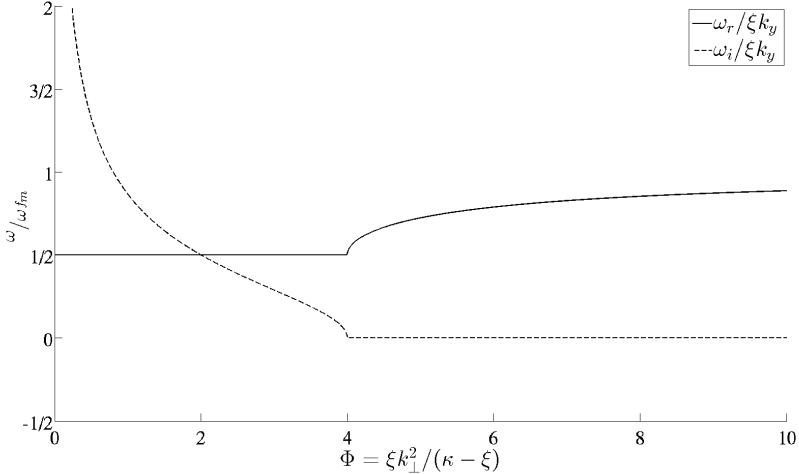


Figure 2.2: Dispersion diagram for the real frequency and the growth-rate of fluctuating perturbations in a toroidal magnetic field.

Now using Eq. (2.65), neglecting collisions, and using the positive solution of Eq. (2.72), the ratio between $n_{\mathbf{k}}$ and $\phi_{\mathbf{k}}$ is found to be

$$\frac{n_{\mathbf{k}}}{\phi_{\mathbf{k}}} = -k_\perp^2 \left[\frac{1}{2} + \left(\frac{\Phi - 4}{4\Phi} \right)^{1/2} \right] = -k_\perp^2 \left[\frac{1}{2} + i \left(\frac{4 - \Phi}{4\Phi} \right)^{1/2} \right], \quad (2.75)$$

for $0 < \Phi < 4$, from which it is possible to extract the phase and the amplitude ratio of the fluctuations. The phase of a complex number $z = a + ib$ is given by $\tan(\theta + \pi) = b/a$ when both a and b are less than zero, and the amplitude is given by $r = |z| = \sqrt{a^2 + b^2}$, which means that

$$\tan(\theta_{\mathbf{k}} + \pi) = \frac{-k_\perp^2 ((4 - \Phi)/4\Phi)^{1/2}}{-k_\perp^2 (1/2)} = \left(\frac{4 - \Phi}{\Phi} \right)^{1/2}, \quad (2.76)$$

and

$$r = \left| \frac{n_{\mathbf{k}}}{\phi_{\mathbf{k}}} \right| = \sqrt{\left(\frac{-k_\perp^2}{2} \right)^2 + (-k_\perp^2) \left(\frac{4 - \Phi}{4\Phi} \right)^{1/2}} = k_\perp \sqrt{\frac{\kappa - \xi}{\xi}}. \quad (2.77)$$

A plot of the phase-difference $|\theta_{\mathbf{k}}|$ is seen in Figure 2.3, and comparing it with Figure 2.2, it is seen that the instability occurs for $\pi/2 < \theta_{\mathbf{k}} < \pi$, and that it is greatest for a phase-difference of $\pi/2$.

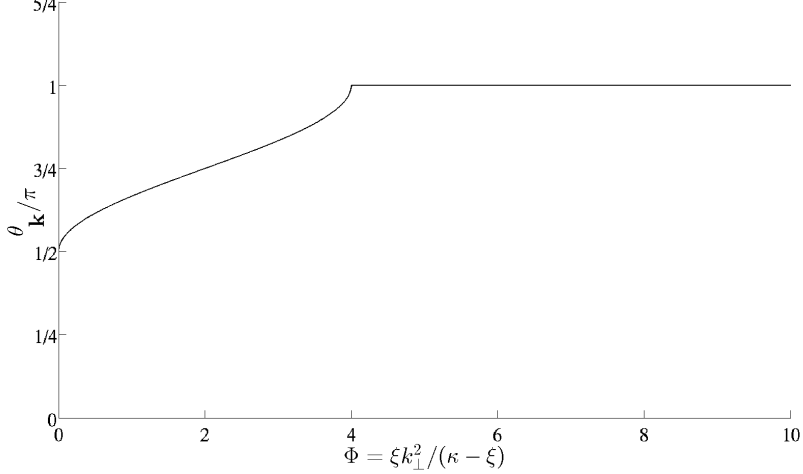


Figure 2.3: A plot of the phase-difference between the density fluctuations and the potential fluctuations for a collisionless plasma.

The nonlinear particle flux due to fluctuations is given by $\Gamma = n u_x$ in dimensionless units, where n is the fluctuating plasma density and u_x is the fluctuating fluid velocity in the radial (x -direction)[9]. The main velocity is the $\mathbf{E} \times \mathbf{B}$ drift, since the fluctuations in question are assumed to be electrostatic, low-frequency fluctuations. This means that

$$\Gamma = -n \frac{\partial}{\partial y} \phi. \quad (2.78)$$

The non-dimensional volume-averaged radial plasma flux due to fluctuations is then given by[9],

$$\Gamma_0 \equiv \int \Gamma dx dy = - \int n \frac{\partial \phi}{\partial y} dx dy. \quad (2.79)$$

Expanding both n and ϕ in Fourier modes, $n = \sum_{\mathbf{k}} n_{\mathbf{k}} \exp(i\mathbf{k} \cdot \mathbf{r})$ and $\phi = \sum_{\mathbf{k}'} \phi_{\mathbf{k}'} \exp(i\mathbf{k}' \cdot \mathbf{r})$, Γ_0 becomes

$$\Gamma_0 = - \int \sum_{\mathbf{k}\mathbf{k}'} ik'_y n_{\mathbf{k}} \phi_{\mathbf{k}'} \exp(i(\mathbf{k} + \mathbf{k}') \cdot \mathbf{r}) dx dy. \quad (2.80)$$

Using the definition of a 2D delta function $(2\pi)^2 \delta(\mathbf{k} + \mathbf{k}') = \int \exp(i(\mathbf{k} + \mathbf{k}') \cdot \mathbf{r}) \cdot d\mathbf{r}$, the radial plasma-flux is given by

$$\Gamma_0 = (2\pi)^2 \sum_{\mathbf{k}} ik_y n_{\mathbf{k}} \phi_{-\mathbf{k}}. \quad (2.81)$$

Now since both n and ϕ are real functions, the Fourier components have the properties

$n_{-\mathbf{k}} = n_{\mathbf{k}}^*$ and $\phi_{-\mathbf{k}} = \phi_{\mathbf{k}}^*$. Dividing by $(2\pi)^2$ on both sides and redefining Γ_0 , gives

$$\begin{aligned}\Gamma_0 &= \sum_{\mathbf{k} \geq 0} ik_y n_{\mathbf{k}} \phi_{\mathbf{k}}^* + \sum_{\mathbf{k} \leq 0} ik_y n_{\mathbf{k}} \phi_{\mathbf{k}}^* \\ &= \sum_{\mathbf{k} \geq 0} ik_y n_{\mathbf{k}} \phi_{\mathbf{k}}^* - \sum_{\mathbf{k} \geq 0} ik_y n_{\mathbf{k}}^* \phi_{\mathbf{k}} \\ &= \sum_{\mathbf{k} \geq 0} ik_y (n_{\mathbf{k}} \phi_{\mathbf{k}}^* - n_{\mathbf{k}}^* \phi_{\mathbf{k}}) \\ &= - \sum_{\mathbf{k} \geq 0} 2k_y \Im(n_{\mathbf{k}} \phi_{\mathbf{k}}^*). \end{aligned} \quad (2.82)$$

Using the phase-relation

$$\frac{\phi_{\mathbf{k}}}{n_{\mathbf{k}}} = \left| \frac{\phi_{\mathbf{k}}}{n_{\mathbf{k}}} \right| \exp(i\theta_{\mathbf{k}}) \quad (2.83)$$

in Eq. (2.82), Γ_0 becomes

$$\begin{aligned}\Gamma_0 &= - \sum_{\mathbf{k} \geq 0} 2k_y \Im \left(n_{\mathbf{k}} n_{\mathbf{k}}^* \left| \frac{\phi_{\mathbf{k}}}{n_{\mathbf{k}}} \right| \exp(-i\theta_{\mathbf{k}}) \right) \\ &= \sum_{\mathbf{k} \geq 0} 2k_y |\phi_{\mathbf{k}}| |n_{\mathbf{k}}| \sin(\theta_{\mathbf{k}}). \end{aligned} \quad (2.84)$$

Finally using Eq. (2.77), gives

$$\Gamma_0 = \sum_{\mathbf{k} \geq 0} 2k_y k_{\perp} \left(\frac{\kappa - \xi}{\xi} \right)^{1/2} |\phi_{\mathbf{k}}|^2 \sin(\theta_{\mathbf{k}}), \quad (2.85)$$

which shows that a relative phase between the density and the potential fluctuations is essential for nonlinear transport. Even for large values of $|\phi_{\mathbf{k}}|$, radial transport is not guaranteed, e.g. if $\theta_{\mathbf{k}} = 0$, which means that $\Gamma_0 = 0$ and no radial plasma flux is present.

2.2.2 Resistive drift waves

Another source of nonlinear transport for magnetically confined plasmas are the so-called drift waves, which originate from parallel collisions. In a uniform magnetic field, $\omega_{fm} = 0$ [9], and the dispersion relation, Eq. (2.70), becomes

$$\omega^2 + i\Psi\omega_{dw}\omega - i\Psi\omega_{dw}^2 = 0, \quad (2.86)$$

which has the solution

$$\begin{aligned}\omega &= \frac{-i\Psi\omega_{dw} \pm \sqrt{-\Psi^2\omega_{dw}^2 + i4\Psi\omega_{dw}^2}}{2} \\ \Rightarrow \frac{\omega}{\omega_{dw}} &= \frac{i\Psi}{2} \left(-1 \pm \left(1 - \frac{i4}{\Psi} \right)^{1/2} \right). \end{aligned} \quad (2.87)$$

Again no instability occurs for the negative solution. Denoting ω as

$$\frac{\omega}{\omega_{dw}} = \frac{\omega_r}{\omega_{dw}} + i \frac{\omega_i}{\omega_{dw}} \quad (2.88)$$

and plotting the real and imaginary parts in Figure 2.4, it is seen that the maximum growth-rate occurs around $\Psi \approx 1$.

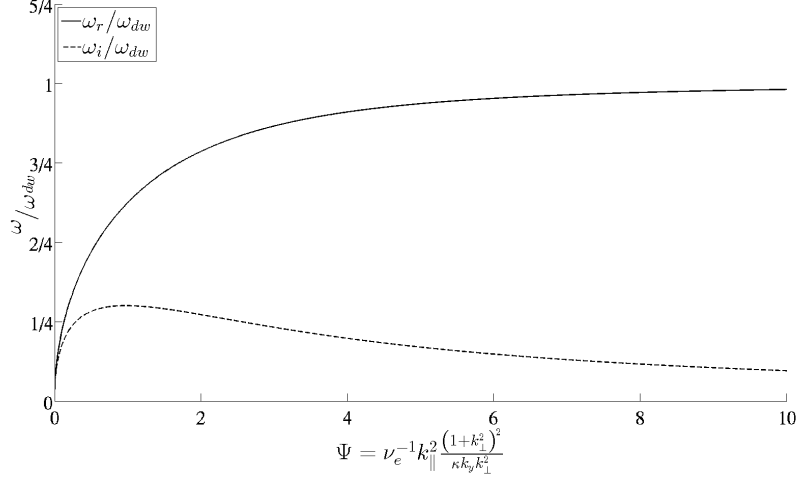


Figure 2.4: Dispersion diagram for the real frequency and the growth-rate of fluctuating perturbations in uniform magnetic field with parallel losses.

In the same way as for the interchange instability, the ratio between $n_{\mathbf{k}}$ and $\phi_{\mathbf{k}}$ is calculated in order to determine the phase-relation and the amplitude. Using Eq. (2.66) neglecting curvature effects, so $\omega_{fm} = 0$, the ratio becomes

$$\begin{aligned} \frac{n_{\mathbf{k}}}{\phi_{\mathbf{k}}} &= \frac{\nu_e^{-1} k_{||}^2 - i\omega k_{\perp}^2}{\nu_e^{-1} k_{||}^2} = 1 - i \frac{k_{\perp}^2}{\nu_e^{-1} k_{||}^2} (\omega_r + i\omega_r) = 1 + \frac{k_{\perp}^2}{\nu_e^{-1} k_{||}^2} (\omega_i - i\omega_r) \\ &= 1 + \frac{\kappa k_y (1 + k_{\perp}^2)^2}{\Psi} (\omega_i - i\omega_r) = 1 + \frac{1 + k_{\perp}^2}{\Psi} \left(\frac{\omega_i}{\omega_{dw}} - i \frac{\omega_r}{\omega_{dw}} \right), \end{aligned} \quad (2.89)$$

and phase-difference is then given by

$$\tan(\theta_{\mathbf{k}}) = -\frac{\omega_r/\omega_{dw}}{1 + (1 + k_{\perp}^2/\Psi) \omega_i/\omega_{dw}}. \quad (2.90)$$

A plot of the phase-difference, $|\theta_{\mathbf{k}}|$, for the drift-waves with $k_{\perp} \ll 1$ is seen in Figure 2.5. From the figure it is seen that the phase-difference approaches $|\theta| \rightarrow 1/4\pi$ as $\Psi \rightarrow 0$ and approaches 0 as $\Psi \rightarrow \infty$.

From this, it is seen that the drift-waves and interchange instabilities cause exponential growth for different relative phases between the density and potential fluctuations. It is therefore interesting to examine the effects of magnetic field curvature and parallel collisions combined.

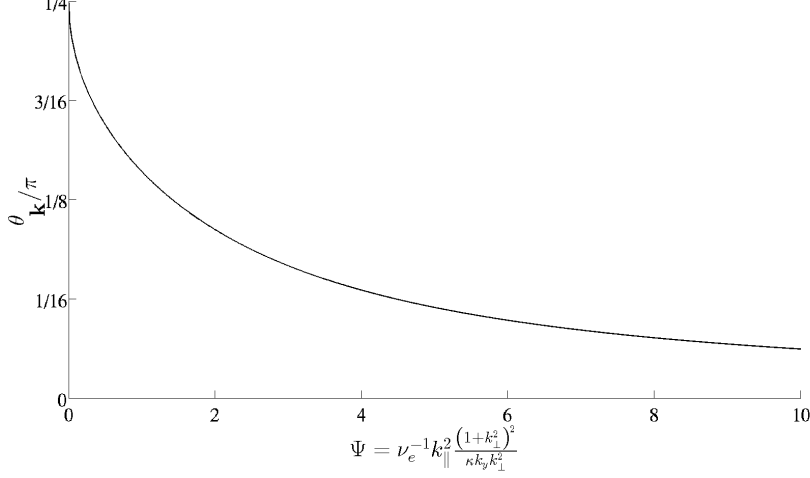


Figure 2.5: A plot of the phase-difference between the density fluctuations and the potential fluctuations in the absence of magnetic field curvature and with $k_{\perp} \ll 1$.

2.2.3 Effect of drift waves

The complete solution to Eq. (2.70) is given by

$$\begin{aligned} \omega &= \frac{\omega_{fm} - i\Psi\omega_{dw} \pm \sqrt{(i\Psi\omega_{dw} - \omega_{fm})^2 - 4 \left(\frac{\omega_{fm}^2}{\Phi} + i\omega_{fm}\omega_{dw} \frac{\Psi}{1+k_{\perp}^2} - i\Psi\omega_{dw}^2 \right)}}{2} \\ \Rightarrow 2\frac{\omega}{\omega_{dw}} &= \frac{\omega_{fm}}{\omega_{dw}} - i\Psi \pm \sqrt{-\Psi^2 + \frac{\omega_{fm}^2}{\omega_{dw}^2} - 2i\Psi \frac{\omega_{fm}}{\omega_{dw}} - 4\frac{\omega_{fm}^2}{\omega_{dw}^2\Phi} - 4i\frac{\omega_{fm}\Psi}{\omega_{dw}(1+k_{\perp}^2)} + 4i\Psi} \\ &= \frac{\omega_{fm}}{\omega_{dw}} - i\Psi \pm \sqrt{i4\Psi - \Psi^2 - \frac{4-\Phi}{\Phi} \frac{\omega_{fm}^2}{\omega_{dw}^2} - 2i\Psi \frac{\omega_{fm}}{\omega_{dw}} - 4i\frac{\Psi\omega_{fm}}{\omega_{dw}(1+k_{\perp}^2)}}. \quad (2.91) \end{aligned}$$

from which Eq. (2.72) is obtained for $\Psi = 0$ and Eq. (2.87) is obtained for $\omega_{fm} = 0$, just as required.

For small Φ , the third term in the square root dominates, and the dispersion equation in this limit for the unstable branch reads

$$\begin{aligned} 2\frac{\omega}{\omega_{dw}} &= \frac{\omega_{fm}}{\omega_{dw}} - i\Psi + i\sqrt{\frac{4-\Phi}{\Phi}} \frac{\omega_{fm}}{\omega_{dw}} \left(1 + \Psi^2 \frac{\Phi}{4-\Phi} \frac{\omega_{dw}^2}{\omega_{fm}^2} - i4\Psi \frac{\Phi}{4-\Phi} \frac{\omega_{dw}^2}{\omega_{fm}^2} + 2i\Psi \frac{\omega_{dw}}{\omega_{fm}} \frac{\Phi}{4-\Phi} \right. \\ &\quad \left. + 4i\frac{\Psi\omega_{dw}}{\omega_{fm}(1+k_{\perp}^2)} \frac{\Phi}{4-\Phi} \right)^{1/2} \\ &\approx \frac{\omega_{fm}}{\omega_{dw}} - i\Psi + i \left(\frac{4-\Phi}{\Phi} \right)^{1/2} \frac{\omega_{fm}}{\omega_{dw}} + i\frac{\Psi^2}{2} \left(\frac{\Phi}{4-\Phi} \right)^{1/2} \frac{\omega_{dw}}{\omega_{fm}} - 2i\Psi \left(\frac{\Phi}{4-\Phi} \right)^{1/2} \frac{\omega_{dw}}{\omega_{fm}} \\ &\quad + i\Psi \left(\frac{\Phi}{4-\Phi} \right)^{1/2} + 2i\Psi \frac{1}{1+k_{\perp}^2} \left(\frac{\Phi}{4-\Phi} \right)^{1/2} \end{aligned}$$

which shows that the drift modes with finite but small Ψ have a stabilising effect on the interchange instability.

For very large Ψ , the second term becomes dominant, and the unstable branch reads

$$\begin{aligned} 2\frac{\omega}{\omega_{dw}} &= \frac{\omega_{fm}}{\omega_{dw}} - i\Psi + i\Psi \left(1 - \frac{i4}{\Psi} + \frac{4 - \Phi}{\Phi\Psi^2} \frac{\omega_{fm}^2}{\omega_{dw}^2} + \frac{2i}{\Psi} \frac{\omega_{fm}}{\omega_{dw}} + \frac{4i}{\Psi} \frac{\omega_{fm}}{\omega_{dw}(1 + k_\perp^2)} \right)^{1/2} \\ &\approx \frac{\omega_{fm}}{\omega_{dw}} - i\Psi + i\Psi + 2 + i \frac{4 - \Phi}{2\Phi\Psi} \frac{\omega_{fm}^2}{\omega_{dw}^2} - \frac{\omega_{fm}}{\omega_{dw}} - 2 \frac{\omega_{fm}}{\omega_{dw}(1 + k_\perp^2)} \\ &\Rightarrow \omega \approx \omega_{dw} + i \frac{4 - \Phi}{4\Phi\Psi} \frac{\omega_{fm}^2}{\omega_{dw}} - \frac{\omega_{fm}}{(1 + k_\perp^2)}, \end{aligned}$$

so the imaginary frequency is given by

$$\begin{aligned} \omega_i &= \frac{4 - \Phi}{4\Phi\Psi} \frac{\omega_{fm}^2}{\omega_{dw}} = \frac{(4(\kappa - \xi) - \xi k_\perp^2)\kappa k_y k_\perp^2}{4\xi k_\perp^2 \nu_e^{-1} k_\parallel^2 (1 + k_\perp^2)^2} \frac{\xi^2 k_y^2 (1 + k_\perp^2)}{\kappa k_y} \\ &= \frac{4(\rho_s R_0/L - 2\rho_s) - 2\rho_s k_\perp^2}{4R_0^2 \nu_e^{-1} k_\parallel^2 (1 + k_\perp^2)} 2\rho_s k_y^2 \end{aligned} \quad (2.92)$$

$$= \frac{2\rho_s^2}{R_0 L} \left(1 - \frac{2L}{R_0} - \frac{k_\perp^2 L}{2R_0} \right) \frac{k_y^2}{\nu_e^{-1} k_\parallel^2 (1 + k_\perp^2)}, \quad (2.93)$$

where a again stabilising effect is seen, upon comparing with Eq. (2.74). This stabilising effect is also seen in Figure 2.6, which is a contour plot of the imaginary frequency in Eq. (2.91), where $k_\perp \ll 1$ is assumed, and where it has been used that

$$\frac{\omega_{fm}}{\omega_{dw}} = \frac{\xi k_y}{\kappa k_y} = \frac{2\rho_s}{R_0} \frac{L}{\rho_s} = \frac{2L}{R_0} \equiv 2c, \quad (2.94)$$

with L being the minor radius of the device and R_0 being the major radius. In Figure 2.6 a ratio between the minor and major radius of $c = 0.3$ is used. From the plot it is seen that the maximum value is at $\Phi \rightarrow 0$, just as seen in section 2.2.1. Furthermore, it is also seen that Ψ has a stabilizing effect, just as described in the above analysis.

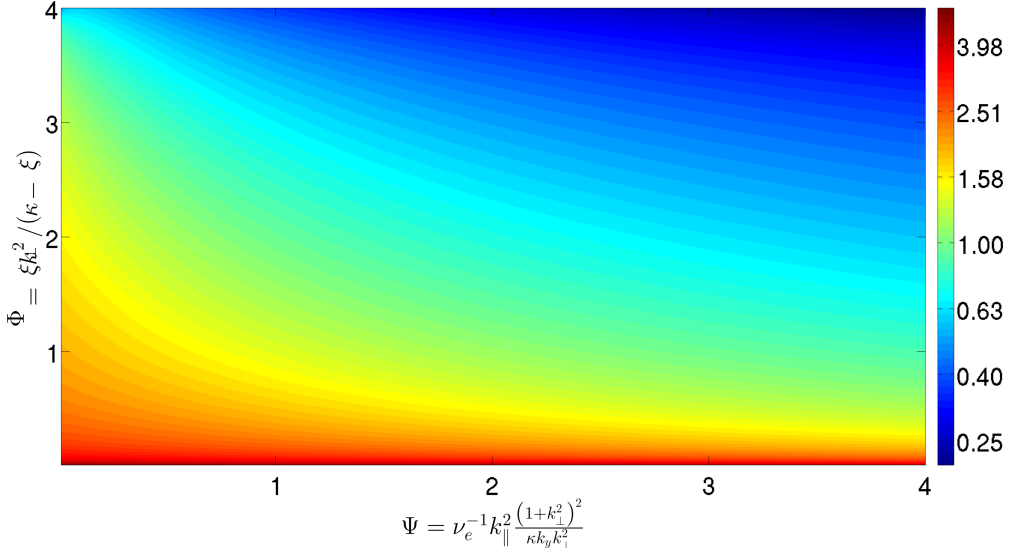


Figure 2.6: A contour plot of the imaginary frequency of the full solution to the dispersion relation Eq. (2.70). The colorbar shows ω_i/ω_{dw} . Note that the colourbar increases logarithmically.

To further investigate the stabilizing effects of Ψ , three plots of the cross section of Figure 2.6 are made at different values of Φ , and are seen in Figure 2.7. From all three plots, it is evident that the growth-rate decreases with increasing Ψ . Furthermore, it is seen, upon comparing Figure 2.7a with Figures 2.7b and 2.7c, that the growth rate decreases faster relative to the initial value as Φ is increased. Figure 2.7c also shows that that, for large values of Φ , small values Ψ can have a destabilising effect, but as Ψ increases, the growth rate again decreases.

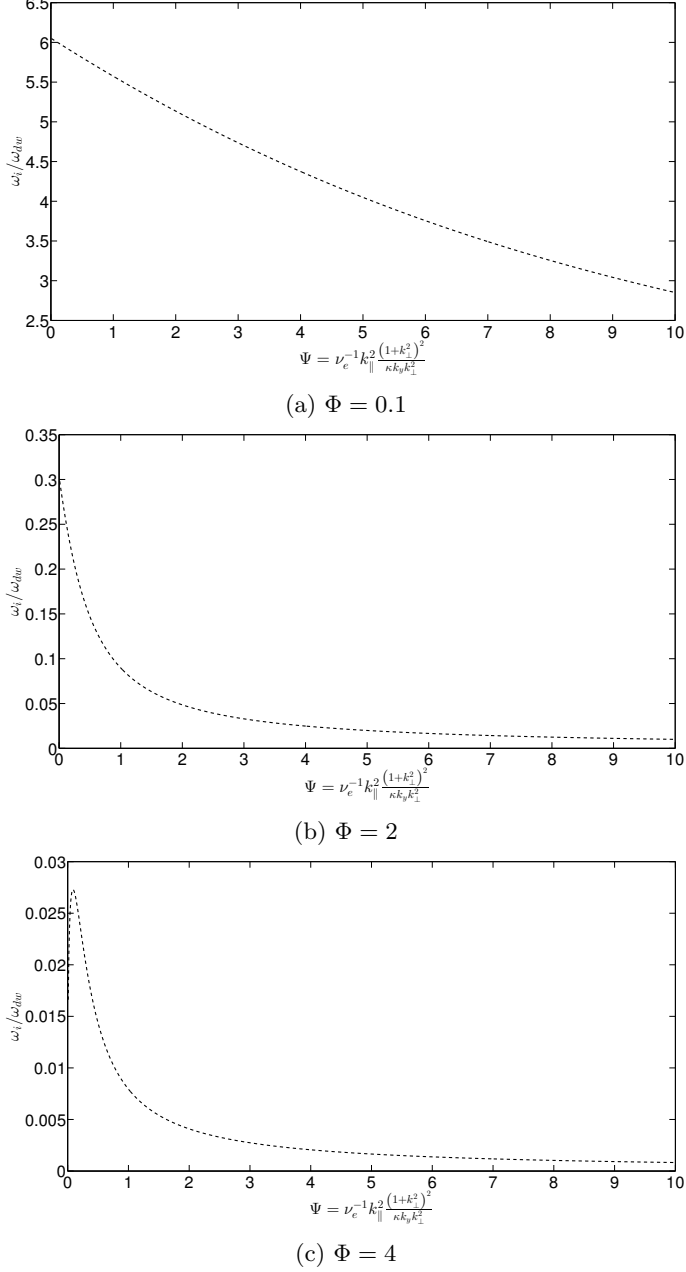


Figure 2.7: ω_i/ω_{dw} for different values of Φ as a function of Ψ .

Finally, to express this stabilising effect even further, Figure 2.8 shows three plots for different values of Ψ with increasing Φ . Upon comparing Figures 2.8a, 2.8b and 2.8c, which

show a cross-section of Figure 2.6 for $\Psi = 0.1$, $\Psi = 2$ and $\Psi = 4$, respectively, it is seen that the growth-rate drops faster towards 0 as Ψ is increased.

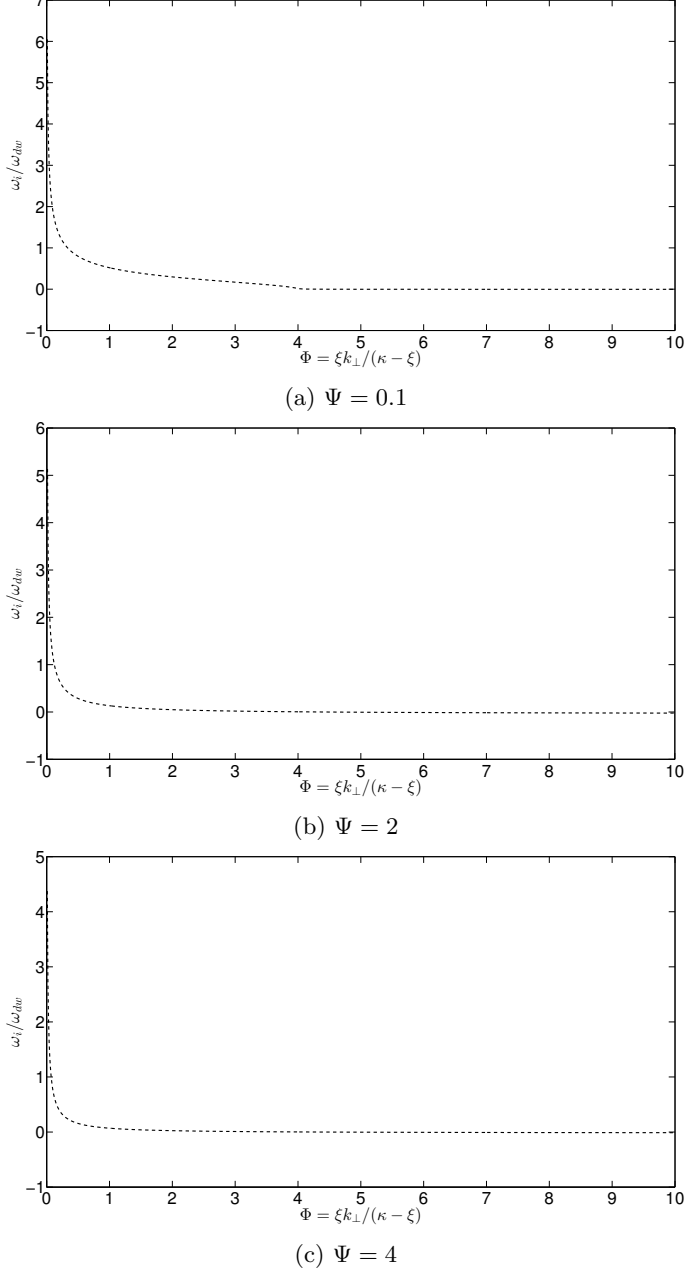


Figure 2.8: ω_i/ω_{dw} for different values of Ψ as a function of Φ .

So to summarize, in this chapter, simple equations governing the behaviour for a weakly and a fully ionized plasma have been derived. Although the models are greatly simplified, they do give a qualitative description of some of the properties of a magnetically confined plasma, including instabilities resulting from magnetic field curvature and drift-waves. It was found that a phase difference between the fluctuating potential and the fluctuating density is necessary for radial transport. Finally it was found that drift-waves have a stabilizing effect on the instability resulting from a curvature in the magnetic field.

Chapter 3

Numerical methods

With the analysis of the instability criteria for a simple two-fluid model at hand, the governing equations for a magnetically confined toroidal plasma can now be solved numerically. The equations are solved using an existing code, HESEL (Hot edge-SOL electrostatic turbulence), and the output data is then processed in order to find the position and velocity of the coherent structures resulting from these instabilities. This chapter first describes the HESEL code, then moves on to look at the numerical methods used for post-processing, including different methods for determining the position of the coherent structures resulting from the instabilities described in section 2.2.

3.1 The HESEL code

To conduct the simulations, an existing code developed to treat edge-SOL electrostatic turbulence, HESEL, is used. HESEL is an expanded version of the previous code ESEL, which solves a reduced 2-fluid model, similar to the model derived in chapter 2. The main differences between ESEL and Eq.'s (2.61) and (2.62) lie in the fact that the electron temperature is not assumed constant, so an equation for the electron temperature, found by taking the second moment of the Boltzmann equation, is included in ESEL. Also particle losses due to open magnetic field lines are included in the part treating SOL dynamics in ESEL, whereas they are neglected in the equations derived in chapter 2. The equations solved by ESEL are then given by[11]

$$\frac{d}{dt}n + n\mathcal{C}(\varphi) - \mathcal{C}(nT_e) = \Lambda_n, \quad (3.1)$$

$$\frac{d}{dt}\Omega - \mathcal{C}(nT_e) = \Lambda_\Omega, \quad (3.2)$$

$$\frac{d}{dt}T_e + \frac{2T_e}{3}\mathcal{C}(\varphi) - \frac{7T_e}{3}\mathcal{C}(T_e) - \frac{2T_e^2}{3n}\mathcal{C}(n) = \Lambda_T, \quad (3.3)$$

where $\Omega = \nabla_\perp^2\varphi$ is the vorticity, $\varphi = \frac{e\phi}{T_{e0}}$ and Bohm normalization has been used. Furthermore, $\frac{d}{dt} = \frac{\partial}{\partial t} + B^{-1}\hat{\mathbf{z}} \times \nabla\varphi \cdot \nabla$ is the convective derivative, and $\mathcal{C} \equiv -\xi \frac{\partial}{\partial y}$ is the curvature term. The influence of sinks, sources and dissipation is described by $\Lambda_n = D_n \nabla_\perp^2 n - \sigma_n n$ for the density equation, where D_n is collisional diffusion coefficient and σ_n represents particle losses due to transport along open magnetic field lines in the SOL. For the vorticity and temperature equations, n is replaced by Ω and T , respectively, in the definition of Λ , but it is otherwise described in the same way.

However the ESEL model assumes cold ions and although this is realistic for most basic

plasma physics experiments, it is not realistic for a tokamak edge-SOL plasma, where $T_i > T_e$ typically[12]. It has therefore been expanded to implement the following effects[13]

- finite ion temperature in the form of dynamical evolution of the ion pressure
- ion inertia response to the ion diamagnetic drift in the vorticity equation
- collisional terms from Braginskii fluid closure in the drift fluid solution of the perpendicular part of the momentum equation
- sheath boundary conditions parametrized through sheath damping term in the vorticity equation

and the expanded code is called HESEL. The HESEL code is based on a four-field Braginskii fluid model, which describes the evolution of the density, generalised vorticity and electron and ion pressures, solving the four equations[14]

$$\frac{d}{dt}n + n\mathcal{K}(\varphi) - \mathcal{K}(p_e) = \Lambda_n \quad (3.4)$$

$$\frac{d^0}{dt}\omega + \{\nabla\varphi, \nabla p_i\} - \mathcal{K}(p_e + p_i) = \Lambda_\omega \quad (3.5)$$

$$\frac{3}{2}\frac{d}{dt}p_e + \frac{5}{2}p_e\mathcal{K}(\varphi) - \frac{5}{2}\mathcal{K}\left(\frac{p_e^2}{n}\right) = \Lambda_{p_e} \quad (3.6)$$

$$\frac{3}{2}\frac{d}{dt}p_i + \frac{5}{2}p_i\mathcal{K}(\varphi) + \frac{5}{2}\mathcal{K}\left(\frac{p_i^2}{n}\right) - p_i\mathcal{K}(p_e + p_i) = \Lambda_{p_i} \quad (3.7)$$

with the RHS defined as

$$\Lambda_n = (1 + 1.6q^2) D_n (1 + \tau) \nabla_\perp^2 n - \frac{n}{\tau_n} \quad (3.8)$$

$$\Lambda_\omega = (1 + 1.6q^2) D_\omega \nabla^2 \nabla^2 \varphi^* - \frac{\omega}{\tau_\omega} + \frac{c_s}{L_\parallel} \left[1 - \exp\left(\varphi_w - \frac{\langle\varphi\rangle}{\langle T_e \rangle}\right) \right] \quad (3.9)$$

$$\begin{aligned} \Lambda_{p_e} = & (1 + 1.6q^2) D_n \left(\frac{5}{2} (1 + \tau) \nabla_\perp^2 p_e + \left(\frac{13}{6} - \frac{5}{2} \tau \right) \nabla \cdot (n \nabla_\perp T_e) \right. \\ & \left. + (1 + \tau) \nabla_\perp \ln n \cdot \nabla_\perp p_i \right) - \frac{p_e}{\tau_{\parallel,p_e} n} - \frac{3m_e}{m_i} \nu_{ei} (p_e - p_i) \end{aligned} \quad (3.10)$$

$$\begin{aligned} \Lambda_{p_i} = & (1 + 1.6q^2) \left(\frac{5}{2} D_n (1 + \tau) \nabla \cdot (T_i \nabla_\perp n) - D_n (1 + \tau) \nabla_\perp \ln n \cdot \nabla_\perp p_i \right. \\ & \left. + 2 \frac{T_{i0} \nu_{ii0}}{m_i \omega_{ci}^2} [\nabla_\perp^2 p_i - p_i \nabla_\perp^2 \ln n - \nabla_\perp \ln \cdot \nabla_\perp p_i] \right) \\ & - \frac{p_i}{\tau_{\parallel,p_i}} + \frac{3m_e}{m_i} \nu_{ei} (p_e - p_i) + p_i \Lambda_\omega. \end{aligned} \quad (3.11)$$

Note that in the above equations Bohm normalization has been used in all terms. n is the fluctuating part of particle density, $\omega = \nabla^2\phi + \nabla^2p_i$ is the generalized vorticity, n_0 is the background density, φ is the electrostatic potential, $\varphi^* = \varphi + p_i/(n_0e)$, p_i and p_e are the ion and electron pressure, respectively, and $\tau = T_i/T_e$. The temperatures are defined as $T_{i,e} = p_{i,e}/n$. Furthermore, ν_{ii0} is the ion-ion collision frequency given by,

$$\nu_{ii0} = \frac{n_0 Z^4 e^4 l_e}{12\pi^{3/2} e^2 \sqrt{A m_i} (e T_i)^{3/2}}, \quad \text{with } l_e = \ln\left(\frac{12\pi n_0 \rho_d^3}{Z}\right), \quad \text{and } \rho_d = \sqrt{\frac{\epsilon_0 T_e}{n_0 e}} \quad (3.12)$$

ν_{ei} is the electron-ion collision frequency given by

$$\nu_{ei} = \sqrt{2} \frac{n_0 Z^2 e^4 l_e}{12\pi^{3/2} e^2 \sqrt{m_e} (eT_e)^{3/2}}, \quad (3.13)$$

normalised by the ion cyclotron frequency, ω_{ci} , in the equations. The material derivatives and curvature operator are defined as $\frac{d}{dt} = \frac{\partial}{\partial t} + \frac{1}{B} \hat{\mathbf{z}} \times \nabla \varphi \cdot \nabla$ and $\mathcal{K} = \nabla \left(\frac{1}{B} \right) \cdot \hat{\mathbf{z}} \times \nabla$ respectively. $\frac{d^0}{dt}$ is the material derivative with a constant magnetic field. Friction forces are taken into account with D_n and D_ω , where D is the diffusion coefficient, given by

$$D_n = \rho_e^2 \nu_{ei}, \quad \text{with } \nu_{ei} = \sqrt{2} \frac{n_0 Z^2 e^4 l_e}{12\pi^{3/2} \epsilon_0^2 \sqrt{m_e} (eT_e)^{3/2}}, \quad (3.14)$$

$$D_\omega = \rho_i^2 \nu_{ii}, \quad \text{with } \nu_{ii} = \frac{n_0 Z^4 e^4 l_e}{12\pi^{3/2} \epsilon_0^2 \sqrt{A m_i} (eT_i)^{3/2}}, \quad (3.15)$$

where both are normalized by $\omega_{ci} \rho_s^2$ in the equations. τ_n , τ_ω and τ_{\parallel,p_i} denote damping terms modelling losses due to advection along the magnetic field lines in the SOL region, and are given by

$$\tau_n = \frac{L_\parallel}{6} \frac{1}{M_p c_s \sqrt{1 + \tau}} \quad (3.16)$$

$$\tau_\omega = \frac{L_\parallel}{6} \frac{1}{M_p c_s \sqrt{1 + \tau}} \quad (3.17)$$

$$\tau_{\parallel,p_i} = \frac{3}{2} \frac{L_\parallel}{6} \frac{1}{M_p c_s \sqrt{1 + \tau}} \frac{2}{9}, \quad (3.18)$$

which are all normalized by ω_{ci} in the equations, and where M_p is the parallel mach number accounting for tokamak geometry, and the $2/9$ in τ_{\parallel,p_i} accounts for adiabatic expansion. The parallel electron heat conduction is modelled with the damping rate τ_{\parallel,p_e} given by

$$\tau_{\parallel,p_e} = \frac{3}{2} L_\parallel^2 \nu_{ee} \left(1 + 3.2 \frac{1}{0.8 \nu_{es}} \right) \frac{1}{3.2 v_e^2} \quad \text{with } \nu_{ee} = \frac{n_0 e^4 l_e}{12\pi^{3/2} \epsilon_0^2 \sqrt{m_e} (eT_e)^{3/2}}, \quad (3.19)$$

$$v_e = \sqrt{\frac{eT_e}{m_e}} \quad \text{and} \quad \nu_{es} = \frac{L_\parallel \nu_{ei}}{v_e}, \quad (3.20)$$

also normalized by ω_{ci} . Tokamak geometry and poloidal magnetic field lines are accounted for by a neo-classical Pfirsch-Schlüter correction to the diffusion coefficients given by the term $(1 + 1.6q^2)$, where q denotes the safety factor at the LCFS.

The effect of sheath currents is approximated by an effective sheath dissipation given by the term $c_s/L_\parallel \left(1 - \exp(\varphi_w - \langle \varphi \rangle) \right)$, where $L_\parallel = 2\pi R_0$ is the parallel connection length, φ_w is the wall potential and $\langle \cdot \rangle$ denotes a poloidal average[15].

The HESEL code is solved in a 2D domain located at the out-board mid plane of a tokamak, which includes an edge region with closed magnetic field lines, and a SOL with open magnetic field lines. The HESEL code does, however, still neglect ionization effects, parallel dynamics (flows and currents) and only uses a first order approximation to finite ion Larmor radius (FLR) effects. Furthermore, the code is also imposing the local approximation described in chapter 2, so the full dynamics of magnetically confined plasmas is not completely captured by the model and it is not expected to be valid at high amplitude perturbations or very high ion temperatures. Despite these simplifications, the HESEL code has shown to fit well with experimental data[16], and this is the model used to examine the behaviour of coherent structures.

Due to the normalization used in HESEL, all in the following sections are given in terms of dimensionless units following Bohm normalization, unless otherwise specified.

3.2 Definition of blob position

The main purpose of this project has been to investigate the dynamics of coherent structures (blobs) in a magnetically confined plasma. The dynamics are simulated using the HESEL code described in section 3.1, which outputs the four fields from Eq. (3.4) to (3.7) at different time steps. However, the fields do not provide the position of the blob, which is necessary for describing the dynamics. The first step in the post-processing has therefore been how to define the position of the coherent structure. Three different methods have been investigated.

Position

The first method investigated is where the position is defined as the center of mass of the blob given by

$$\mathbf{x}_{CoM} \equiv \frac{1}{\int(n - n_0)d\mathbf{x}} \int(n - n_0)\mathbf{x} \cdot d\mathbf{x}, \quad (3.21)$$

where n is the density profile, n_0 is the background density and \mathbf{x} is (x, y) . The integral can be approximated by two sums to discretize the definition of the centre of mass;

$$x_{CoM} = \frac{1}{\sum_{i=1}^{p_x} \sum_{j=1}^{p_y} (n_{i,j} - n_0) \Delta x \Delta y} \sum_{i=1}^{p_x} \sum_{j=1}^{p_y} (n_{i,j} - n_0) x_i \Delta x \Delta y, \quad (3.22)$$

$$y_{CoM} = \frac{1}{\sum_{i=1}^{p_x} \sum_{j=1}^{p_y} (n_{i,j} - n_0) \Delta x \Delta y} \sum_{i=1}^{p_x} \sum_{j=1}^{p_y} (n_{i,j} - n_0) x_j \Delta x \Delta y, \quad (3.23)$$

where $p_{x,y}$ are the lengths of the simulation domain in the radial and poloidal directions, respectively, and $\Delta x, y$ are the corresponding step sizes. Finally x_i denotes the radial coordinate and x_j denotes the poloidal coordinate.

The second method investigated is where the position is defined as the point where the blob has the maximum amplitude given by

$$x_m = x(\max(n(x, y))), \quad (3.24)$$

$$y_m = y(\max(n(x, y))). \quad (3.25)$$

Finally, the third definition investigated is where the position of the blob is defined as the point where 50 % of the density is located, found by solving for x_p and y_p in the equations

$$\frac{1}{\int(n - n_0)d\mathbf{x}} \int_0^{x_p} \int_0^{L_y} (n - n_0) dy dx = 0.5, \quad (3.26)$$

$$\frac{1}{\int(n - n_0)d\mathbf{x}} \int_0^{L_x} \int_0^{y_p} (n - n_0) dy dx = 0.5, \quad (3.27)$$

where $L_{x,y}$ are the radial and poloidal lengths of the system in question, and x_p and y_p are the coordinates for the position. As for the center of mass, this can be discretized as

$$\frac{1}{\sum_{i=1}^{p_x} \sum_{j=1}^{p_y} (n_{i,j} - n_0) \Delta x \Delta y} \sum_{i=1}^{x_p} \sum_{j=1}^{p_y} (n_{i,j} - n_0) \Delta x \Delta y \approx 0.50, \quad (3.28)$$

$$\frac{1}{\sum_{i=1}^{p_x} \sum_{j=1}^{p_y} (n_{i,j} - n_0) \Delta x \Delta y} \sum_{i=1}^{p_x} \sum_{j=1}^{y_p} (n_{i,j} - n_0) \Delta x \Delta y \approx 0.50 \quad (3.29)$$

The three different methods are compared in Figure 3.1.

Figure 3.1a shows a plot of a large blob with a width of $\sigma = 40$ after $t = 2500$ with $\tau = 0.5$. Here the blob forms the well known mushroom shape as usually seen in the low ion-temperature limit[17]. The black cross is (x_m, y_m) , the magenta dot is (x_{CoM}, y_{CoM}) and the blue circle is (x_p, y_p) . In this limit, the center of mass and 50% positions are very similar and estimate the position to be centred between the tails of the blob, slightly behind the blob front, where the position of the maximum point is located on the lower blob tail. However, when increasing the ion temperature, the blob does not generate the typical mushroom shape, but instead moves both in the radial and poloidal direction, retaining much of its structure as also seen in [17] and illustrated in Figure 3.1b. This behaviour will be investigated further in chapter 4, but the analysis here is restricted to comparing the different definitions of blob position. The plot shows a large blob with $\sigma = 40$ after $t = 2500$ with $\tau = 3.5$, and here it is seen that the centre of mass scheme determines the position of the blob behind the blob front, and above where the majority of the propagating mass is located. The 50% point is located slightly behind the centre of mass in the radial direction, but is located closer to where the majority of the propagating mass is in the poloidal coordinate. The maximum value here is located almost at the wave front and close to the centre of the propagating mass, which seems to be a better estimate of the blob position than the other two.

For the center of mass and 50% schemes there is also a problem finding the poloidal position when the blob is not centred, as seen in Figure 3.1c or when it propagates too close to the edge, as seen in Figure 3.1d, due to periodic boundary conditions used in the poloidal direction in HESEL. Therefore care needs to be taken when determining the poloidal position. If the blob is not centred, the poloidal coordinate needs to be moved correspondingly, and if the blob moves too close to the edge, a bigger simulation domain is required.

Velocity

The velocity of the blob has been calculated using a finite difference method with an error of δt^4 , where δt is the time-step using¹

$$\frac{d}{dt}\mathbf{x}(t) = \frac{8\mathbf{x}(t + \delta t) - 8\mathbf{x}(t - \delta t) - \mathbf{x}(t + 2\delta t) + \mathbf{x}(t - 2\delta t)}{12\delta t} + O(\delta t^4), \quad (3.30)$$

where $\mathbf{x} = (x, y)$ is the position of the blob, t is the given time-step and δt is the time-step size. The script for calculating the positions and the velocity can be seen in Appendix B. The different definitions of coordinate positions give rise to different maximum velocities when using Eq. (3.30). These velocities are compared in Figure 3.2.

In Figure 3.2a it is seen that the velocity of the maximum value is higher than that of the center of mass, and that the 50% position is somewhere between the two for a blob with $\sigma = 10$, $\Delta n = n_0$ and $T_e = 10$ eV.

The same behaviour is seen for larger blobs as seen in Figure 3.2b, and for both lower and higher initial blob amplitudes, as seen in Figures 3.2c and 3.2d, respectively. From the figures it is also clear that both the definition using the point of maximum amplitude, and the definition using the 50% point as the position of the blob generate stepwise increases in the maximum velocity for different temperature ratios due to them being tied to a grid-point. This step-wise increase is not seen for the centre of mass scheme, since it can be positioned between grid-points, which means that the centre of mass is better for determining differences in maximum velocities.

From the analysis it is seen that the centre of mass scheme and the 50% scheme do not fully describe the position of propagating part of the blob, whereas the point of the maximum amplitude seems to capture the position of the propagating mass fairly well. However both

¹See appendix A.1.8 for the derivation.

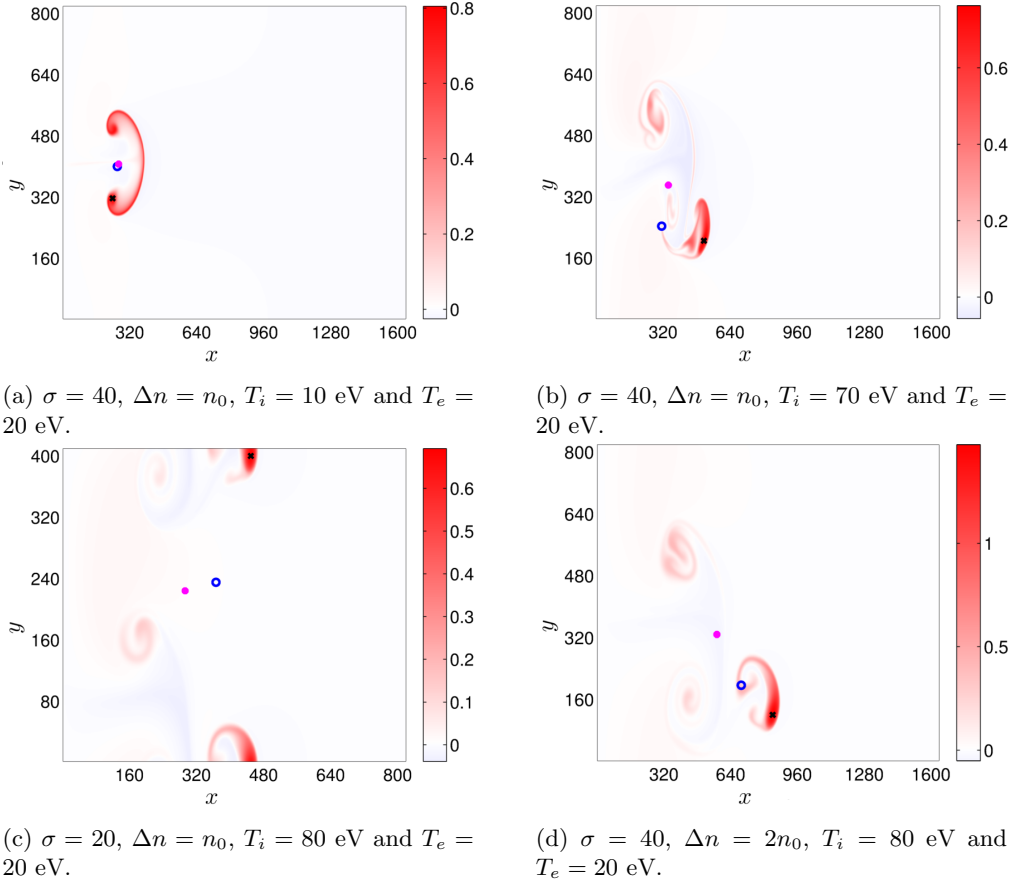


Figure 3.1: A plot of a blob after $t = 2500$ for different initial parameters. The black cross denotes the position of the maximum value, the magenta dot denotes the position of the center of mass and the blue circle denotes the 50% position.

the maximum amplitude and the 50% schemes are tied to specific grid-points, so they do not estimate the velocity correctly when using a finite difference scheme. Furthermore, the center of mass is also a measure for the $\mathbf{E} \times \mathbf{B}$ -flux[17], and since it is widely used in papers on scaling laws (see for example [6] or [17]), this is the coordinate used throughout the rest of the paper, unless otherwise specified.

To fully describe the blob position, the maximum amplitude and the centre of mass schemes could be combined, so the position is calculated from the centre of mass of a box with a width equal to that of the initial blob, centred around the point of maximum amplitude. However due to the limited time available for this project, this is left to be tested in future works.

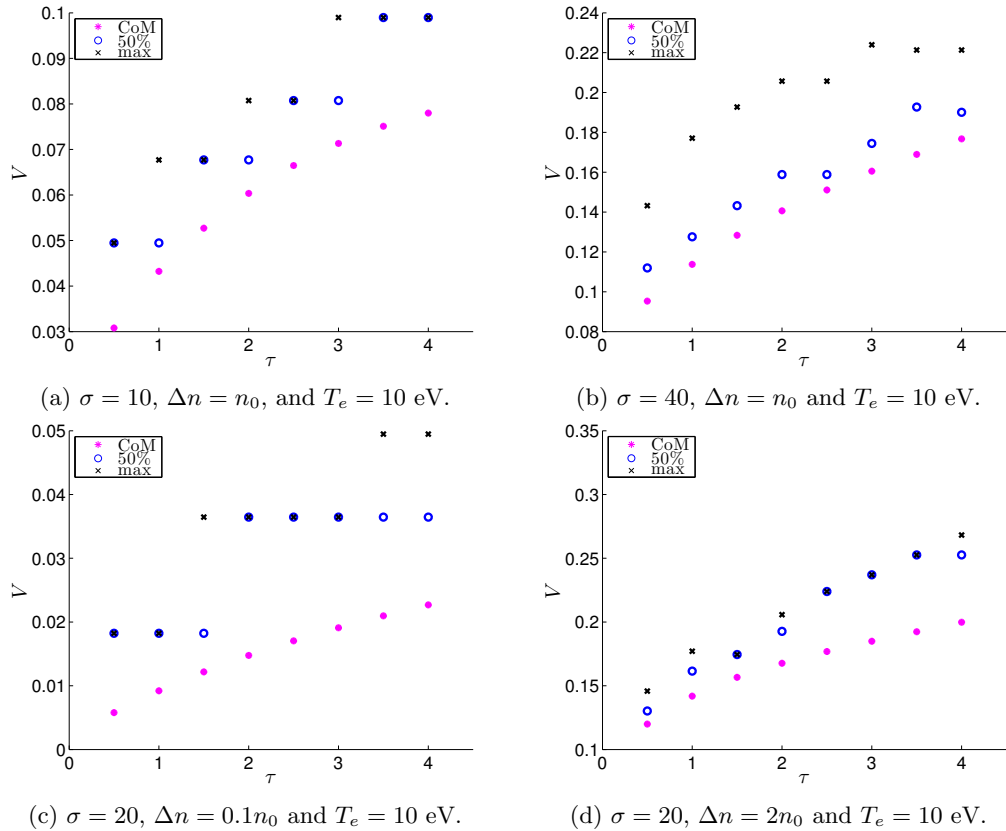


Figure 3.2: A plot of the maximum radial velocity for different values of τ for blobs with different initial parameters. The black cross denotes the velocity of the maximum value, the magenta dot denotes the velocity of the center of mass and the blue circle denotes the 50% velocity.

Chapter 4

Simulation results

With the definitions of the blob position at hand and a description of the code used to solve the dynamical equations governing blob behaviour, the next step is to examine the dynamics of these blobs. Perturbations driving the instabilities are initialized by creating a seeded blob in the simulation domain. Two different regimes are examined using the HESEL code, one for blobs in a toroid-shaped device with a weakly ionized plasma, and one for blobs in a tokamak device with a fully ionized plasma. In this chapter simulations are initially carried out using parameters from the TORPEX device and compared with other codes and experimental results. Then the dynamics of a fully ionized plasma, using the dimensions from the ASDEX device, are investigated, and finally these simulations are compared with different scaling laws for blob velocities.

4.1 Weakly ionized plasma

In order to validate the code, simulations were carried out using input parameters corresponding to the TORPEX device in Lausanne and compared with experimental results and other numerical solvers. However TORPEX differs significantly from other fusion experimental devices on several parameters. The shape is that of a torus, not a tokamak, it is smaller than typical fusion devices and is only around 5% ionized. Since HESEL is written for tokamak geometry fusion plasmas, several alterations have been made to account for the differing parameters and geometry. The main change has been to incorporate collisions with neutrals, since these are expected to dominate diffusion for a weakly ionized plasma, as described in chapter 2.

The left-hand side (LHS) of the HESEL equations solved are the same as Eq.'s (3.4) to (3.7) in chapter 3, but the RHS has been redefined for TORPEX and these are now given as

$$\Lambda_n = D_{\nu n} \nabla_{\perp}^2 n - D_{\nu n} \nabla_{\perp}^2 \varphi - \frac{n}{\tau_n} \quad (4.1)$$

$$\Lambda_{\omega} = D_{\omega} \nabla^2 \nabla^2 \varphi^* - \nu_{in} \omega + \frac{c_s}{L_{\parallel}} \left[1 - \exp \left(\varphi_w - \frac{\langle \varphi \rangle}{\langle T_e \rangle} \right) \right] \quad (4.2)$$

$$\Lambda_{p_e} = D_{\nu n} \frac{5}{2} \nabla_{\perp}^2 p_e - \frac{p_e}{\tau_{\parallel, p_e} n} \quad (4.3)$$

$$\begin{aligned} \Lambda_{p_i} = & \left(\frac{5}{2} D_{\nu n} \nabla \cdot (T_i \nabla_{\perp} n) - D_{\nu n} \nabla_{\perp} \ln n \cdot \nabla_{\perp} p_i \right. \\ & + 2 \frac{T_{i0} \nu_{ii0}}{m_i \omega_{ci}^2} [\nabla_{\perp}^2 p_i - p_i \nabla_{\perp}^2 \ln n - \nabla_{\perp} \ln \cdot \nabla_{\perp} p_i] \Big) \\ & - \frac{p_i}{\tau_{\parallel, p_i}} + p_i \Lambda_{\omega}. \end{aligned} \quad (4.4)$$

Collisions with neutrals have been taken into account by replacing τ_{ω} with the ion-neutral collision frequency ν_{in} normalized by ω_{ci} and by incorporating them in the density diffusion coefficient so $D_{\nu n} = \nu_{en} \rho_s^2$. Furthermore, effects due to tokamak geometry, in the form of Phirsch-Schlüter corrections, have been removed, and ion temperatures are assumed small, so $\tau \ll 1$.

Since the device is small and has limiters placed in the reaction chamber, sheath currents are expected to have a significant influence on the blob dynamics. The effect of sheath currents is therefore included and is approximated by an effective sheath dissipation, where L_{\parallel}^1 is the parallel connection length.

4.1.1 Simulation parameters

To conduct the simulations for a perturbation of a weakly ionized plasma, several parameters need to be initialized. For TORPEX, these parameters are given[18] in Table 4.1

Table 4.1: Parameters for TORPEX

| | Symbol | Value |
|----------------------------------|-----------------|--------------------------------------|
| Toroidal magnetic field at R_0 | B_0 | $B_0 = 0.075$ T |
| Major radius | R_0 | 1 m |
| Minor radius | r_0 | 0.2 m |
| Parallel mach number | M_p | 1 |
| Mass number | A | 1 |
| Charge number | Z | 1 |
| Electron density at LCFS | n_e | 2.5×10^{15} m ⁻³ |
| Parallel connection length | L_{\parallel} | 3 m |
| Electron temperature | T_e | 2.8 eV |

Furthermore, the electron and ion collision frequencies are given as $\nu_{en} \approx 1 \times 10^6$ s⁻¹ and $\nu_{in} \approx 3 \times 10^4$ s⁻¹[18], respectively, which is verified by theoretical calculations when using

¹The parallel connection length is taken to be $L_{\parallel} = L_{TORPEX}/2$ due to the symmetry of the system, where the longest distance to the limiter is $L_{TORPEX}/2$.

the ion sound velocity for the ions and the electron thermal velocity for the electrons[19]

$$\nu_{en} = n_n \sigma_n \sqrt{\frac{8k_b T_e}{\pi m_e}} = 1.1 \times 10^6 \text{ s}^{-1} \quad (4.5)$$

$$\nu_{in} = n_n \sigma_n \sqrt{\frac{8k_b T_e}{\pi m_i}} = 2.6 \times 10^4 \text{ s}^{-1}, \quad (4.6)$$

assuming a neutral density of $n_n = 10^{20} \text{ m}^{-3}$, and a neutral cross-section $\sigma_n = 10^{-20} \text{ m}^2$.

The density profiles associated with the device are given in [18] as

$$n_{bg}(r) = -4.2 \times 10^{17} r^{2.9} + 2.5 \times 10^{15} \text{ [m}^{-3}\text{]}, \quad (4.7)$$

and

$$T_{e,bg}(r) = 2.8 \times \exp(-5.9r) \text{ [eV].} \quad (4.8)$$

Since n_{bg} becomes negative for large values of r when using this definition, a numerical restriction is imposed where, if the background density reaches 1% of the initial value at $r = 0$, the background is assumed to be $n_{bg}(r) = 0.01n_{bg}(0)$.

Finally the profiles for the seeded blobs are given as

$$n(r, z) = n_0 \exp \left[- \left(\frac{r - r_0}{\sigma_{rn}} \right)^2 - \left(\frac{z}{\sigma_{zn}} \right)^2 \right] \text{ [m}^{-3}\text{]} \quad (4.9)$$

$$T_e(r, z) = T_{e,0} \exp \left[- \left(\frac{r - r_0}{\sigma_{rT}} \right)^2 - \left(\frac{z}{\sigma_{zT}} \right)^2 \right] \text{ [eV]} \quad (4.10)$$

$$\begin{aligned} \phi(r, z) = & \phi_1 \exp \left[- \left(\frac{r - r_0}{\sigma_{r\phi,1}} \right)^2 - \left(\frac{z - z_1}{\sigma_{z\phi,1}} \right)^2 \right] + \phi_2 \exp \left[- \left(\frac{r - r_0}{\sigma_{r\phi,2}} \right)^2 - \left(\frac{z - z_2}{\sigma_{z\phi,2}} \right)^2 \right] \\ & + \lambda T_e(r, z) \text{ [V],} \end{aligned} \quad (4.11)$$

The constant values are all given within a 68% confidence interval for three different blobs in [18] and λ is given as $\lambda = 3$. For the simulations the mean values of the confidence intervals, seen in Table 4.2 for the density and electron temperature profiles and in Table 4.3 for the potential, are used. It should be noted that the sign of the polarization of the potential has been swapped compared to [18] due to the direction of the magnetic field in HESEL being opposite of the one used in TORPEX.

Table 4.2: The values for the density and electron temperature profiles used for the seeded blob simulations in TORPEX.

| | r_0 [m] | n_0 [10^{15} m^{-3}] | σ_{rn} [m] | σ_{zn} [m] | $T_{e,0}$ [eV] | σ_{rT} [m] | σ_{zT} [m] |
|--------|-----------|------------------------------------|-------------------|-------------------|----------------|-------------------|-------------------|
| case 1 | 0.07 | 1.975 | 0.022 | 0.024 | 0.345 | 0.0105 | 0.0365 |
| case 2 | 0.07 | 2.335 | 0.024 | 0.021 | 0.96 | 0.0105 | 0.0145 |
| case 3 | 0.07 | 4.395 | 0.0165 | 0.0175 | 1.73 | 0.008 | 0.0285 |

Table 4.3: The values for the potential used for the seeded blob simulations in TORPEX.

| | ϕ_1 [V] | $\sigma_{r\phi,1}$ [m] | $\sigma_{z\phi,1}$ [m] | z_1 [m] | ϕ_2 [V] | $\sigma_{r\phi,2}$ [m] | $\sigma_{z\phi,2}$ [m] | z_2 [m] |
|--------|--------------|------------------------|------------------------|-----------|--------------|------------------------|------------------------|-----------|
| case 1 | -2.33 | 0.033 | 0.0295 | 0.0255 | 1.54 | 0.031 | 0.04 | -0.022 |
| case 2 | -4.6 | 0.0325 | 0.031 | 0.026 | 2.35 | 0.0275 | 0.0475 | -0.005 |
| case 3 | -4.75 | 0.0495 | 0.049 | 0.0115 | 6.155 | 0.0305 | 0.025 | -0.0245 |

The boundary conditions used are periodic in the poloidal direction and are

- Dirichlet/Neumann on ϕ with $\phi(0) = \lambda T_{e,bg}(0)$ and $\phi'(L_x) = 0$,
- Dirichlet/Dirichlet on ω with $\omega(0) = 0$ and $\omega(L_x) = 0$,
- Dirichlet/Neumann on n with $n(0) = n_{bg}(0)$ and $n'(L_x) = 0$,
- Dirichlet/Neumann on p_e with $p_e(0) = T_{e,bg}(0)n_{bg}(0)$ and $p'_e(L_x) = 0$,
- Dirichlet/Neumann on p_i with $p_i(0) = T_{i,bg}(0)n_{bg}(0)$ and $p'_i(L_x) = 0$,

in the radial direction. The ions are assumed to be at room temperature, so $T_{i,bg}$ is assumed to be 0.025 eV throughout the entire domain.

Finally, since there are several different ways of defining the blob position, as mentioned in chapter 3, the blob position in this section is defined in compliance with the methods used in other codes simulating TORPEX. Due to noise in the system, the definition of the blob positions are defined as the center of mass for the position where the saturation current has a value higher than a threshold of 20%, or in other words the center of mass where

$$\sum_0^x j_{sat} = 0.2 \sum_0^{p_x} j_{sat}, \quad (4.12)$$

where p_x is the radial length of the domain, and solving for the radial position x . Since HESEL does not provide a measure of the saturation current, it is used that it is given by[8]

$$j_{sat} = n \sqrt{\frac{T_e}{m_i}} e A, \quad (4.13)$$

where A is the area of the probe used to measure the current. From this it is seen that $j_{sat} \propto n \sqrt{T_e}$ so the position from which to calculate the center of mass is found by solving for x in

$$\sum_0^x n \sqrt{T_e} = 0.2 \sum_0^{p_x} n \sqrt{T_e}, \quad (4.14)$$

4.1.2 Comparisons with experimental values

With the initialization of the seeded blobs at hand, it is now time to look at the results from the simulations. In order to compare the simulations and experimental results, the density profiles of the seeded blobs for both the experimental case and the HESEL simulations are investigated. Since no experimental data is presented for case 3, the comparisons are restricted to case 1 and 2, and since the interest of the comparison lies with the blob, the background is removed by subtracting a reference simulation with no seeded blob from the actual blob simulations.

Case 1

First the blob with the parameters given for case 1 in Tables 4.2 and 4.3 is examined, since this blob has the lowest initial potential and density and is therefore expected to fit best with the simulations.

The density profiles for the simulated and experimental blobs at different time steps are seen in Figure 4.1. Already in the initialization of the blob it is seen that the density profile provided in [18], seen in Figure 4.1a, is very simplified compared to the experimental data seen in Figure 4.1b, which may explain some of the deviations observed.

At later times, seen in Figure 4.1c, the blob moves in the radial direction, but is skewed slightly in the poloidal direction, likely due to the sheath condition in the vorticity equation

and the initial potential. Upon comparing it with the experimental result at the same time seen in Figure 4.1d, it is seen that the position in the radial direction appears to be very close to that of the experimental value, but the simulated blob moves in the opposite direction of the experimental one, likely due to the direction of the magnetic field being opposite in HESEL compared to TORPEX. Assuming that the effect of a reversed magnetic field is a poloidal displacement of the same magnitude but in the opposite direction (see for example [20]), it is possible to compare the magnitudes of the displacement. Doing this, it is seen that the experimental blob has moved further in the poloidal direction than the simulated one, which may be caused by parallel effects neglected in HESEL. A much weaker damping is also observed in the simulation compared to the experiment, which could also be due to the lack of parallel dynamics or due to missing damping terms, but this will need to be investigated further in future studies.

At $t = 40 \mu\text{s}$, the radial position of the simulation, seen in Figure 4.1e, still seems to fit well with the experiment, seen in Figure 4.1f. It is also seen that the simulated blob has moved further in the poloidal direction, but still not as far as the experiment. Since the movement in the poloidal direction for low ion temperatures is mainly due to parallel effects, and the only parallel effect included in HESEL is the sheath dissipation, this may explain the lack of propagation in the poloidal direction. However, the simulated blob is barely damped, in sharp contrast to the experimental blob, which has dropped to a maximum density of around half the initial value. This difference is most likely not solely due to lack of parallel dynamics, and the different damping terms need to be investigated further in order to determine the origin of the large difference between the simulation and the experiment.

Case 2

Next, the blob with the parameters given for case 2 in Tables 4.2 and 4.3 is investigated. This blob has a slightly higher amplitude and initial potential, which means that the blob is expected to move faster than in case 1, and since the blob amplitude is higher, a larger difference between HESEL and the experiment is expected due to the local approximation used in the code.

Here the density profiles at different time-steps for both the experimental case and the simulation are seen in Figure 4.2. As for case 1, the initial blob is very simplified compared to the experimental values as seen when comparing Figure 4.2a with Figure 4.2b, which again may explain some of the deviations observed.

Also, upon comparing Figure 4.2c with Figure 4.2d, which is a plot of the density profile at $t = 20 \mu\text{s}$ for the simulation and the experiment, respectively, a good match is seen between the simulation and the experimental profile in terms of radial positions at the time $t = 20 \mu\text{s}$. However, as for case 1, a much smaller magnitude of the poloidal displacement is seen, and, again, there is a very low dissipation compared to the experiment.

At later times the simulated blob moves further in the poloidal direction compared to case 1, as seen in Figure 4.2e, but the magnitude of the displacement is still much smaller than in the experiment, seen in Figure 4.2f. Looking at the radial positions of the simulated and the experimental blobs, it is also observed that the simulated blob has moved further than the experiment, which is likely due to the local approximation in HESEL. Again the dissipation is much lower in the simulation compared to the experiment, and the simulated blob is stretched over a large area, where the experimental blob seems to retain its shape throughout the entire time series.

From the above comparisons it is concluded that HESEL does not describe the weakly ionized blobs well in terms of dissipation, poloidal propagation and compactness of the blob. Furthermore, the velocity in HESEL for higher amplitude blobs is estimated too high, likely due to the local approximation imposed in the code. These deviations from the

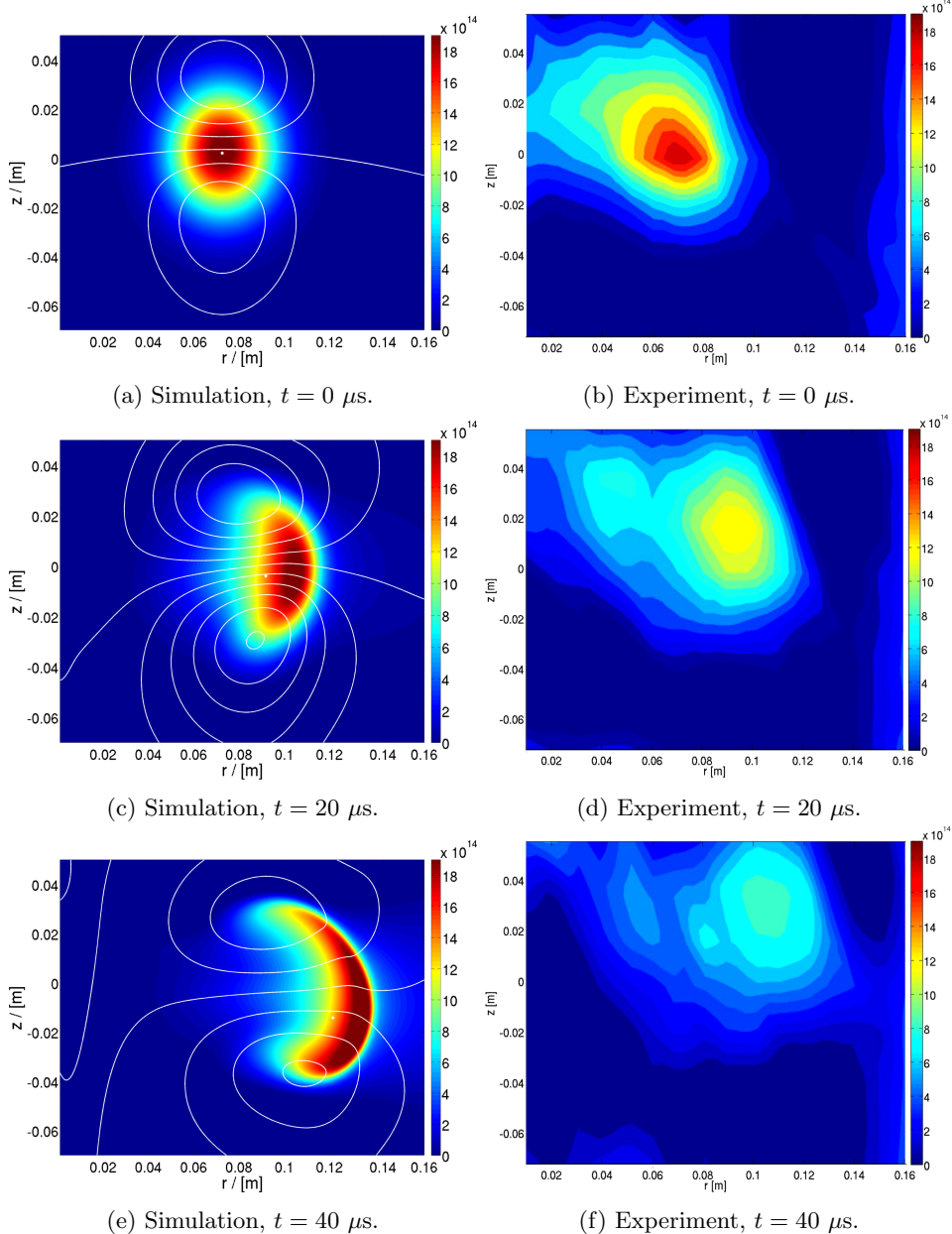


Figure 4.1: Contour plots of the density profiles of the seeded blob for case 1 at different times. The colour scale is in units of m^{-3} , the white contours indicate the electrostatic potential and the white dots indicates the calculated position. To the left are the simulation density profiles and to the right are the experimental density profiles.

experimental results will need to be investigated further in future works in order to fully describe where the differences between the experiment and the assumptions used in the code lie.

However, since HESEL, and most other codes, are designed for fully ionized fusion plasmas, several of the assumptions used are likely not valid for TORPEX. It is therefore also interesting to compare different codes using the same initial parameters, since they use the same assumptions.

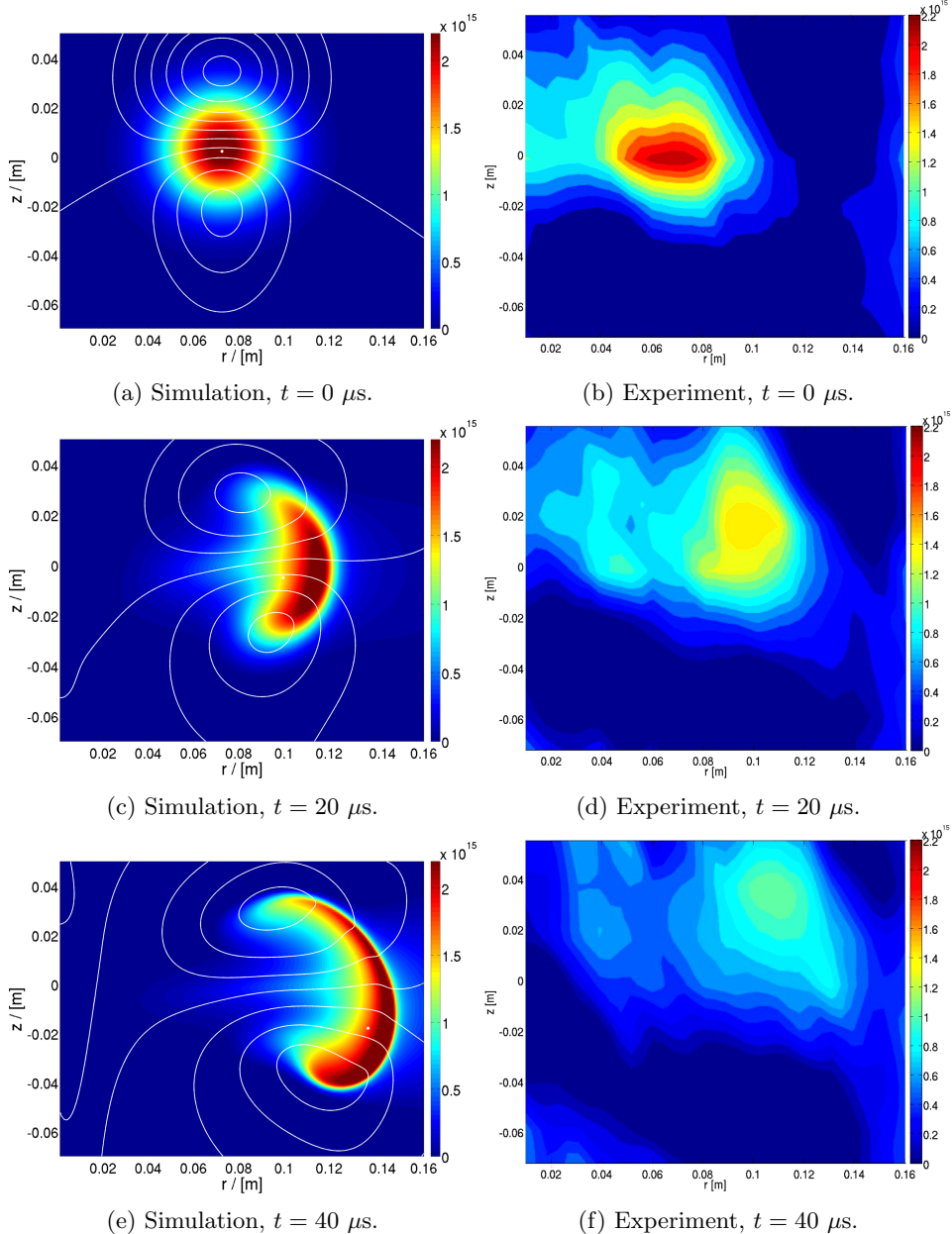


Figure 4.2: Contour plots of the density profiles of the seeded blob for case 2 at different times. The colour scale is in units of m^{-3} , the white contours indicate the electrostatic potential and the white dots indicates the calculated position. To the left are the simulation density profiles and to the right are the experimental density profiles.

4.1.3 Comparison with BOUT++ and GBS

Since the initialization of the blob is very simplified compared to the experiment, and since TORPEX differs significantly from the parameter range in which HESEL usually operates, the analysis of the seeded blobs is supported by comparing the results with other simulations. The codes for which data for TORPEX is available are the BOUT++ code, which is a full 3D code used at the Culham Centre for Fusion Energy, and the GBS code, which is also a full 3D code based on a global two-fluid braginskii model, used by EPFL.

Again the comparison is restricted to case 1 and 2 due to the data available for the other codes, and again the background has been removed for all codes to solely describe the dynamics of the blobs in question.

Case 1

For case 1, no data has been provided by GBS, so the comparison here is only done between BOUT++ and HESEL.

The radial and poloidal positions as a function of time for both codes are seen in Figure 4.3. Comparing the radial positions, seen in Figure 4.3a for HESEL and Figure 4.3b for BOUT++, it is seen that the evolution of the blob is estimated slightly higher in HESEL, and that it seems to accelerate slightly after $30 \mu\text{s}$, which is not seen in BOUT++. Apart from these small discrepancies, the overall behaviour seems to compare well and no major difference is seen in the radial position.

Looking at the poloidal direction, HESEL and BOUT++ are expected to behave differently due to the effect of parallel dynamics present in BOUT++. This difference in poloidal behaviour is verified by comparing Figure 4.3c with Figure 4.3d, which shows the poloidal position as a function of time for the blob using HESEL and BOUT++, respectively. The poloidal position of the blob found with HESEL propagates approximately twice as far in the poloidal direction as the one found using BOUT++, likely due to parallel dynamics, but again the overall behaviour of the blob is very similar in the two codes, which indicates that the sheath condition imposed captures some of the parallel effects. It should be noted that the sign on the poloidal position in Figure 4.3c has been swapped to take the direction of the magnetic field into account.

Case 2

For case 2, results were available for both BOUT++ and GBS, and a comparison between the three with respect to radial and poloidal position is carried out here.

Figure 4.4 shows the radial and poloidal positions as a function of time for all three codes. Again the propagation in the radial direction is investigated first, since this is where the codes are expected to be most similar. The overall behaviour between the radial position in HESEL, seen in Figure 4.4a, and in BOUT++, seen in Figure 4.4b, seem quite similar. However, as was also seen for case 1, a slight acceleration is observed after $30 \mu\text{s}$ in HESEL, which results in a radial displacement of the blob, which is much bigger than the one seen in BOUT++. The radial propagation of the blob in GBS is seen in the top part of Figure 4.4e, and it is observed that the blob in this code propagates much shorter than both HESEL and BOUT++. Also the behaviour of the blob propagation differs significantly from the other two codes, where GBS oscillates slightly, whereas the other two codes show a continuous forward propagation in the radial direction.

The poloidal propagation of the blob for case 2, seen in Figure 4.4c for HESEL, Figure 4.4d for BOUT++ and in the bottom of Figure 4.4e for GBS is again not expected to compare well due to the lack of parallel dynamics in HESEL. This is verified upon comparing the three different cases, where the HESEL blob propagates much further than the other two and seems to accelerate throughout the entire time, whereas BOUT++ decelerates after $40 \mu\text{s}$ and GBS decelerates around $50 \mu\text{s}$.

From the above, it is evident that HESEL does not capture the poloidal dynamics well for a blob with the parameters used in TORPEX. However both GBS and BOUT++ estimated the poloidal displacement to be less than what was estimated using HESEL, which again was less than seen in the experiment, so none of the codes seem to capture the blob behaviour. Furthermore, the radial displacement for case 2 was estimated much larger in HESEL, than in both other codes and the experiment, which could indicate some

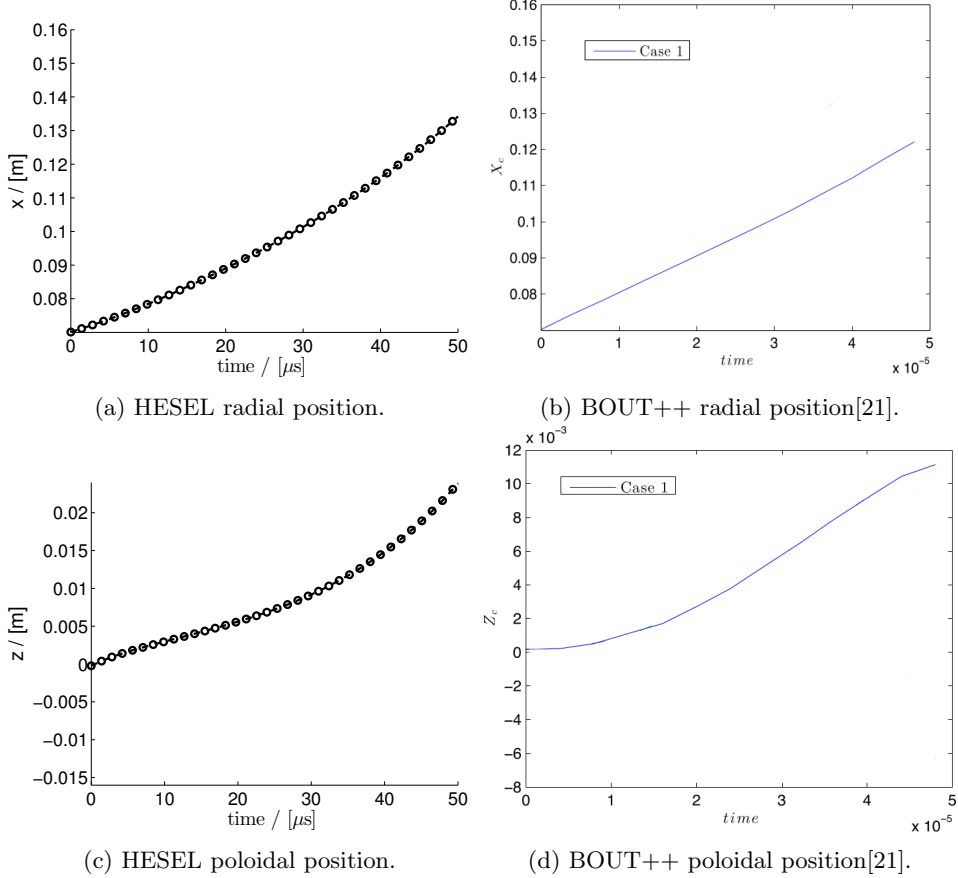


Figure 4.3: The blob positions as a function of time for case 1 for the different codes. The positions are all found using the definition given in Eq. (4.14). Note that the scale on the poloidal axis for HESEL is twice that of the one used for BOUT++.

errors or wrong assumptions used in HESEL. So although HESEL seems to capture the radial dynamics well for case 1, more work is needed in order to explain the difference in poloidal movement with both the other codes and the experiment. Also the dissipation between HESEL and the experimental results were very different which also needs to be further investigated. Finally the comparisons made here are not very comprehensive due to the limited amount of material available, so in order to do a full comparison with both the experiment and the other codes, more data is needed, for example the blob size and velocity profiles.

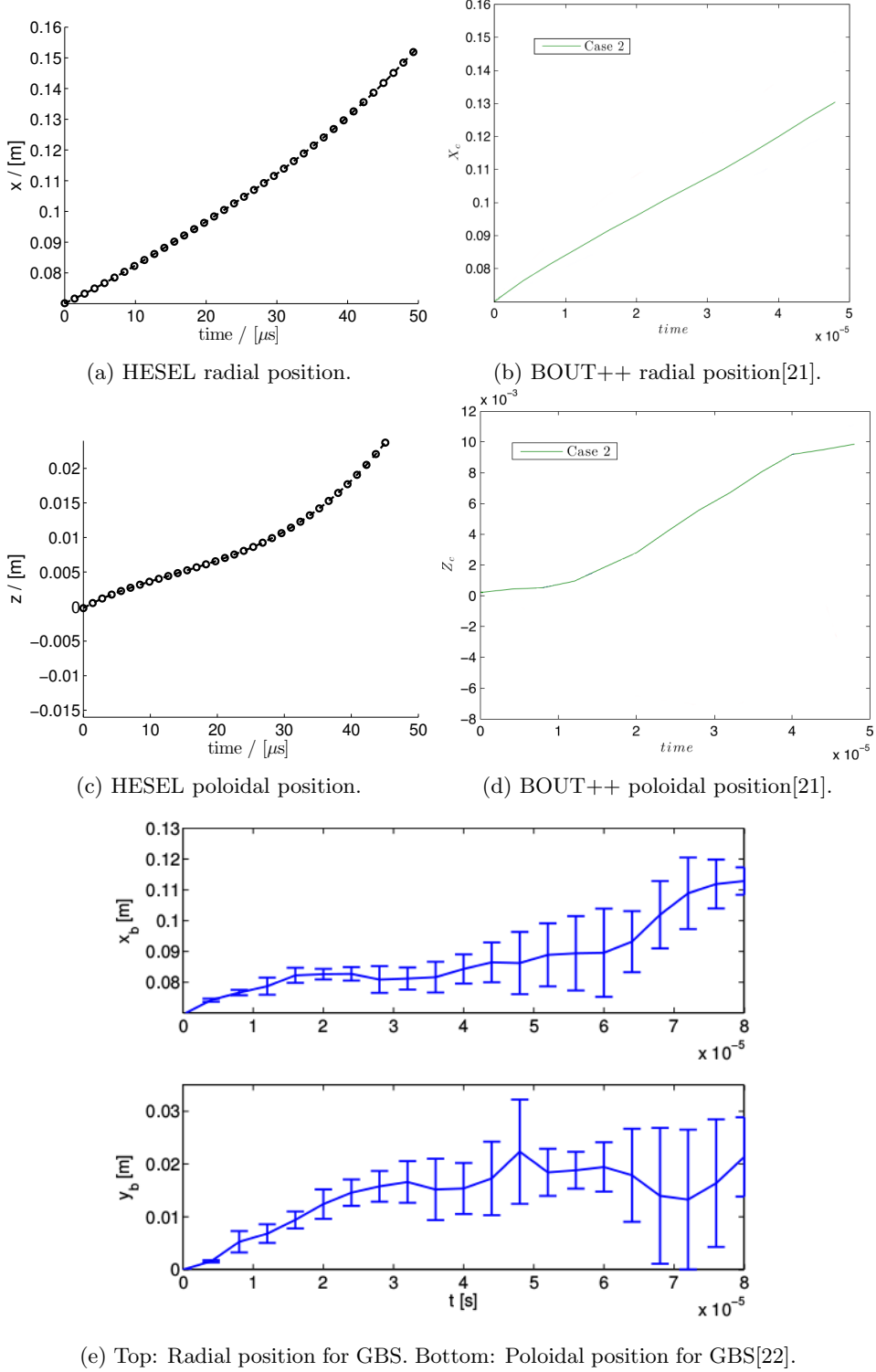


Figure 4.4: The blob positions as a function of time for case 2 for the different codes. The positions are all found using the definition given in Eq. (4.14). Note that the scale on the poloidal axis for HESEL is twice that of the one used for BOUT++.

4.2 Fully ionized plasma

Although the simulations for the weakly ionized plasma differed significantly from the experiment, it should be noted that HESEL is designed to describe the behaviour of fully ionized plasmas, and previous results in this regime have shown good agreement with experimental data[16]. The code is therefore used to examine blob behaviour in this regime, using parameters similar to those in the ASDEX device.

4.2.1 Simulation parameters

The constant parameters used in these simulations are given in Table 4.4. The edge region

Table 4.4: Parameters for ASDEX

| | Symbol | Value |
|----------------------------------|-----------------|-----------------------------------|
| Toroidal magnetic field at R_0 | B_0 | $B_0 = 1.86 \text{ T}$ |
| Major radius | R_0 | 1.65 m |
| Minor radius | r_0 | 0.5 m |
| Parallel mach number | M_p | 0.5 |
| Mass number | A | 2 |
| Charge number | Z | 1 |
| Electron density at LCFS | n_0 | $1 \times 10^{19} \text{ m}^{-3}$ |
| Parallel connection length | L_{\parallel} | 10 m |
| Safety factor at LCFS | q | 5 |

is set to fill the entire domain in order to disregard effects from the SOL and wall regions. Furthermore a ballooning term is implemented in D_n in the HESEL equations seen in chapter 3, to take tokamak geometry into account. All parallel effects in terms of drift-waves and sheath condition are neglected, so the only parallel effects taken into account when solving the HESEL equations, given in section 3.1, are the linear terms in the form of parallel damping. The boundary conditions used are periodic in the poloidal direction and are

- Dirichlet/Dirichlet on ϕ with $\phi(0) = 0$ and $\phi(L_x) = 0$,
- Dirichlet/Dirichlet on ω with $\omega(0) = 0$ and $\omega(L_x) = 0$,
- Dirichlet/Dirichlet on n with $n(0) = n_0$ and $n(L_x) = n_0$,
- Dirichlet/Dirichlet on p_e with $p_e(0) = T_{e0}n_0$ and $p_e(L_x) = T_{e0}n_0$,
- Dirichlet/Dirichlet on p_i with $p_i(0) = T_{i0}n_0$ and $p_i(L_x) = T_{i0}n_0$,

in the radial direction, where n_0 is the background density, T_{e0} is the initial electron temperature and T_{i0} is the initial ion temperature. The seeded blob is set as a Gaussian perturbation and has the form

$$n(x, y) = n_0 + \Delta n \exp\left(-\frac{r^2}{2\sigma^2}\right) \quad (4.15)$$

$$p_e(x, y) = T_e(x, y)n(x, y) \quad (4.16)$$

$$p_i(x, y) = T_i(x, y)n(x, y), \quad (4.17)$$

where Δn is the relative amplitude of the blob,

$$r = \sqrt{(x - x_0)^2 + (y - y_0)^2},$$

with x being the radial position and y being the poloidal position and σ is the initial width of the blob. Furthermore constant background temperatures and densities are used.

Finally it should be mentioned that the code is normalized using Bohm normalization as described in chapter 3, and all values are given in terms of dimensionless parameters unless otherwise stated.

4.2.2 Blob behaviour

In order to investigate the dynamics of these seeded blobs, several different initial parameters are varied. These are the blob amplitude, Δn , the blob radius radius σ , the ion temperature T_i and the electron temperature T_e .

From the simulations it is observed that small blobs tend to dissipate fast as is seen upon comparing Figure 4.5 with Figure 4.6, which show the propagation of a blob with a width of $\sigma = 5$ and $\sigma = 40$, respectively, but otherwise with the same parameters. This fast dissipation of small blobs is likely due to rapid convection and the resulting velocity shear, which causes Kelvin-Helmholtz vortices and vortex shedding[23]. The increased dissipation of smaller blobs is emphasized in Figure 4.7a, which shows the maximum amplitude as a function of time for different blob sizes all with $T_i/T_e \equiv \tau = 1$. The effect becomes even more evident for higher ion temperatures as seen in Figure 4.7b, which is a plot of the maximum density of the blob as a function of time for different blob sizes with $\tau = 3$.

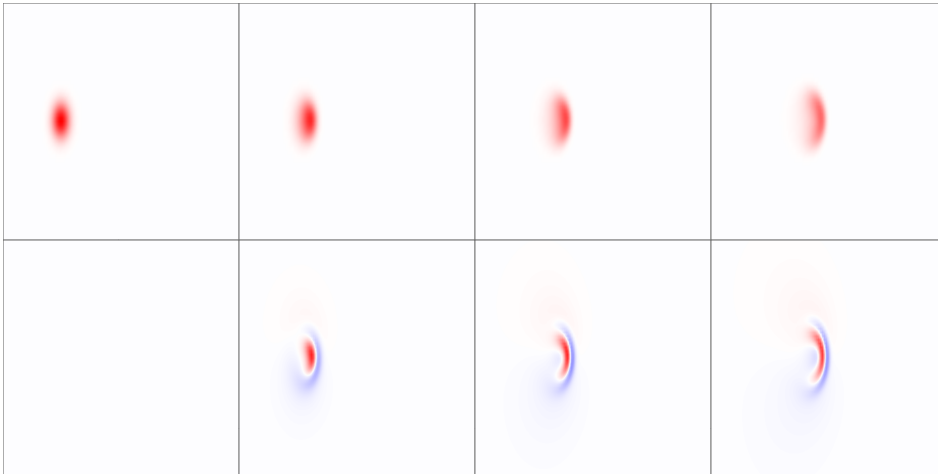


Figure 4.5: Top: Density of a blob minus the background with $\sigma = 5$, $T_i = 10$ eV, $T_e = 20$ eV, and an initial blob-amplitude of $\Delta n = n_0$. Bottom: Vorticity of the blob at the same time steps. The scaling in y is 0 to 35, the scaling in x is 0 to 50 and the time between each step is 500. The colour scheme is kept constant in both plots.

The increased difference in dissipation for higher ion temperatures is likely due to the behaviour of larger blobs at higher ion temperatures. For low ion temperatures, blobs develop the well-known mushroom-like structure[6] seen in Figure 4.6, which shows the propagation of a blob with $\sigma = 40$, $\Delta n = n_0$ and $\tau = 0.5$. However, as is also seen in the plot, the blob is slightly skewed downwards at later times due to the finite ion temperature used in the simulation, which destroys the invariance of the $\mathbf{E} \times \mathbf{B}$ velocity and the grad- \mathbf{B} drifts and causes the blob center of mass to move poloidally[20]. This effect is enhanced when the ion temperature is increased, where the blob does not display the characteristic mushroom shape, but instead begins to propagate downwards, leaving behind much of the initial mass and retaining its shape longer than in the cold ion case, as seen in Figure 4.8, which shows the propagation of a blob with $\sigma = 40$, $\Delta n = n_0$ and $\tau = 3.5$.

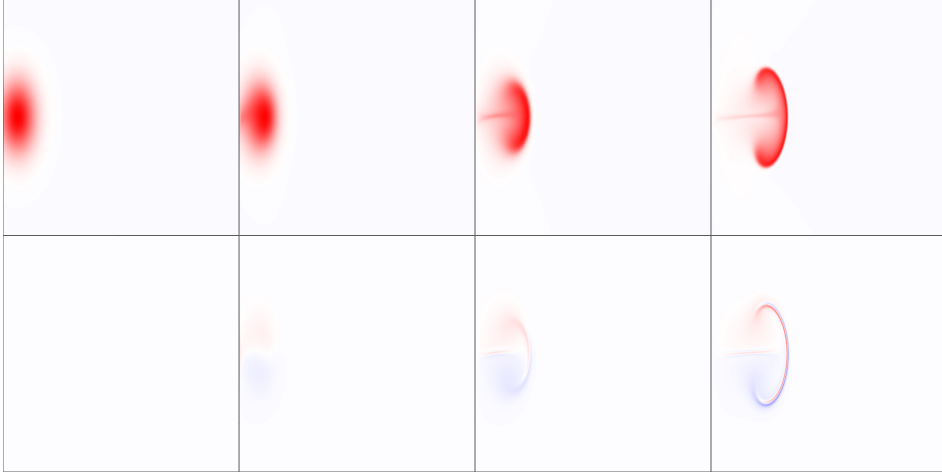


Figure 4.6: Top: Density of a blob minus the background with $\sigma = 40$, $T_i = 10$ eV, $T_e = 20$ eV, and an initial blob-amplitude of $\Delta n = n_0$. Bottom: Vorticity of the blob at the same time steps. The scaling in y is 0 to 100, the scaling in x is 0 to 200 and the time between each step is 500. The colour scheme is kept constant in both plots.

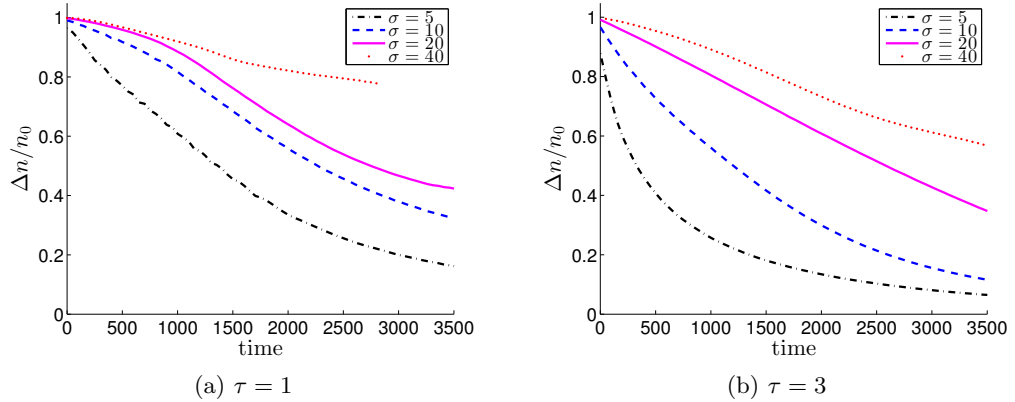


Figure 4.7: The maximum amplitude of different sizes of blobs with $\Delta n = n_0$ and $T_e = 20$ eV as a function of time. The only difference between the left and the right plots is the value of τ .

Also a larger amplitude of the initial blob has an effect on the dynamics. Increasing the initial blob amplitude increases the effects of finite ion temperatures, as seen in Figure 4.9, which is a plot of the propagation of a blob with $\sigma = 40$, $\Delta n = 5n_0$ and $\tau = 0.5$. The same blob behaviour is seen as for the case with a high ion temperature, but since the blob velocity is higher, the blob moves further both radially and poloidally. It is interesting to note that the blob reverses velocity in the poloidal direction after a period of time, vaguely seen in Figure 4.9 and even clearer in Figure 4.10, which is a plot of the propagation of a smaller blob with $\sigma = 20$ but otherwise the same parameters. This reversal of poloidal velocity is likely due to deceleration of the blob, which tilts the vorticity, driving the blob center of mass to reverse direction[20].

However for all cases it is seen that finite ion temperature causes the blob to retain much of its initial shape due to a sheared flow of particle and vorticity density around the blob, which prevents the formation of a steep blob front[20]. This difference between low and high ion temperatures in terms of the shape of the blob front is illustrated in Figure 4.11, which shows the evolution of $n(x, y_m, t)/n_0$ for a blob with $\sigma = 40$, $\Delta n = 2n_0$. The top

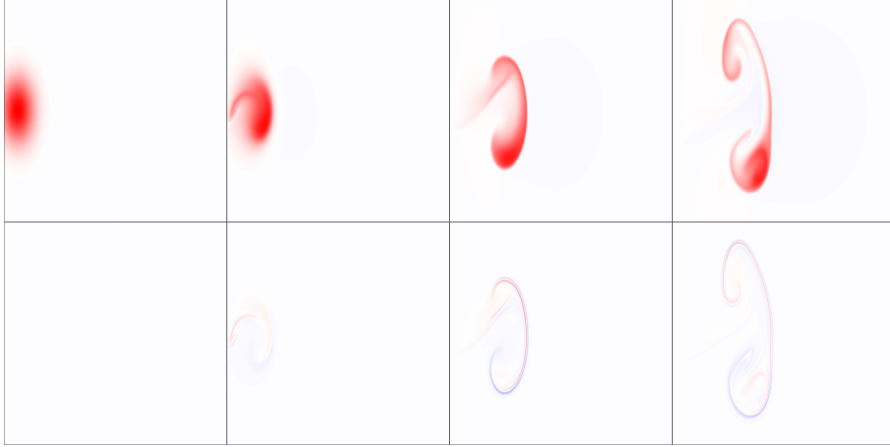


Figure 4.8: Top: Density of a blob minus the background with $\sigma = 40$, $T_i = 70$ eV, $T_e = 20$ eV, and an initial blob-amplitude of $\Delta n = n_0$. Bottom: Vorticity of the blob at the same time steps. The scaling in y is 0 to 100, the scaling in x is 0 to 200 and the time between each step is 500. The colour scheme is kept constant in both plots.

plot is for $\tau = 0.5$ and the bottom is for $\tau = 4$, and the difference between the two is clearly seen. The low ion temperature blob develops a steep front and propagates much shorter than the high ion temperature blob.

This difference in the blob front between low and high ion temperature blobs, and the fact that the blob shape is retained longer for warm ions, results in a reduced collisional induced energy dissipation[20]. This means that the blob travels further and retains a higher radial velocity for warm ion blobs. However the higher radial velocity is not immediately seen from the velocities in the center of mass scheme as illustrated Figure 4.12a, which shows the radial center of mass velocity as a function of time for a blob with $\sigma = 10$ and $\Delta n = n_0$ for different values of τ . This is due to the blob leaving behind much of the initial mass, which does not propagate radially. However upon looking at the radial velocity of the maximum amplitude, seen in Figure 4.12b with the same parameters as in Figure 4.12a, it is verified that the warm ion blobs retain a higher radial velocity due to the more composed shape. Despite these differences between the blobs for different parameters, it is seen from Figures 4.12a and 4.12b that the radial velocity peaks early and gradually slows down.

Despite the less steep blob front at higher ion temperatures, the dissipation for warmer ion blobs is larger than that of blobs with a low ion temperature as seen in Figure 4.13a, which shows the maximum density of the blob as a function of time for a blob with $\sigma = 10$ and $\Delta n = n_0$ for different values of τ . The faster dissipation of the high temperature blobs is likely due to their higher velocity, which results in additional velocity shear and thus faster dissipation. For high amplitude blobs, the difference between the dissipations of low and high temperature blobs is not as great as for lower amplitudes, as seen in Figure 4.13b, which shows the maximum blob amplitude as a function of time for a blob with $\sigma = 10$ and $\Delta n = 2n_0$. This is likely due to the increased velocity resulting from a higher initial amplitude, which means that the velocity difference between small and large blobs is not as great.

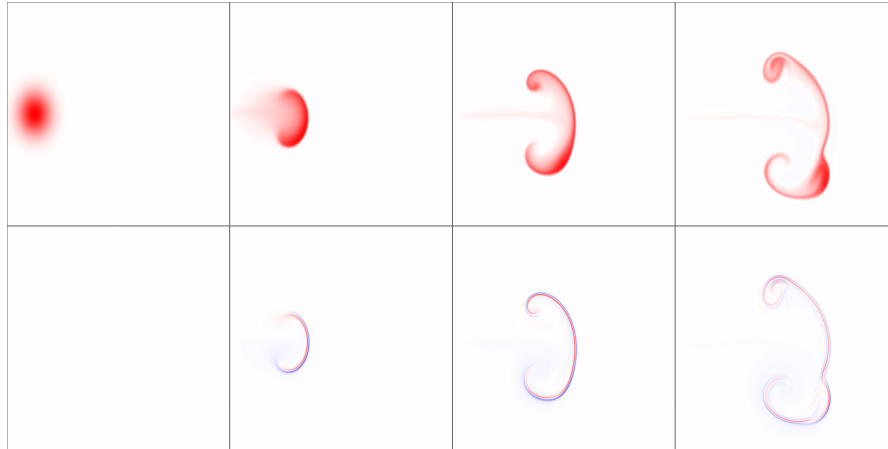


Figure 4.9: Top: Density of a blob minus the background with $\sigma = 40$, $T_i = 10$ eV, $T_e = 20$ eV, and an initial blob-amplitude of $\Delta n = 5n_0$. Bottom: Vorticity of the blob at the same time steps. The scaling in y is 0 to 150, the scaling in x is 0 to 200 and the time between each step is 500. The colour scheme is kept constant in both plots.

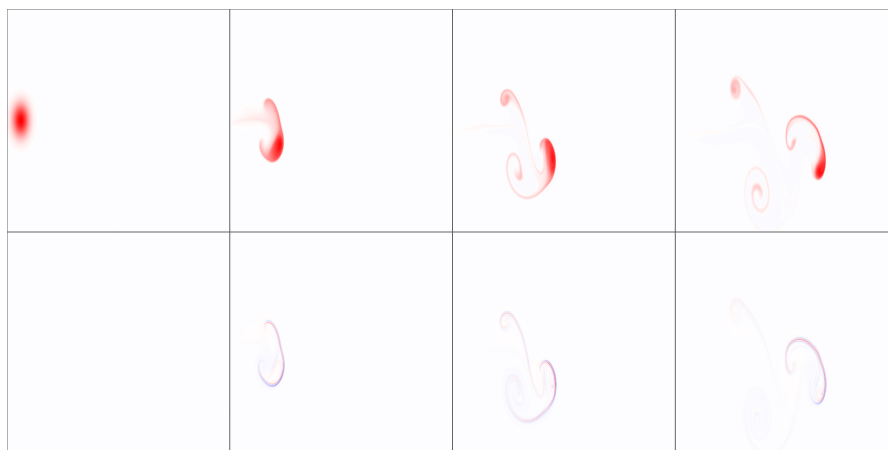


Figure 4.10: Top: Density of a blob minus the background with $\sigma = 20$, $T_i = 10$ eV, $T_e = 20$ eV, and an initial blob-amplitude of $\Delta n = 5n_0$. Bottom: Vorticity of the blob at the same time steps. The scaling in y is 0 to 100, the scaling in x is 0 to 200 and the time between each step is 500. The colour scheme is kept constant in both plots.

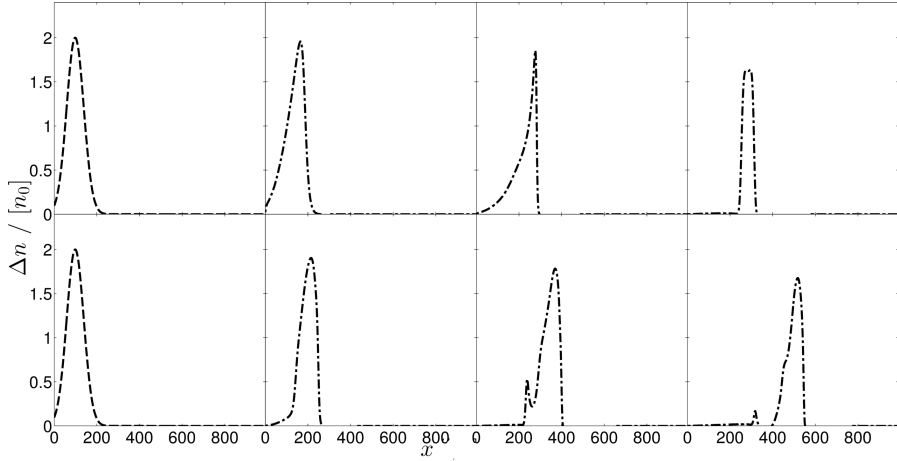


Figure 4.11: Top: A plot of $n(x, y_m, t)/n_0$ for a blob with $\sigma = 40$, $\Delta n = 2n_0$ and $\tau = 0.5$ at different time-steps in increments of 500. Bottom: A plot of $n(x, y_m, t)/n_0$ for a blob with $\sigma = 40$, $\Delta n = 2n_0$ and $\tau = 4$ at different time-steps in increments of 500.

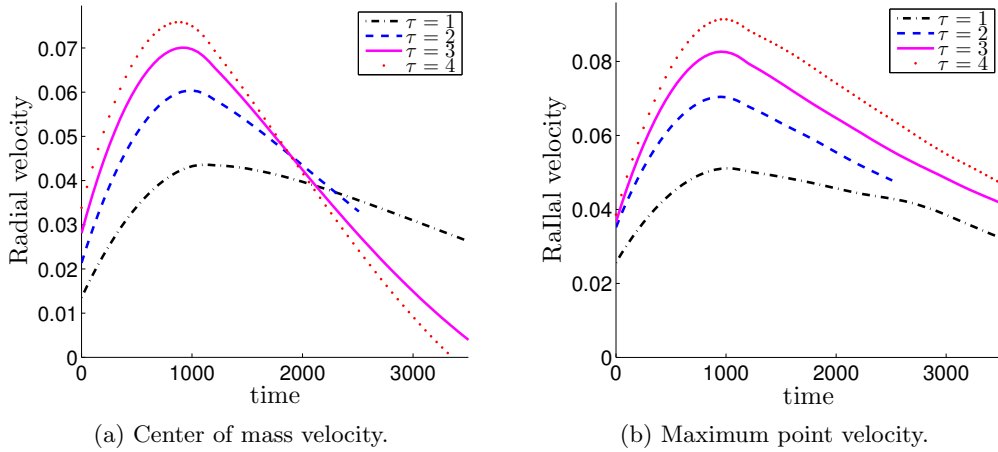


Figure 4.12: Radial velocity of the center of mass (left) and the maximum point (right) as a function of time for several different τ for a blob with $\sigma = 10$, $\Delta n = n_0$ and an electron temperature of $T_e = 10$ eV.

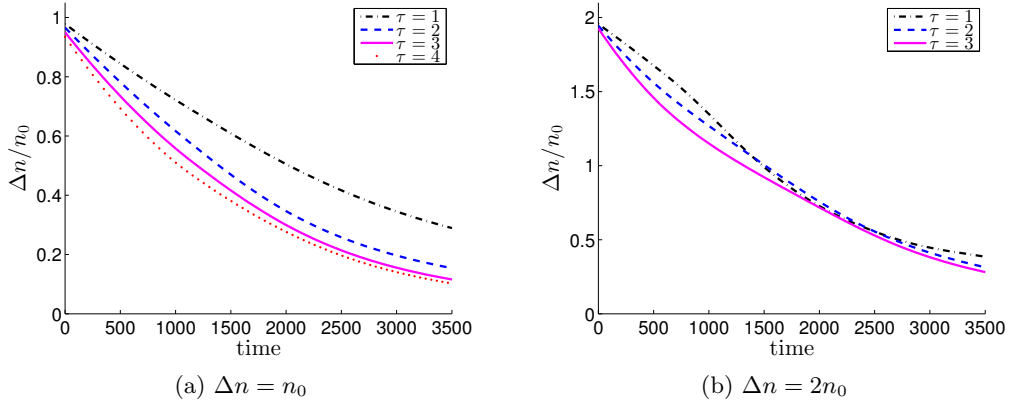


Figure 4.13: The maximum amplitude of a blob with $\sigma = 10$ and $T_e = 10$ eV as a function of time for different τ . The left plot is for a blob with $\Delta n = n_0$ and the right is for a blob with $\Delta n = 2n_0$.

4.2.3 Scaling laws

Due to the same initial behaviour of all blobs with a velocity that peaks early and gradually slows down, it is interesting to investigate the scaling laws of the maximum velocity. These scaling laws have been studied extensively in previous works (see for example [6] or [24]), and are found by equating terms in the vorticity equation and doing a dimensional analysis.

A simple scaling is found[6] by linearising Eq. (3.5), neglecting damping and equating the terms

$$\frac{d^0}{dt}\omega \approx V^2 \quad (4.18)$$

and

$$\mathcal{K}(p_e + p_i) \approx \frac{\Delta n}{n_0}(T_e + T_i), \quad (4.19)$$

and finally reverting to dimensional units. Defining the sound speed as $c_s = \sqrt{eT_e/m_i}$ leads to a velocity scaling given by

$$\frac{V}{c_s} \approx \left(\frac{2\sigma}{R_0} \frac{\Delta n}{n_0} \right)^{1/2} (1 + \tau)^{1/2} \quad (4.20)$$

This velocity scaling indicates that $V \rightarrow \infty$ as $\Delta n/n_0 \rightarrow \infty$, however for large $\Delta n/n_0$ the local approximation used in HESEL is no longer valid, and the interchange term becomes independent of amplitude[24], which means that the velocity scales as

$$\frac{V}{c_s} \approx \left(\frac{2\sigma}{R_0} \frac{\Delta n}{n_0 + \Delta n} \right)^{1/2} (1 + \tau)^{1/2}, \quad (4.21)$$

for a global model, which has the limiting behaviour $V \rightarrow c_s (2\sigma/R_0)^{1/2} (1 + \tau)^{1/2}$ as $\Delta n \rightarrow \infty$. This behaviour is not expected in HESEL due to the local approximation used, but it has been included in this analysis to show the large difference between the local and global models for high amplitude blobs.

However the scalings shown in Eq. (4.20) and Eq. (4.21) neglect the contribution from the nonlinear term in Eq. (3.5), $\{\nabla\phi, \nabla p_i\}$, and use a vorticity defined as $\Omega = \nabla^2\phi$, so the ion pressure used in the definition of the generalized vorticity is not taken into account either. A different scaling based on a model similar to HESEL is therefore proposed by P. Manz in [12], given by

$$\frac{V}{c_s} = \sqrt{\frac{\sqrt{f_i^2 + g^2} - f_i}{2}}, \quad (4.22)$$

where

$$f_i = \left(\frac{\tau \rho_s}{2\sigma} \frac{\Delta n}{n_0} \right)^2, \quad \text{and} \quad g = (1 + \tau) \frac{2\sigma}{R} \frac{\Delta n}{n_0}. \quad (4.23)$$

For large σ , Eq. (4.21) is retrieved, except for a factor of $1/\sqrt{2}$, and for small blobs the velocity scales as

$$\frac{V}{c_s} \approx \frac{1 + \tau}{\tau} \left(\frac{\sigma}{\rho_s} \right)^2 \frac{\rho_s}{R}, \quad (4.24)$$

which is independent of amplitude and scales as σ^2 instead of $\sigma^{1/2}$.

These three scaling laws are all compared with numerical results of the maximum value found using HESEL for different initial blob parameters in order to investigate whether these analytical estimates explain the blob behaviour observed in HESEL.

Dependence on blob size

The first parameter dependence investigated is that between the maximum radial velocity and the initial width of the blob. Figure 4.14 illustrates this dependence for the simulation and the different scaling laws for four different cases.

The first case, seen in Figure 4.14a, is for a small amplitude, low ion temperature blob, where the local and global models are similar and where FLR effects are less significant for blob dynamics. It is seen that all scalings estimate the maximum velocity too high for this case. However the overall velocity scaling seems to be captured well by Eq. (4.22) with the σ^2 dependence for small blobs and the $\sqrt{\sigma}$ dependence for large blobs, where both the local and global model seem to overestimate the effect of larger blobs and do not describe the size dependence observed for small blobs. The same behaviour is seen when the ion temperature is increased, as illustrated in Figure 4.14b. Again all scalings overestimate the radial velocity dependence of blob size, and again the scaling proposed by Manz seems to capture the overall behaviour best, although none of the scalings are accurate.

Increasing the blob amplitude to $\Delta n = 0.5n_0$, as seen in Figure 4.14c, the scaling proposed by Manz fits well with the observed maximum velocities of the blob, whereas, again, both the local and global models overestimate the velocity and do not describe the velocity scaling with small blobs.

Even when the blob amplitude is increased further, as seen in Figure 4.14d, where the local scaling seems to capture the behaviour well for large σ , Eq. (4.22) seems to better describe the blob dependence for small blobs. But both this scaling and the global scaling underestimate the velocity.

It is thus concluded that none of the scaling laws describe the scaling with initial blob size well, but that the scaling proposed by Manz gives a better description of the behaviour at small blob sizes. However it is also seen that both ion temperature and blob amplitude have a significant effect on the maximum velocity.

Dependence on ion temperature

The next thing investigated is therefore the dependence of the maximum blob velocity on τ . Figure 4.15 illustrates this dependence for the simulation and the different scaling laws for four different cases.

Again a small amplitude blob is investigated first due to the similarity between the local and global models here. Figure 4.15a shows the maximum velocity dependence on τ for blobs with $\Delta n = 0.1n_0$, $\sigma = 20$ and $T_e = 10$ eV. From the figure it is seen that all three scaling laws overestimate the velocity, and the deviation from the simulation increases for the local and global models, likely due to the lack of FLR effects in these. When increasing the blob amplitude to $\Delta n = 2n_0$, the global model estimates the velocities too low as expected due to the local approximation used in HESEL as seen in Figure 4.15b. Despite the local approximation in HESEL, the local velocity scaling model still overestimates the velocity in this case, and it deviates further from the simulation results as the ion temperature is increased, which again is likely due to the lack of FLR effects in the derivation of Eq. (4.20). The scaling proposed by Manz does not capture the evolution of the blob velocity well with these parameters, and looking at the equation, it is seen that $f_i \propto \Delta n^2$ and $g \propto \Delta n$, so the term $\sqrt{f_i^2 + g^2} - f_i \rightarrow 0$ as $\Delta n \rightarrow \infty$, which does not fit well with the observed behaviour. Furthermore it is also seen that $f_i \propto \tau^2$ and $g_i \propto \tau$, which also means the term $\sqrt{f_i^2 + g^2} - f_i \rightarrow 0$ as $\tau \rightarrow \infty$. The scaling thus predicts a slow radial velocity for high amplitude, high ion temperature blobs, which does not agree with the blob behaviour observed in section 4.2.2, so this scaling is not expected to agree well with the simulations for high amplitude, high temperature blobs.

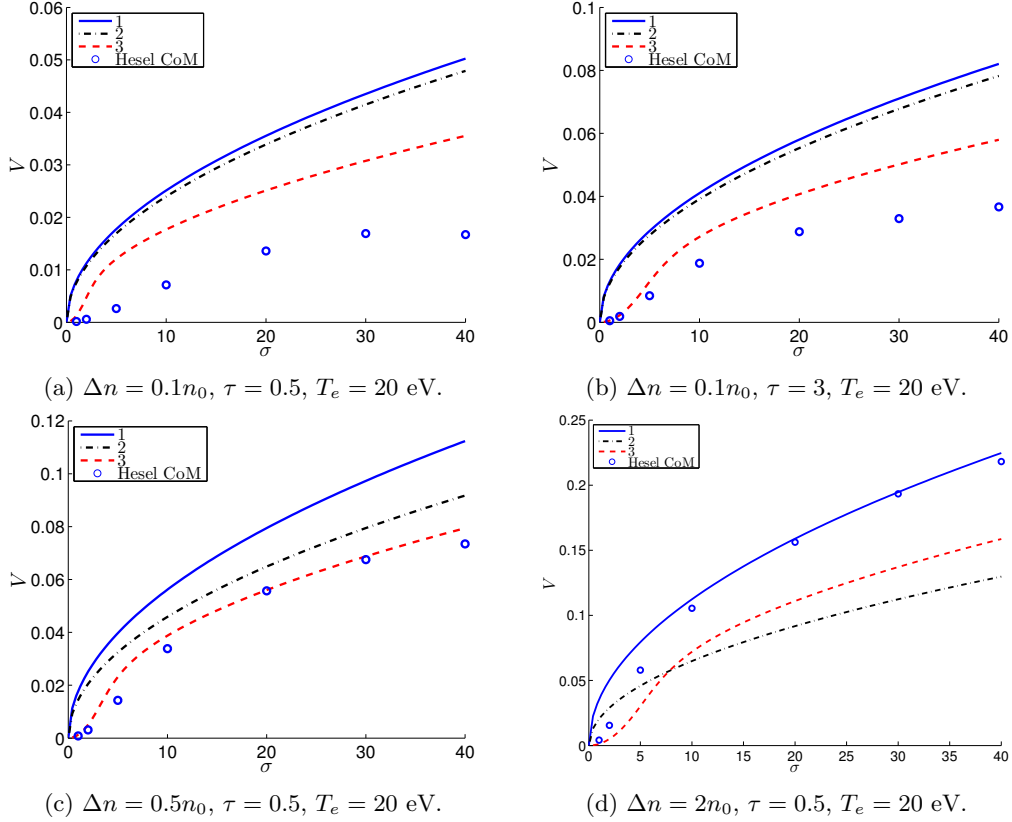


Figure 4.14: The maximum velocity of different blobs as a function of blob size with different initial values of τ and Δn . The blue dots are the numerically calculated maximum velocities, the full blue line denoted as 1 in the legend is given by Eq. (4.20), the dashed black line denoted as 2 in the legend is given by Eq. (4.21) and the dashed red line denoted as 3 in the legend is given by Eq. (4.22).

For small blobs the scaling proposed by Manz actually predicts a drop in the velocity as the ion temperature is increased, as seen in Figure 4.15c, which shows the maximum velocity as a function of τ for blobs with $\Delta = 0.5n_0$ and $\sigma = 5$. This is opposite of the behaviour seen in the simulations where the maximum velocity increases with τ , irrespective of the initial blob size. Both the local and global scalings overestimate the velocity for a blob with these parameters, and again the deviation between the scaling laws and the simulation values increases with τ . For a larger blob, $\sigma = 20$, otherwise with the same parameters, seen in Figure 4.15d, the effect of the temperature dependence in Eq. (4.22) is not as evident, however it still does not capture the scaling of the blob velocity with τ . Again the local and global models seem to capture the behaviour better despite the fact that the velocity again is estimated too high.

None of the scaling laws thus seem to fit with the blob velocity as a function of τ , however the local and global scaling laws explain the behaviour much better than the scaling proposed by Manz, which, for small blobs, predicts the opposite behaviour of what is observed in the simulations.

Dependence on blob amplitude

Finally, since the initial blob amplitude seems to have a large effect on the maximum velocity, the effect of different blob amplitudes is investigated by keeping the initial blob size and τ fixed. Due to the local approximation imposed by HESEL, the global model

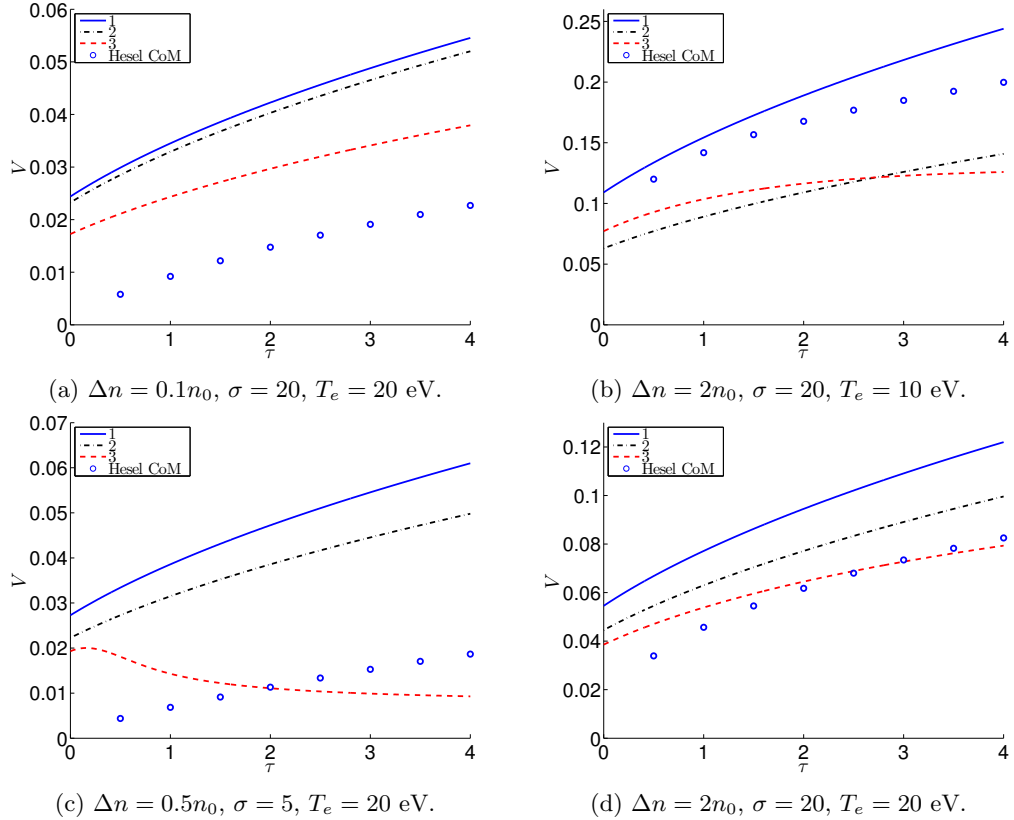


Figure 4.15: The maximum velocity of blobs as a function of τ with different initial values of σ and Δn . The blue dots are the numerically calculated maximum velocities, the full blue line denoted as 1 in the legend is given by Eq. (4.20), the dashed black line denoted as 2 in the legend is given by Eq. (4.21) and the dashed red line denoted as 3 in the legend is given by Eq. (4.22).

is not expected to fit with the numerical results, however as seen in Figure 4.16a, which shows the maximum velocity as a function of Δn of blobs with $\sigma = 20$ and $\tau = 0.5$, none of the scalings fit well with the simulation results, even at low temperatures, where FLR effects do not play a significant role. The numerical results seem to scale linearly with the blob amplitude, whereas the scaling models predict a scaling as $\sqrt{\Delta n}$. The same linear scaling is found when increasing τ to 3 as seen in Figure 4.16b, where both the local and the global models, and especially the scaling proposed by Manz show a behaviour far from the one observed in simulations. When increasing the blob size to $\sigma = 20$, the scaling also seems to be linear but with an increased slope as seen in Figure 4.16c, which is a plot of the maximum velocity as a function of Δn of blobs with $\sigma = 20$ and $\tau = 0.5$, and again none of the scaling laws fit well with the observed behaviour. For higher ion temperatures $\tau = 3$ and otherwise the same parameters, this behaviour is again observed, as illustrated in Figure 4.16d. This mismatch between the scaling laws and the numerically observed data is also observed in [17], so it appears that the amplitude dependence of the maximum velocity is not captured well by the theoretical estimate.

All in all, none of the velocity scalings capture the behaviour with varying initial conditions of the blob, which is likely due to several factors. First, the local and global scaling laws do not take FLR effects into account, and second, all scaling laws are found by an order of magnitude estimate of the vorticity equation, which does not capture the full dynamics of the blob propagation. However the seemingly linear scaling of the blob velocity is very

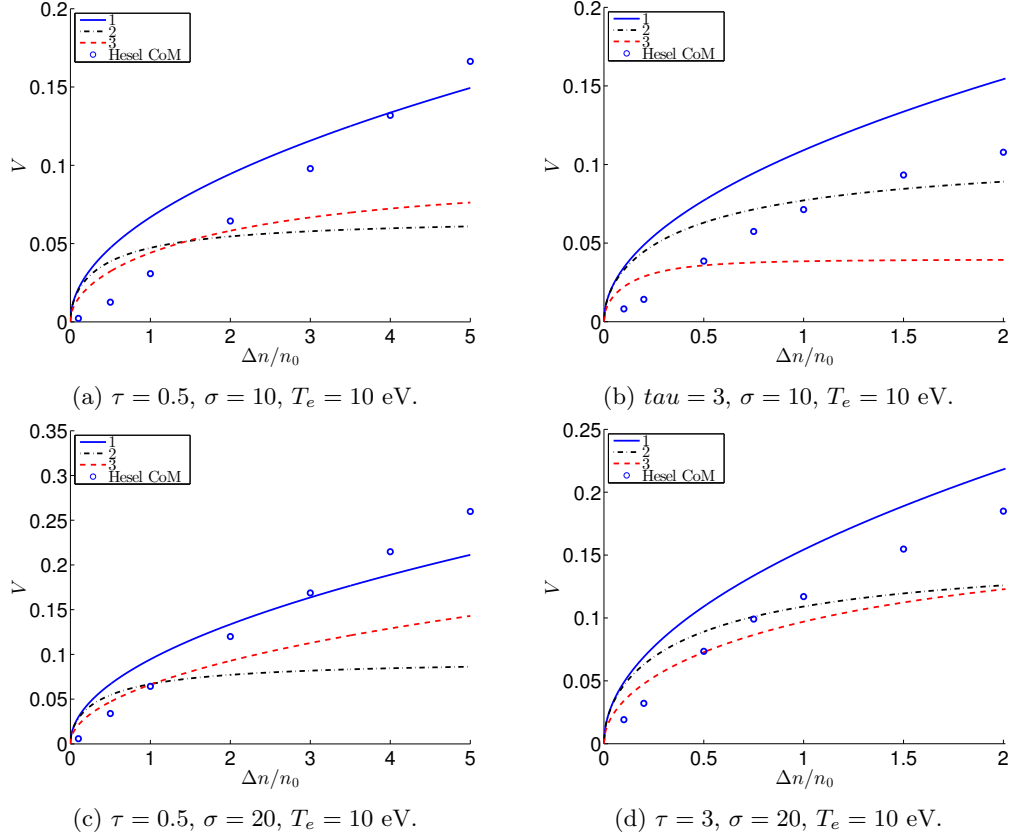


Figure 4.16: The maximum velocity of blobs as a function of Δn with different initial values of σ and τ . The blue dots are the numerically calculated maximum velocities, the full blue line denoted as 1 in the legend is given by Eq. (4.20), the dashed black line denoted as 2 in the legend is given by Eq. (4.21) and the dashed red line denoted as 3 in the legend is given by Eq. (4.22).

different from the expected behaviour and will need to be investigated further in future works.

Chapter 5

Conclusion

Radial transport in magnetically confined fusion plasmas is primarily caused by propagating coherent plasma filaments, also known as blobs. This project set out to investigate the behaviour of such filaments using an existing numerical code, HESEL.

To investigate the dynamics of these blobs, a series of intermediate goals addressing the key challenges were made. The first aim was to investigate simple analytical expressions for a magnetically confined plasma in order to describe the driving mechanisms behind different instabilities. The next was to understand how to use HESEL and how to describe blob structures from the output of the code, and finally the main goal was to use the code to investigate the dynamics of these blobs and compare them with both experimental results and other existing codes.

In this thesis, the equations governing plasma behaviour for small fluctuations in a magnetically confined fusion device were derived for both weakly and fully ionized plasmas using a series of assumptions. These equations were then used to examine the so-called interchange instability, resulting from magnetic field curvature, and the effect of drift-waves caused by parallel collisions. It was found that a phase-difference between density and potential fluctuations is essential for radial transport, and that the interchange instability and drift-waves have a maximum growth-rate at different phase differences. Finally it was seen that drift-waves have a stabilising effect on the interchange instability.

Next the HESEL code was applied in order to investigate the propagation and dynamics of blob structures, particularly those of seeded blobs, i.e. blobs initiated as a density perturbation on a uniform background. The main purpose of this was to investigate the scaling of the radial propagation velocity of these blobs with varying initial conditions - blob width and amplitude - for finite ion temperatures. To do this, three different ways of defining the position of the blob were investigated. One where the position is the centre of mass, one where it is the maximum value of the blob, and one at the position where 50% of the mass is located. It was found that the 50% and the centre of mass definitions were quite similar in the radial position, but the 50% was less sensitive to the blob leaving behind much of its initial mass for the poloidal position. However both the centre of mass and 50% were sensitive to the blob being positioned close to the edge when determining the poloidal position due to the periodic boundary conditions used in HESEL, and therefore care needed to be taken when determining the poloidal position. The maximum value was mostly quite close to the blob front, which is where most of the propagating mass is located and did not have the same problems regarding the poloidal positioning. However both the maximum value and the 50% scheme were tied to a grid point which caused difficulties when determining the maximum velocity, whereas the centre of mass scheme can be placed between grid-points and therefore does not have this issue. Furthermore, the centre of mass

is widely used in papers (see for example [17]) and is also a measure of the $\mathbf{E} \times \mathbf{B}$ particle flux, and this coordinate was therefore chosen to define the blob position.

The code was then used to simulate two different plasma regimes. First a weakly ionized plasma was examined using parameters from the TORPEX device, which is a small experimental device in the shape of a torus. The experimental density profiles with two different cases of initial blob condition were given, and for the first case, HESEL seemed to match the radial position of the experiment well. However there were significant discrepancies between the code and the experiment regarding both poloidal propagation and dissipation. The code estimated a much weaker dissipation than what was seen in the experiment for both cases, and the magnitude of the poloidal propagation was slightly smaller in the simulation. For the second case, the radial displacement was estimated too high compared to the experiment, likely due to the large amplitude of the blob compared to the background and the local approximation imposed in HESEL. Since the parameters of TORPEX are well out of the regime which HESEL normally operates in, this could explain some of the discrepancies observed. The simulation results were also compared with other codes, and also here differences were found between both the radial and poloidal positions of the blobs. These differences may be accounted for by the lack of parallel dynamics in HESEL, which were present in both GBS and BOUT++, with which HESEL was compared to.

Then a fully ionized plasma was investigated using parameters corresponding to the ASDEX device. It was found that small blobs dissipate faster than large blobs, and that also higher ion temperatures increases the dissipation. It was also found that a finite ion temperature has a large effect on the propagation of the blob. At low ion temperatures, the blobs generate the typical mushroom shape, seen in for example [17]. However at large ion temperatures, the blob was seen to retain much of its initial shape and the center of mass was seen to propagate both radially and poloidally whereas low ion temperature blobs only propagated radially. The increase in ion temperature also caused a less steep blob front to form, which caused the blobs to propagate further and retain a higher velocity than for cold ion blobs. A high initial blob amplitude was found to increase the effect of finite ion temperatures causing the blob to propagate both radially and poloidally at higher velocities, as the blob slowed down, the poloidal propagation was found to reverse directions.

Finally the maximum velocities of the centre of mass of the blobs were compared with three different scaling laws. It was found that the scaling proposed by Manz[12] explained the scaling with blob size and maximum radial velocity best, however it did also predict that the velocity $V \rightarrow 0$ as both the ion temperature normalized to the electron temperature τ and the initial blob amplitude Δn strongly increase, which is opposite of the behaviour seen in HESEL. The other scaling laws which the simulations were compared with were a local and a global scaling model, described in [6] and [24], respectively. Neither of these compared very well with HESEL when determining the maximum velocity with varying initial blob parameters. The velocity scaling as a function of temperature was not described with either the local or the global model. Both models deviated further from the values observed in HESEL as τ increased, likely due to ion finite larmor radius effects, present to first order in HESEL, but not used in the derivation of the scaling laws. None of the scaling laws described the increase in maximum velocity as a function of blob amplitude. The maximum velocities in HESEL appeared to scale linearly with increasing Δn , but both the local and global models describe the dependence as $\sqrt{\Delta n}$. It was thus concluded that none of the scaling laws described the maximum radial velocity with different initial parameters in HESEL with any of the parameters.

5.1 Outlook

This project set out to investigate blob behaviour with different initial parameters, and this was successfully accomplished. However, significant discrepancies between the simulations and experimental results for weakly ionized plasmas were found, and these still need to be accounted for.

For the fully ionized plasma, differences were found between the theoretical estimates of maximum blob velocity and the simulations. Especially for the scalings of maximum velocity with initial blob amplitude. Here the theory predicts a scaling as $\sqrt{\Delta n}$, where a linear scaling was observed. This is also left to be investigated in future works, both with further simulations and derivations of an analytical scaling law following the HESEL equations.

Finally parallel dynamics are neglected in HESEL, and a local approximation is made, and it would be interesting to implement these changes and determine whether these effects lead to a better description of the blob behaviour for weakly ionized plasmas.

Appendix A

Appendix A

A.1 Derivations

A.1.1 Derivation of the parallel velocity for a weakly ionized plasma

Assuming that $(\partial_t + u_{\sigma\parallel} \cdot \nabla_{\parallel}) \ll \omega_{ci}$, and that parallel collisions are on the order of ϵ^0 , the parallel velocity is found from Eq. (2.15);

$$\begin{aligned} n_{\sigma} q_{\sigma} \mathbf{E}_{\parallel} - \nabla_{\parallel} p_{\sigma} - \nu_{\sigma n} m_{\sigma} n_{\sigma} \mathbf{u}_{\sigma\parallel} &= 0 \\ \Rightarrow \nu_{\sigma n} m_{\sigma} n_{\sigma} \mathbf{u}_{\sigma\parallel} &= n_{\sigma} q_{\sigma} \mathbf{E}_{\parallel} - \nabla_{\parallel} p_{\sigma} \\ \Rightarrow \mathbf{u}_{\sigma\parallel} &= \frac{1}{\nu_{\sigma n} m_{\sigma} n_{\sigma}} (n_{\sigma} q_{\sigma} \mathbf{E}_{\parallel} - \nabla_{\parallel} p_{\sigma}) \\ \Rightarrow \mathbf{u}_{\sigma\parallel} &= \frac{1}{\nu_{\sigma n} m_{\sigma}} \left(-q_{\sigma} \nabla_{\parallel} \phi - T_{\sigma} \frac{\nabla_{\parallel} n_{\sigma}}{n_{\sigma}} \right) \\ \Rightarrow \mathbf{u}_{\sigma\parallel} &= \frac{T_{\sigma}}{m_{\sigma} \nu_{\sigma n}} \nabla_{\parallel} \left(\frac{-q_{\sigma} \phi}{T_{\sigma}} - \ln n_{\sigma} \right). \end{aligned} \quad (\text{A.1})$$

A.1.2 Derivation of the lowest order perpendicular velocity for a weakly ionized plasma

To lowest order Eq. (2.16) reads

$$n_{\sigma} q_{\sigma} (\mathbf{E}_{\perp} + \mathbf{u}_{\sigma\perp 0} \times \mathbf{B}) - T_{\sigma} \nabla_{\perp} n_{\sigma} = 0 \quad (\text{A.2})$$

Taking the cross-product of this equation with \mathbf{B} from the left leads to

$$n_{\sigma} q_{\sigma} (\mathbf{E}_{\perp} \times \mathbf{B} + (\mathbf{u}_{\sigma\perp 0} \times \mathbf{B}) \times \mathbf{B}) - T_{\sigma} \nabla_{\perp} n_{\sigma} \times \mathbf{B} = 0 \quad (\text{A.3})$$

Next using the vector identity $(\mathbf{A} \times \mathbf{B}) \times \mathbf{C} = (\mathbf{A} \cdot \mathbf{C}) \mathbf{B} - (\mathbf{B} \cdot \mathbf{C}) \mathbf{A}$, gives

$$n_{\sigma} q_{\sigma} (\mathbf{E}_{\perp} \times \mathbf{B} + (\mathbf{u}_{\sigma\perp 0} \cdot \mathbf{B}) \mathbf{B} - (\mathbf{B} \cdot \mathbf{B}) \mathbf{u}_{\sigma\perp 0}) - T_{\sigma} \nabla_{\perp} n_{\sigma} \times \mathbf{B} = 0. \quad (\text{A.4})$$

Now using that the dot-product between two perpendicular vectors is 0 and that $\mathbf{B} \cdot \mathbf{B} = B^2$ and solving for $\mathbf{u}_{\sigma\perp 0}$, leads to

$$\begin{aligned} \mathbf{u}_{\sigma\perp 0} &= \frac{\mathbf{E}_{\perp} \times \mathbf{B}}{B^2} - \frac{T_{\sigma} \nabla_{\perp} n_{\sigma} \times \mathbf{B}}{n_{\sigma} q_{\sigma} B^2} \\ &= -\frac{\nabla_{\perp} \phi \times \mathbf{B}}{B^2} - \frac{T_{\sigma}}{q_{\sigma} B^2} \nabla_{\perp} \ln n_{\sigma} \times \mathbf{B}. \end{aligned} \quad (\text{A.5})$$

A.1.3 Derivation of first order perpendicular velocity for a weakly ionized plasma

To order ϵ Eq. (2.16) gives[8],

$$n_\sigma m_\sigma \left(\frac{\partial}{\partial t} - \frac{\nabla_\perp \phi \times \mathbf{B}}{B^2} \cdot \nabla_\perp \right) \mathbf{u}_{\sigma\perp 0} = n_\sigma q_\sigma \mathbf{u}_{\sigma\perp 1} \times \mathbf{B} - \nu_{\sigma n} m_\sigma n_\sigma \mathbf{u}_{\sigma\perp 0}, \quad (\text{A.6})$$

where $-\nabla_\perp \phi \times \mathbf{B}/B^2$ is used as $\mathbf{u}_{\sigma\perp}$, since $T_\sigma \nabla_\perp \ln n_\sigma \times \mathbf{B}/q_\sigma B^2 \ll \nabla_\perp \phi \times \mathbf{B}/B^2$. Inserting $\mathbf{u}_{\sigma\perp 0}$ and denoting $d_t = \partial_t + \mathbf{u}_E \cdot \nabla_\perp$ gives

$$\left(n_\sigma m_\sigma \frac{d}{dt} + \nu_{\sigma n} m_\sigma n_\sigma \right) \left(-\frac{\nabla_\perp \phi \times \mathbf{B}}{B^2} - \frac{T_\sigma}{q_\sigma B^2} \nabla_\perp \ln n_\sigma \times \mathbf{B} \right) = n_\sigma q_\sigma \mathbf{u}_{\sigma\perp 1} \times \mathbf{B}. \quad (\text{A.7})$$

Moving $\times \mathbf{B}$ out of the parenthesis and dividing by $n_\sigma q_\sigma$ an equation for $\mathbf{u}_{\sigma\perp 1}$ is obtained

$$\begin{aligned} \mathbf{u}_{\sigma\perp 1} &= \frac{m_\sigma}{q_\sigma B^2} \frac{d}{dt} \nabla_\perp \left(-\phi - \frac{T_\sigma \ln n_\sigma}{q_\sigma} \right) - \frac{\nu_{\sigma n} m_\sigma}{q_\sigma B^2} \nabla_\perp \left(\phi + \frac{T_\sigma}{q_\sigma} \ln n_\sigma \right) \\ &= \frac{m_\sigma T_\sigma}{q_\sigma^2 B^2} \frac{d}{dt} \nabla_\perp \left(\frac{-q_\sigma \phi}{T_\sigma} - \ln n_\sigma \right) + \frac{\nu_{\sigma n} m_\sigma T_\sigma}{q_\sigma^2 B^2} \nabla_\perp \left(\frac{-q_\sigma \phi}{T_\sigma} - \ln n_\sigma \right). \end{aligned} \quad (\text{A.8})$$

A.1.4 Derivations of gradients for a weakly ionized plasma

The gradients of the $\mathbf{E} \times \mathbf{B}$ and diamagnetic drifts are given by

$$\nabla \cdot \mathbf{u}_E = -\nabla \cdot \frac{\nabla_\perp \phi \times \mathbf{b}}{B} = -\frac{\mathbf{b}}{B} \cdot (\nabla \times \nabla_\perp \phi) + \nabla_\perp \phi \cdot \left(\nabla \times \frac{\mathbf{b}}{B} \right) = \nabla_\perp \phi \cdot \left(\nabla \times \frac{\mathbf{b}}{B} \right), \quad (\text{A.9})$$

and

$$\begin{aligned} \nabla \cdot \mathbf{u}_{de} &= \nabla \cdot \frac{T_e}{e B^2} \nabla_\perp \ln n_e \times \mathbf{B} = \frac{T_e \mathbf{b}}{B} \cdot \left(\nabla \times \frac{\nabla_\perp \ln n_e}{e} \right) - \frac{T_e \nabla_\perp \ln n_e}{e} \cdot \left(\nabla \times \frac{\mathbf{b}}{B} \right) \\ &= -\frac{T_e \nabla_\perp \ln n_e}{q_e} \cdot \left(\nabla \times \frac{\mathbf{b}}{B} \right), \end{aligned} \quad (\text{A.10})$$

where it is used that the curl of a gradient is 0. Assuming that \mathbf{B} is a vacuum field gives $\nabla \times \mathbf{B} = 0$, so

$$\nabla \times \mathbf{B} = \nabla \times B \mathbf{b} = B \nabla \times \mathbf{b} + \nabla B \times \mathbf{b} = B \nabla \times \mathbf{b} - \mathbf{b} \times \nabla B = 0, \quad (\text{A.11})$$

which means that

$$\nabla \times \mathbf{b} = \frac{1}{B} \mathbf{b} \times \nabla B, \quad (\text{A.12})$$

which leads to

$$\begin{aligned} \nabla \times \frac{\mathbf{b}}{B} &= \frac{1}{B} \nabla \times \mathbf{b} + \nabla \frac{1}{B} \times \mathbf{b} = \frac{1}{B^2} \mathbf{b} \times \nabla B - \frac{1}{B^2} \nabla B \times \mathbf{b} = \frac{2}{B^2} \mathbf{b} \times \nabla B \\ &= \frac{2}{B} \mathbf{b} \times \nabla \ln B = -\frac{2}{BR} \hat{\mathbf{z}}, \end{aligned} \quad (\text{A.13})$$

where $\hat{\mathbf{z}}$ is in the direction of the major torus radius. This means that

$$\nabla \cdot \mathbf{u}_E = -\frac{2}{BR} \hat{\mathbf{z}} \cdot \nabla_\perp \phi \quad (\text{A.14})$$

and

$$\nabla \cdot \mathbf{u}_{de} = \frac{2T_e}{eBR} \hat{\mathbf{z}} \cdot \nabla_\perp \ln n_e, \quad (\text{A.15})$$

A.1.5 Derivation of first order perpendicular velocity for a fully ionized plasma

To order ϵ Eq. (2.44) reads

$$\begin{aligned}
n_\sigma m_\sigma \frac{d}{dt} \mathbf{u}_{\sigma \perp 0} &= n_\sigma q_\sigma \mathbf{u}_{\sigma \perp 1} \times \mathbf{B} - \nabla_{\perp} \boldsymbol{\Pi}_\sigma - \nu_{\sigma\alpha} m_\sigma n_\sigma (\mathbf{u}_{\sigma \perp 0} - \mathbf{u}_{\alpha \perp 0}) \\
\Rightarrow \mathbf{u}_{\sigma \perp 1} \times \mathbf{B} &= \frac{m_\sigma}{q_\sigma} \frac{d}{dt} \mathbf{u}_{\sigma \perp 0} + \frac{\nabla_{\perp} \boldsymbol{\Pi}_\sigma}{n_\sigma q_\sigma} + \frac{\nu_{\sigma\alpha} m_\sigma}{q_\sigma} (\mathbf{u}_{\sigma \perp 0} - \mathbf{u}_{\alpha \perp 0}) \\
\Rightarrow (\mathbf{u}_{\sigma \perp 1} \times \mathbf{B}) \times \mathbf{B} &= \frac{m_\sigma}{q_\sigma} \frac{d}{dt} \mathbf{u}_{\sigma \perp 0} \times \mathbf{B} + \frac{\nabla_{\perp} \boldsymbol{\Pi}_\sigma \times \mathbf{B}}{n_\sigma q_\sigma} + \frac{\nu_{\sigma\alpha} m_\sigma}{q_\sigma} (\mathbf{u}_{\sigma \perp 0} - \mathbf{u}_{\alpha \perp 0}) \times \mathbf{B} \\
\Rightarrow -B^2 \mathbf{u}_{\sigma \perp 1} &= \frac{m_\sigma}{q_\sigma} \frac{d}{dt} \mathbf{u}_{\sigma \perp 0} \times \mathbf{B} + \frac{\nabla_{\perp} \boldsymbol{\Pi}_\sigma \times \mathbf{B}}{n_\sigma q_\sigma} + \frac{\nu_{\sigma\alpha} m_\sigma}{q_\sigma} (\mathbf{u}_{\sigma \perp 0} - \mathbf{u}_{\alpha \perp 0}) \times \mathbf{B} \\
\Rightarrow \mathbf{u}_{\sigma \perp 1} &= \frac{m_\sigma}{B q_\sigma} \mathbf{b} \times \frac{d}{dt} \mathbf{u}_{\sigma \perp 0} + \frac{\mathbf{b} \times \nabla_{\perp} \boldsymbol{\Pi}_\sigma}{B n_\sigma q_\sigma} + \frac{\nu_{\sigma\alpha} m_\sigma}{B q_\sigma} \mathbf{b} \times (\mathbf{u}_{\sigma \perp 0} - \mathbf{u}_{\alpha \perp 0}). \tag{A.16}
\end{aligned}$$

A.1.6 Derivation of the stress-tensor for a fully ionized plasma

. For a hydrogen plasma, the stress-tensor is given by[10]

$$\begin{aligned}
\Pi_{xx} &= -\frac{\eta_0}{2} (W_{xx} + W_{yy}) - \frac{\eta_1}{2} (W_{xx} - W_{yy}) - \eta_3 W_{xy} \\
\Pi_{yy} &= -\frac{\eta_0}{2} (W_{xx} + W_{yy}) + \frac{\eta_1}{2} (W_{xx} - W_{yy}) + \eta_3 W_{xy} \\
\Pi_{xy} = \Pi_{yx} &= -\eta_1 W_{xy} + \frac{\eta_3}{2} (W_{xx} - W_{yy}) \\
\Pi_{xz} = \Pi_{zx} &= -\eta_2 W_{xz} - \eta_4 W_{yz} \\
\Pi_{yz} = \Pi_{zy} &= -\eta_2 W_{yz} + \eta_4 W_{xz} \\
\Pi_{zz} &= -\eta_0 W_{zz},
\end{aligned}$$

where $W_{jk} = \partial_k u_j + \partial_j u_k - \frac{2}{3} \delta_{jk} \nabla \cdot \mathbf{u}$ is the rate of the strain-tensor, and the viscosities are given by

$$\begin{aligned}
\eta_0^i &= 0.96n \frac{T_i}{\nu_i}, & \eta_1^i &= 0.3n \frac{T_i \nu_i}{\omega_{ci}^2}, & \eta_2^i &= 1.2n \frac{T_i \nu_i}{\omega_{ci}^2}, \\
\eta_3^i &= 0.5n \frac{T_i}{\omega_{ci}}, & \eta_4^i &= n \frac{T_i}{\omega_{ci}}, \\
\eta_0^e &= 0.73n \frac{T_e}{\nu_e}, & \eta_1^e &= 0.51n \frac{T_e \nu_e}{\omega_{ce}^2}, & \eta_2^e &= 2n \frac{T_e \nu_e}{\omega_{ce}^2}, \\
\eta_3^e &= -0.5n \frac{T_e}{\omega_{ce}}, & \eta_4^e &= -n \frac{T_e}{\omega_{ce}},
\end{aligned}$$

As seen from the above, η_3 and η_4 are independent of collisions, which is because they originate from lowest order gyroradius motion of the particles, whereas the gyroviscosities η_1 and η_2 depend on both ν and ω . In general η_0 is bigger than η_1 , η_2 , η_3 and η_4 , but the latter can still be important for incompressible motion or if diamagnetic drifts are present[10].

In order to evaluate $\mathbf{u}_{\Pi\sigma}$, we start by looking at $\boldsymbol{\Pi}_\sigma$. Since we are only looking at the perpendicular directions, only Π_{xx} , $\Pi_{xy} = \Pi_{yx}$ and Π_{yy} are relevant. Neglecting all effect

originating from gyroradius motion, we are left with

$$\begin{aligned}\Pi_{xx} &= -\frac{\eta_0}{2}(W_{xx} + W_{yy}) - \frac{\eta_1}{2}(W_{xx} - W_{yy}) \\ &= -\eta_0 \left(\partial_x u_x + \partial_y u_y - \frac{2}{3} \nabla \cdot \mathbf{u} \right) - \eta_1 (\partial_x u_x - \partial_y u_y) \\ &= -\eta_0 \left(\frac{1}{3} \partial_x u_x + \frac{1}{3} \partial_y u_y \right) - \eta_1 (\partial_x u_x - \partial_y u_y),\end{aligned}\quad (\text{A.17})$$

$$\begin{aligned}\Pi_{yy} &= -\frac{\eta_0}{2}(W_{xx} + W_{yy}) + \frac{\eta_1}{2}(W_{xx} - W_{yy}) \\ &= -\eta_0 \left(\partial_x u_x + \partial_y u_y - \frac{2}{3} \nabla \cdot \mathbf{u} \right) + \eta_1 (\partial_x u_x - \partial_y u_y) \\ &= -\eta_0 \left(\frac{1}{3} \partial_x u_x + \frac{1}{3} \partial_y u_y \right) + \eta_1 (\partial_x u_x - \partial_y u_y),\end{aligned}\quad (\text{A.18})$$

$$\Pi_{xy} = \Pi_{yx} = -\eta_1 (\partial_x u_y + \partial_y u_x). \quad (\text{A.19})$$

Since the largest contribution to the fluid velocity is \mathbf{u}_E , we will only include this term for the velocity. Assuming that the magnetic field is only along $\hat{\mathbf{z}}$, we have that

$$\mathbf{u}_E = -\frac{\nabla_\perp \phi \times \mathbf{b}}{B} = -\frac{1}{B} (\partial_y \phi \hat{\mathbf{x}} - \partial_x \phi \hat{\mathbf{y}}), \quad (\text{A.20})$$

which means that $u_x = -\partial_y \phi / B$ and $u_y = \partial_x \phi / B$, so

$$\begin{aligned}\Pi_{xx} &= -\frac{\eta_0}{3B} (-\partial_{xy} \phi + \partial_{yx} \phi) - \frac{\eta_1}{B} (-\partial_{xy} \phi - \partial_{yx} \phi), \\ &= \frac{2\eta_1}{B} \partial_{xy} \phi\end{aligned}\quad (\text{A.21})$$

$$\Pi_{yy} = -\frac{2\eta_1}{B} \partial_{xy} \phi \quad (\text{A.22})$$

$$\Pi_{xy} = \Pi_{yx} = -\frac{\eta_1}{B} (\partial_{xx} \phi - \partial_{yy} \phi). \quad (\text{A.23})$$

Inserting this in the expression for $\mathbf{u}_{\Pi\sigma}$, we get

$$\begin{aligned}\mathbf{u}_{\Pi\sigma} &= \frac{\mathbf{b} \times \nabla_\perp \Pi_\sigma}{B n_\sigma q_\sigma} = \frac{\mathbf{b}}{B n_\sigma q_\sigma} \times \left(\nabla_\perp \cdot \begin{bmatrix} \frac{2\eta_1^\sigma}{B} \partial_{xy} \phi & -\frac{\eta_1^\sigma}{B} (\partial_{xx} - \partial_{yy}) \phi \\ -\frac{\eta_1^\sigma}{B} (\partial_{xx} - \partial_{yy}) \phi & -\frac{2\eta_1^\sigma}{B} \partial_{xy} \phi \end{bmatrix} \right) \\ &= \frac{\mathbf{b}}{B n_\sigma q_\sigma} \times \begin{bmatrix} \partial_x \frac{2\eta_1^\sigma}{B} \partial_{xy} \phi - \partial_y \frac{\eta_1^\sigma}{B} (\partial_{xx} - \partial_{yy}) \phi \\ -\partial_x \frac{\eta_1^\sigma}{B} (\partial_{xx} - \partial_{yy}) \phi - \partial_y \frac{2\eta_1^\sigma}{B} \partial_{xy} \phi \end{bmatrix}\end{aligned}\quad (\text{A.24})$$

Assuming η_1^σ is independent of x and y , we get

$$\mathbf{u}_{\Pi\sigma} = \frac{\eta_1^\sigma \mathbf{b}}{B^2 n_\sigma q_\sigma} \times \begin{bmatrix} \partial_{xxy} + \partial_{yyy} \\ -\partial_{xxx} - \partial_{xyy} \end{bmatrix} \phi = \frac{\eta_1^\sigma}{B^2 n_\sigma q_\sigma} \begin{bmatrix} -\partial_{xxx} - \partial_{xyy} \\ -\partial_{yyy} - \partial_{xxy} \end{bmatrix} \phi = -\frac{\eta_1^\sigma}{B^2 n_\sigma q_\sigma} \nabla_\perp \cdot \nabla_\perp^2 \phi. \quad (\text{A.25})$$

A.1.7 Derivation of dispersion relation

With the definitions in Eq. (2.68) and Eq. (2.69), the term involving ω in Eq. (2.67) can be rewritten as

$$\begin{aligned}-\xi k_y + i\nu_e^{-1} k_\parallel^2 + i\nu_e^{-1} \frac{k_\parallel^2}{k_\perp^2} &= -\omega_{fm} + i\nu_e^{-1} k_\parallel^2 \left(1 + \frac{1}{k_\perp^2} \right) = -\omega_{fm} + i\nu_e^{-1} k_\parallel^2 \left(\frac{k_\perp^2 + 1}{k_\perp^2} \right) \\ &= -\omega_{fm} + i\Psi \frac{\kappa k_y k_\perp^2}{1 + k_\perp^2} \frac{1}{k_\perp^2} = -\omega_{fm} + i\Psi \omega_{dw},\end{aligned}$$

and the constant term as

$$\begin{aligned} & -i \frac{\nu_e^{-1} \kappa k_y k_{\parallel}^2}{k_{\perp}^2} + \frac{\kappa k_y \omega_{fm}}{k_{\perp}^2} - \frac{\omega_{fm}^2}{k_{\perp}^2} + \frac{\nu_e^{-1} k_{\parallel}^2 i \omega_{fm}}{k_{\perp}^2} \\ & = -i \Psi \frac{\kappa^2 k_y^2}{(1 + k_{\perp}^2)^2} + \frac{\kappa \xi k_y \omega_{fm} - \xi \omega_{fm}^2}{\xi k_{\perp}^2} + i \omega_{fm} \Psi \frac{\kappa k_y}{(1 + k_{\perp}^2)^2} \\ & = -i \Psi \omega_{dw}^2 + \frac{\omega_{fm}^2}{\Phi} + i \omega_{fm} \omega_{dw} \frac{\Psi}{1 + k_{\perp}^2}, \end{aligned}$$

which gives the dispersion relation

$$\omega^2 + (i \Psi \omega_{dw} - \omega_{fm}) \omega - i \Psi \omega_{dw}^2 + \frac{\omega_{fm}^2}{\Phi} + i \omega_{fm} \omega_{dw} \frac{\Psi}{1 + k_{\perp}^2} = 0. \quad (\text{A.26})$$

A.1.8 Derivation of the finite difference scheme

To derive a fourth-order central-difference scheme for $\partial u / \partial t$, u is first Taylor expanded around the point t , which yields

$$u(t \pm \delta t) = u(t) \pm u'(t) \delta t + \frac{u''(t) \delta t^2}{2!} \pm \frac{u'''(t) \delta t^3}{3!} + \frac{u''''(t) \delta t^4}{4!} + O(\delta t^5), \quad (\text{A.27})$$

where δt is the step-size, and prime denotes differentiation. However this equation is not enough if an error of fourth order is required, so in order to do this, more points are taken into account, namely $t \pm 2\delta t$, and Taylor expanded around t .

$$u(t \pm 2\delta t) = u(t) \pm 2u'(t) \delta t + \frac{u''(t) 4\delta t^2}{2!} \pm \frac{u'''(t) 8\delta t^3}{3!} + \frac{u''''(t) 16\delta t^4}{4!} + O(\delta t^5). \quad (\text{A.28})$$

This leads to

$$\begin{aligned} & u(t + \delta t) - u(t - \delta t) \\ & = \left(u(t) + u'(t) \delta t + \frac{u''(t) \delta t^2}{2!} + \frac{u'''(t) \delta t^3}{3!} + \frac{u''''(t) \delta t^4}{4!} + \frac{u'''''(t) \delta t^5}{5!} + O(\delta t^6) \right. \\ & \quad \left. - \left(u(t) - u'(t) \delta t + \frac{u''(t) \delta t^2}{2!} - \frac{u'''(t) \delta t^3}{3!} + \frac{u''''(t) \delta t^4}{4!} + \frac{u'''''(t) \delta t^5}{5!} + O(\delta t^6) \right) \right) \\ & = 2u'(t) \delta t + \frac{2u'''(t) \delta t^2}{3!} + \frac{2u'''''(t) \delta t^5}{5!}, \end{aligned} \quad (\text{A.29})$$

and

$$\begin{aligned} & u(t + 2\delta t) - u(t - 2\delta t) \\ & = \left(u(t) + 2u'(t) \delta t + \frac{4u''(t) \delta t^2}{2!} + \frac{8u'''(t) \delta t^3}{3!} + \frac{16u''''(t) \delta t^4}{4!} + \frac{32u'''''(t) \delta t^5}{5!} + O(\delta t^6) \right. \\ & \quad \left. - \left(u(t) - 2u'(t) \delta t + \frac{4u''(t) \delta t^2}{2!} - \frac{8u'''(t) \delta t^3}{3!} + \frac{16u''''(t) \delta t^4}{4!} + \frac{32u'''''(t) \delta t^5}{5!} + O(\delta t^6) \right) \right) \\ & = 4u'(t) \delta t + \frac{16u'''(t) \delta t^2}{3!} + \frac{64u'''''(t) \delta t^5}{5!}, \end{aligned} \quad (\text{A.30})$$

Now multiplying Eq. A.29 by 8 and subtracting Eq. A.30 from it gives

$$8u(t + \delta t) - 8u(t - \delta t) - u(t + 2\delta t) + u(t - 2\delta t) = 12u'(t) \delta t - \frac{48}{5!} u'''''(t) \delta t^5 \quad (\text{A.31})$$

which leads to a fourth-order central difference scheme for $\partial u / \partial t$ of

$$u'(t) = \frac{8u(t + \delta t) - 8u(t - \delta t) - u(t + 2\delta t) + u(t - 2\delta t)}{12\delta t} + O(\delta t^4). \quad (\text{A.32})$$

Appendix B

Appendix B

B.1 Matlab Scripts

B.1.1 VelocityCalc.m

```
clear all
clc

% Initialization
w = 212; % filenumber
file = sprintf('ASDEX.%d.h5',w); % input filename
esel = esel_read_head(file); % read parameters

% Initialize parameters
xmax = esel.Lx; % maximum radial position [rho_s]
ymax = esel.Ly; % maximum poloidal position [rho_s]
tmax = h5readatt(file,'/params/structure_param','end_time'); % End time [1/←
    omega_ci]
n0 = h5readatt(file,'/params/structure_param','mean_flow_p1'); % Background ←
    density [ $10^{19} \text{ m}^{-3}$ ]
Te = esel.Te0; % Electron temperature [eV]
Ti = esel.Ti0; % Ion temperature [eV]
cs = esel.Cs; % Ion sound speed [m/s]
omegaCi = esel.omegaci; % ion cyclotron frequency [ $\text{s}^{-1}$ ]
sigma = h5readatt(file,'/params/structure_param','mean_flow_p2'); % blob size [←
    rho_s]
rho_s = esel.rhos; % ion gyration radius [m]
dn = h5readatt(file,'/params/structure_param','mean_flow_p3'); % blob amplitude ←
    [ $10^{19} \text{ m}^{-3}$ ]
R = h5readatt(file,'/params/structure_param','R0'); % major radius [m]
R = R/rho_s; % major radius in [rho_s]

% Read density
dens = h5read(file,'/data/xanimation/density');
% Length of time and space coordinates
Lt = length(dens(1,1,:));
Lx = length(dens(:,1,1));
Ly = length(dens(1,:,:));

% Increment size
x = xmax/Lx;
y = ymax/Ly;
tinc = esel.time1D;

% Find maximum value of x and y and index of it
[maxValueX, IndicesX] = max(dens,[],2);
[maxValueY, IndicesY] = max(dens,[],1);

% Make 2D max of x as function of time and find indices
IndiceX = permute(maxValueX,[1,3,2]);
IndiceY = permute(maxValueY,[2,3,1]);
%Find indices of max for both x and y per time-step
[maxX, IndexX] = max(IndiceX);
[maxY, IndexY] = max(IndiceY);
```

```
% Calculate the center of mass point
densx=zeros(Lt,1);
densy=zeros(Lt,1);
M = sum(sum(dens-n0));
for k=1:Lt
    % Set initial density to 0 at each time-step
    densityx=0;
    densityy=0;
    % Calculate weighted value of blob minus background
    for i=1:Lx
        densityx = densityx + sum(dens(:, :, k)-n0)*double(i);
    end
    for j=1:Ly
        densityy = densityy + sum(dens(:, :, j)-n0)*double(j);
    end
    densx(k)=1/M(1,1,k)*densityx;
    densy(k)=1/M(1,1,k)*densityy;
end

% Calculate radial point for which 50% has passed
f = zeros(Lt,1);
perc = 0.5;
for i=1:Lt
    k=1;
    while h>M(1,1,i)*perc
        h = h+sum(dens(k, :, i)-n0);
        k=k+1;
    end
    f(i) = Lx-k;
end

% Convert to SI units
IndexX = IndexX*x*esel.rhos;
IndexY = IndexY*y*esel.rhos;
densx = densx*x*esel.rhos;
densy = densy*y*esel.rhos;
f = f*x*esel.rhos;

% Calculate velocity
veloIndexX = zeros(Lt,1);
veloDensX = zeros(Lt,1);
veloP = zeros(Lt,1);
veloIndexX(3:Lt-2)=(8*IndexX(4:Lt-1)-8*IndexX(2:Lt-3)+IndexX(1:Lt-4)-IndexX(5:Lt)←
    ))/(12*tinc);
veloDensX(3:Lt-2)=(8*densx(4:Lt-1)-8*densx(2:Lt-3)+densx(1:Lt-4)-densx(5:Lt))←
    /(12*tinc);
veloP(3:Lt-2)=(8*f(4:Lt-1)-8*f(2:Lt-3)+f(1:Lt-4)-f(5:Lt))/(12*tinc);

% Find maximum values of velocity
mVI = max(veloIndexX)/cs;
mVD = max(veloDensX)/cs;
mVP = max(veloP)/cs;
```

Bibliography

- [1] What is fusion? <https://www.iter.org/sci/whatisfusion>. Accessed: 2015-01-03.
- [2] George M. Hornberger. New manuscript guidelines for the reporting of stable hydrogen, carbon, and oxygen isotope ratio data. *Water Resources Research*, 31(12):2895–2895, 1995.
- [3] JET Team. Fusion energy production from a deuterium-tritium plasma in the JET tokamak. *Nuclear Fusion*, 32(2):187, 1992.
- [4] John Wesson. *Tokamaks*. Oxford University Press, 2011.
- [5] Tokamak (scheme) by abteilung Öffentlichkeitsarbeit - max-planck institut für plasmaphysik. [http://commons.wikimedia.org/wiki/File:Tokamak_\(scheme\).jpg#mediaviewer/File:Tokamak_\(scheme\).jpg](http://commons.wikimedia.org/wiki/File:Tokamak_(scheme).jpg#mediaviewer/File:Tokamak_(scheme).jpg). Accessed: 2015-01-06.
- [6] O. E. Garcia, N. H. Bian, and W. Fundamenski. Radial interchange motions of plasma filaments. *Physics of Plasmas (1994-present)*, 13(8):–, 2006.
- [7] Jens Juul Rasmussen, Volker Naulin, and Mirko Salewski. Pressure driven instabilities in magnetized plasmas: The interchange instability. University Lecture, 2013.
- [8] Paul M. Bellan. *Fundamentals of Plasma Physics*. Cambridge, 2006.
- [9] O. E. Garcia. Two-field transport models for magnetized plasmas. *J. Plasma Physics*, 65:81–96, 2001.
- [10] P. K. Shukla, M. Y. Yu, H. U. Rahman, and K. H. Spatschek. Nonlinear convective motion in plasmas. *Physics Reports*, 105:227–328, 1984.
- [11] J. Horacek, O. E. Garcia, J. P. Graves, R. A. Pitts, A. H. Nielsen, V. Naulin, and J. J. Rasmussen. Plasma electrostatic turbulence in TCV tokamak edge: direct comparison of experiment with 2D simulation. *ECA*, 29C, 2005.
- [12] P. Manz, D. Carralero, G. Birkenmeier, H. W. Müller, S. H. Müller, G. Fuchert, B. D. Scott, and U. Stroth. Filament velocity scaling laws for warm ions. *Physics of Plasmas (1994-present)*, 20(10):–, 2013.
- [13] Søren Bang Korsholm, Stefan Kragh Nielsen, Jens Juul Rasmussen, and Connie Munch Westergaard. *Association Euratom - DTU, Technical University of Denmark, Department of Physics - Annual Progress Report 2013*. Department of Physics, Technical University of Denmark, 2014.
- [14] Jens Madsen. Write-up. Unfinished note deriving HESEL, 2014.

- [15] S. I. Krasheninnikov and A. I. Smolyakov. Dynamics and generation mechanisms of mesoscale structures in tokamak edge plasmasa). *Physics of Plasmas (1994-present)*, 15(5):–, 2008.
- [16] A. H. Nielsen, G. S. Xu, J. Madsen, V. Naulin, J. J. Rasmussen, and B. N. Wan. Simulation of transition dynamics to high confinement in fusion plasmas. Unpublished article.
- [17] M. Wiesenberger, J. Madsen, and A. Kendl. Radial convection of finite ion temperature, high amplitude plasma blobs. *Physics of Plasmas (1994-present)*, 21, 2014.
- [18] F. Riva and I. Furno. Data necessary for the simulation of seeded blobs in the TORPEX device. Unpublished note on initialization parameters for TORPEX, 2014.
- [19] Lawrence Baylor Robinson. Theoretical elastic collision frequency between electrons and neutral atoms in a cesium plasma. *Phys. Rev.*, 127:2076–2080, Sep 1962.
- [20] Jens Madsen, Odd E. Garcia, Jeppe Stærk Larsen, Volker Naulin, Anders H. Nielsen, and Jens Juul Rasmussen. The influence of finite larmor radius effects on the radial interchange motions of plasma filaments. *Physics of Plasmas (1994-present)*, 18(11):–, 2011.
- [21] L. Easy, F. Militello, and J. Omotani. Status of TORPEX filament simulations using BOUT++. Powerpoint presentation, 2014. Presented: 2014-10-20.
- [22] F. Riva et al. Gbs simulation results. Powerpoint presentation, 2014. Presented: 2014-10-20.
- [23] A. Y. Aydemir. Convective transport in the scrape-off layer of tokamaks. *Physics of Plasmas (1994-present)*, 12(6):–, 2005.
- [24] R. Kube and O. E. Garcia. Velocity scaling for filament motion in scrape-off layer plasmas. *Physics of Plasmas (1994-present)*, 18(10):–, 2011.